Propriétés structurales, optiques et électroniques des couches d'InN et hétérostructures riches en indium pour applications optoélectroniques

Geeta Rani Mutta

To cite this version:

Geeta Rani Mutta. Propriétés structurales, optiques et électroniques des couches d'InN et hétérostructures riches en indium pour applications optoélectroniques. Electronique. Université de Caen, 2012. Français. <tel-01077170>

HAL Id: tel-01077170
https://hal.archives-ouvertes.fr/tel-01077170

Submitted on 24 Oct 2014

UNIVERSITÉ de CAEN BASSE-NORMANDIE

U.F.R.: Sciences

ECOLE DOCTORALE: Structure, Information, Matière et Matériaux

THESE

Présentée par

Geeta Rani MUTTA

et soutenue le 27 juin 2012

en vue de l'obtention du

DOCTORAT de L'UNIVERSITÉ de CAEN

Spécialité: Milieux denses, matériaux et composants

Propriétés structurales, optiques et électroniques des couches d'InN et hétérostructures riches en indium pour applications optoélectroniques

MEMBRES du JURY

M. Régis CARIN	Professeur, Université de Caen	Président du jury
M. Laurent PICHON	Professeur, Université de Rennes	Rapporteur
M. Philippe VERMAUT	Maître de conférences, ENSCP, Paris	Rapporteur
Mme Eva MONROY	Ingénieur CEA, INAC, Grenoble	Examinateur
M. Philippe de MIERRY	Chargé de Recherche, CRHEA, Valbonne	Examinateur
M. Jean-Louis DOUALAN	Chargé de Recherche, CIMAP, Caen	Examinateur
M. Jean-Marc ROUTOURE	Professeur, Université de Caen	Co-directeur de thèse
M. Pierre RUTERANA	Directeur de Recherche, CIMAP, Caen	Directeur de thèse

Dedicated to my father Late Mutta Narasinga Rao

There is not a more pleasing exercise of the mind than gratitude. It is accompanied with such an inward satisfaction that the duty is sufficiently rewarded by the performance

~Joseph Addison

Acknowledgements

The work presented in this dissertation has been carried out at CIMAP and GREYC laboratories during the period 2009-2012. My thesis entitled: **“Structural, optical and electronic properties of InN thinfilms and In rich heterostructures for optoelectronic applications”** has been performed in the frame work of the European Union project RAINBOW. Behind the accomplishment, there is a number of people, who helped to make it possible and I take this opportunity to express my special gratitude to them.

First of all I express my deep gratitude to my Ph. D advisors, Dr. Pierre Ruterana and Prof. Jean Marc Routoure, who have given me the opportunity to work with them when they choose me for the Marie Curie Fellowship. They introduced me to the field of Transmission Electron Microscopy and low frequency noise techniques, their ideas and guidance have been invaluable. I thank them for providing me with useful comments and directions in order to improve my research. They provided me numerous opportunities to give presentations, encouraged logical, problem solving and gave me confidence whenever I needed it. I am very grateful for the freedom I was given during the project and the constant encouragement when I felt it was all going wrong! I am always amazed at their reduction of complex problems to its simplest and specially to accomplish the deadlines in short time. I am also glad of the opportunities to learn about the administrative matters in addition to scientific work. I express my extended thanks to Dr. Ruterana for rewriting the French part of Ph. D thesis.

I wish to express my sincere thanks to the members of my Ph. D Jury: the President Prof. Regis Carin, the reviewers: Prof. Laurent Pichon and Dr. Philippe Vermaut; the examiners: Dr. Eva Monroy and Dr. Philippe de Mierry, firstly for accepting to judge my work and for their constructive comments which enhanced the manuscript to its present shape.

I owe a great deal of thanks to Dr. Laurence Mechin and Dr. Bruno Guillet, who were very supportive and always entertained my questions in every aspect of learning from conducting experiments to analysing the data and also to make critical comments which helped me to understand better the concepts of precision in measurements, knowledge in device fabrication and many more.

I express my gratitude to Prof. Jean Louis Doualan for teaching me to conduct optical measurements. I enjoyed his help, guidance, insight and humour all these years.

I am very much grateful to Dr. Magali Morales, Dr. Phillipe Marie, Prof. Christian Dufour and Dr. Fabrice Gourbilleau for rekindling my interests in crystallography, semiconductor physics, quantum mechanics, nanotechlonogy and proving that learning can be fun. I extend my sincere thanks to Dr. Serge Bouffard, head of the Laboratory, for having accepted me in CIMAP; he has always been a source of encouragement through the tough times with administrative matters.

I convey my special thanks to Marie-Pierre Chauvat, who was always available for teaching me the sample preparation for TEM and to fix my computer so often. I also thank Cédric Fur for showing me the device fabrication steps on InN layers. I thank Dr. Bertrand Lacroix for STEM measurements and also for his fruitful scientific discussions.

Huge thanks to the RAINBOW family members with whom I built good collaboration all along the past three years and for exchanging the scientific ideas, as well as spending good times in workshops and conferences. Additionally, I express here my sincere thanks to Prof. R. Goldhahn and Prof. F. Calle for letting me visit their groups and giving the time for insight during scientific discussions.

I was really lucky to have perfect Ph.D students, who provided assistance to me during my work, especially Arantxa, Céline ,Yi, An, Chang hui from CIMAP and Dalal ,Shuang, Sheng, Rachida and Hakim from GREYC. I specially thank Pratibha, with whom I shared special memories in Caen.

I extend my heartfelt thanks to Yadira for her cordial scientific and social discussions with me. I acknowledge Pierre Mathieu, Julien, Cédric, Michael, Stéphane and Nicolle for the good times spent at lunches and also for putting a large effort in hearing and correcting my French.

My special thanks to Elodie, Delphine, Nicolle Chasle and Claire, for their indispensable aide concerned with travel, administration and bureaucratic matters efficiently during my stay.

I shall be morally failing if I do not express my thanks to Larysa and Vladimir, who were always available for scientific discussions as well as to give me a constant co-operation and moral support during my stay here in Caen.

Many thanks to all of the past and present colleagues of CIMAP and GREYC, for making nice and jovial working atmosphere. To all of you, thanks for making my time in Caen, a great experience both in the lab and in the outside world.

My special thanks to Srinivas, Uma Mahesh and Jyothi, for having a lot of interesting and intellectual debates and also for being very supportive whenever I needed.

I pay respect to my family members, who have been great over the years. Without their whole hearted support, love and encouragement I would not have been here. Finally, I thank my angel niece: Swetha, for her unconditional love and affection towards me.

Geeta Rani Mutta

CONTENTS

Chapter 2 23
Experimental techniques

Chapter 3 49

Plasma Assisted Molecular Beam Epitaxial InN layers electrical conduction

Chapter 4 78

InGaN Quantum wells: Transmission Electron Microscopy and Photoluminescence studies

Résumé

Au cours des deux dernières décennies, les semi-conducteurs nitrures (AlN, GaN, InN) ont été sujets à des recherches très intenses en raison des nombreuses applications (diodes électroluminescentes (LED), transistors de puissance, composants hyperfréquences, *etc*, ..). L'effort de recherche s'est amplifié depuis 2002, quand la bande d'InN a été réévaluée à 0,65 eV au lieu de 1,89 eV, admis auparavant pendant plus de 20 ans. Cette découverte à ouvert la voie aux nitrures pour la possible fabrication des LED multicolores qui devraient couvrir les gammes de longueurs d'onde de l'UV lointain au proche infrarouge avec des applications très attendue dans l'éclairage faible consommation par exemple. De plus, le semi-conducteur InN présente une mobilité d'électron de plus de 4000 $cm^2V^{-1}s^{-1}$ ce qui pourrait aussi constituer une plateforme pour le développement de composants électroniques fonctionnant jusque dans la gamme terahertz. Actuellement, la qualité des couches d'InN n'est pas encore optimale et beaucoup d'efforts de recherche sont encore nécessaire pour améliorer et comprendre ses propriétés.

Mon travail doctoral s'inscrit dans cette dynamique et porte sur « les propriétés structurelles, optiques et électroniques de films d'InN et hétérostructures riches en indium ». Il a été effectué dans les laboratoires de CIMAP et GREYC dans le cadre du projet RAINBOW Initial Training Network du 7ème Programme Cadre de Developpement Européén de la section People". Le projet RAINBOW (2008-2012) avait comme objectif la réalisation « des couches d'InN de qualité optimale et l'investigation des propriétés intrinsèques d'InN et d'alliages de nitrures riches en indium ». Il consiste en une étude des dispositifs en corrélation avec les propriétés structurales. A cet effet, deux dispositifs ont été abordés: 1) des composants, mis en forme par des techniques de photolithographie, dans des couches d'InN fabriquées par épitaxie aux jets moléculaires assistée par plasma, 2) des puits quantiques InGaN/GaN qui constituent les zones actives des diodes électroluminescentes et des diodes lasers. Dans le premier cas, nous avons cherché à accéder à la conduction de volume d'InN car ses propriétés remarquables ne sont pas encore exploitées à cause d'une accumulation intrinsèque de charge aux surfaces. Pour se faire, nous avons utilisé des mesures du bruit basse fréquence.

Le deuxième volet de ce travail s'est inscrit dans l'analyse des mécanismes qui pourraient expliquer la forte efficacité d'émission bleue dans les puits quantiques InGaN/GaN

malgré les fortes densités de défauts (>10^8cm^{-2}). Pour se faire, nous avons analysé la structure, la chimie et la morphologie des puits quantiques en fonction des conditions de croissance. Ces données ont été corrélées avec les propriétés optiques.

Le manuscrit est divisé en cinq chapitres**.** Le premier chapitre est divisé en deux sections. La première section constitue une brève description des propriétés et applications des semi-conducteurs nitrures et leurs alliages. Leur structure cristalline la plus stable est la structure wurtzite qui n'est pas centro-symétrique. Par conséquent, les couches ont une polarité de cristal N ou métal et les surfaces correspondantes présentent des propriétés très différentes. Les techniques principales de croissance des nitrures sont l'épitaxie aux jets moléculaires (MBE) et l'épitaxie en phase vapeur aux organométalliques (MOVPE). Les substrats communément utilisés pour dépôt des nitrures sont le saphir, le carbure de silicium et le silicium. Comme la structure wurtzite est polaire, il existe un moment dipolaire qui engendre un champ de polarisation spontané le long des directions polaires. En plus, une polarisation piézoélectrique est produite par la tension aux interfaces dans toute l'hétéroépitaxie. Ces champs de polarisation affectent les performances des dispositifs. Ils peuvent être diminués par un choix judicieux de l'orientation de croissance des couches. Au cours de ce travail, nous avons seulement étudié des couches épitaxiées le long de la direction polaire [0001]. La deuxième section du 1er chapitre porte sur l'analyse des matériaux et dispositifs par mesures du bruit basse fréquence. Ces mesures constituent un outil de diagnostic pour explorer les propriétés mésoscopiques et/ou microscopiques des matériaux, car le niveau et le type de bruit est très sensible aux processus de transport. En effet, le bruit intrinsèque dans un système électrique résulte des fluctuations spontanées dans la conductivité électrique. Il est mesuré en terme~~s~~ de fluctuations sur la tension à travers les terminaux de l'appareil ou dans le courant qui y circule. Ces fluctuations peuvent être analysées dans le domaine spectrale à l'aide de la densité spectrale de bruit contenant généralement trois contributions : le bruit blanc, le bruit Lorentzien et le bruit en 1/f. Les mesures de bruit présentaient, pour nous, un intérêt considérable car I) le niveau de bruit est un indicateur sensible de la qualité du matériau et II) il fournit, par la comparaison avec les modèles théoriques, une façon de déterminer les mécanismes dominants de conduction.

Dans le deuxième chapitre, nous avons décrit premièrement les deux techniques de croissance les plus utilisées pour la réalisation des couches épitaxiales des nitrures et ensuite les techniques expérimentales utilisées pour caractériser les hétérostructures d'InN et InGaN/GaN. Nous avons utilisé une série de techniques de microscopie (AFM, SEM, TEM, HRTEM et STEM) pour déterminer la rugosité de surface, la morphologie, la microstructure ainsi que la composition dans puits quantiques InGaN/GaN. Le principe et le mode d'opération de chaque technique ont été exposés ainsi que les méthodologies pour la préparation d'échantillons de TEM. La caractérisation de la photoluminescence a été mise en œuvre pour analyser les propriétés optiques des couches d'InN et des puits quantiques InGaN/GaN. Les propriétés électriques de transport dans les couches d'InN ont été mesurées sur une gamme de température s’étendant de celle de l’azote liquide jusqu’au température ambiante. Les détails des dispositifs expérimentaux permettant d’effectuer les mesures électriques notamment l’estimation de la résistivité et la mesure de bruit basse fréquence sont également exposés dans ce chapitre.

Le troisième chapitre discute les résultats des mesures de bruit de basse fréquence dans les couches d'InN produite par épitaxie aux jets moléculaires (EJM). En ce qui concerne la fabrication des structures par les techniques classiques de la microélectronique (photolithigraphie, dépôt, gravure, *etc*.), nous avons d'abord montré que le recuit thermique devait intervenir après les étapes de la gravure et de dépôt des métaux utilisés pour assurer les contacts électriques.

Le niveau de bruit basse fréquence dans les couches est comparable à ceux publiés pour les semiconducteurs III/V tels que GaAs ou InAs pour lesquels des filières technologiques commerciales existent. Ce résultat montre que la qualité de nos couches en volume est suffisamment bonne pour la fabrication de dispositifs. Par les mesures électriques en température, nous avons également confirmé l'existence d'une conduction de surface qui prédomine à haute température. Aux températures T inférieures à 100K, l’existence d’une conduction électrique volumique a été mise en évidence. Une étude spectroscopique en bruit a revélé l’existence d’un état discret dans la bande interdite situé à 53 meV du minimum de la bande de conduction.

Dans le quatrième chapitre, nous avons mené une analyse détaillée de la microstructure des puits quantiques d'InGaN/GaN. Dans la littérature, il y a eu un nombre d'explications pour l'efficacité d'émission dans le bleu pour ces composants. Il s'agit d'une part des clusters riches en indium qui pourraient aider à localiser les excitons, ou alors des dislocations traversantes qui conduiraient à la formation des défauts en V bordés de puits quantiques inclinés de faible épaisseur. Ces puits constitueraient des barrières de potentiels efficaces empêchant les excitons d'atteindre les cœurs des dislocations. Au cours de cette étude, nous avons analysé la microstructure des puits quantiques avec variation des différents paramètres tels que le nombre de puits quantiques, leurs épaisseurs, la composition nominale d'indium dans les puits. Nous avons observé la formation systématique des défauts en V dans les hétérostructures fabriquées par épitaxie en phase vapeur aux organométalliques (EPVOM). Cependant, dans tous les échantillons analysés, il n'y a aucune influence de ces défauts sur la largeur des puits. Il est donc clair que l'émission dans nos dispositifs ne peut pas profiter d'effet bénéfique de barrières autour des dislocations. Par ailleurs, nos puits de fabrication par EPVOM présentent une meilleure morphologies que ceux obtenus par EJM (uniformité en épaisseur), ce qui est corrélé avec la plus forte émission (intensité et largeur à mi-hauteur des pic d photoluminescence). D'après les mesures de la contrainte dans les images HRTEM, nous obtenons des fluctuation locales de la composition en indium, par contre, les compositions moyennes sont accord avec les longueur d'onde de luminescence.

Le cinquième chapitre donne les conclusions de ce travail et indique quelques pistes de perspectives.

En ce qui concerne l'analyse des propriétés des couches d'InN, nous avons obtenu les résultats suivants :

- Le niveau de bruit à basse fréquence utilisé comme figure de mérite indique que nos couches d'InN pourraient donner des dispositifs aussi performants que ceux basés sur d’autres semi-conducteurs III/V tels que GaAs, ou InAs.
- Dans notre étude du bruit en fonction de la température, les couches de InN présentent une transition du comportement semi-conducteur/ métal autour de 130 K.
- L’analyse du bruit de 1/f en fonction de la température indique que la conduction de surface est prédominante au-dessus de 100 K.
- Aux températures inférieures à 100 K, un bruit lorentzien apparaît en plus des bruits 1/f et blanc. Ce nouveau type de bruit a été attribué à un processus de génération et recombinaison des porteurs par un niveau piège dont nous déterminé l'énergie d'activation à 50 meV au dessous de la bande de conduction. Ces résultats montrent donc, qu'en dessous de 100 K, il y a une contribution supplémentaire à la conduction électrique en plus de la conduction de surface. En d'autres termes, nous avons pu accéder à la conductivité de volume dans nos échantillons grâce aux analyses du bruit.

Pour l'émission dans les hétérostructures d'InGaN/GaN, les puits quantiques avaient une épaisseur de 1 nm à 3 nm, avec les compositions d'indium nominales de 20 à 25%, les longueurs d'ondes d'émission allaient du violet au vert.

- Nous avons mis en évidence que des barrières de GaN dopés Silicium, avaient des interfaces abruptes dans une monocouche atomique.
- Les défauts en V se sont formés dans la croissance des puits par EPVOM mais l'épaisseur des puits n'a pas été modifiée au voisinage de la dislocation.
- La plus forte intensité mesurée dans les échantillons de EPVOM par rapport à ceux de EJM a été corrélée avec la morphologie des puits.

Questions ouvertes et suggestions de poursuite au niveau des couches d'InN

- Même si nous avons pu avoir accès à la conduction des charges aussi bien surface qu'en en volume, il reste encore faire cette séparation de façon quantitative.

- En utilisant des modèles simples, nous avons pu montrer que les fluctuation de mobilité provenaient du volume des couches d'InN, il faudra rapidement vérifier ce fait par des mesures de mobilité par effet Hall.

- Bien sûr, notre démarche sera confortée lorsqu'on aura utilisé les mesures de bruit basse fréquence pour avoir accès à la conductivité électrique dans des couches d'InN dopées p.

Comment compléter ce travail pour les puits quantiques InGaN/GaN

- Pour confirmer le rôle des défauts en forme de V, il faudrait déterminer l'efficacité quantique des puits que nous avons étudiés.

- Lorsque nous avons fait des essais en microscopie en balayage et transmission très haute résolution, les compositions en indium que nous avons obtenu se sont avérées toujours inférieures aux nominales. Cette sous-estimation systématique demande un travail minutieux additionnel pour en comprendre les raisons. En effet, cette technique devrait être la plus précise actuellement disponible pour ce type d'analyse locale.

Introduction

For the last two decades, the nitride semiconductors (AlN, GaN, InN) have been under extensive investigations due to the numerous applications, which span from Light Emitting Diodes LEDs (for solid state lighting), high power and high frequency components. The research effort has even more increased by 2002, when the band gap of InN has been re-evaluated as 0.65 eV instead of the earlier 1.89 eV. With the new band gap, the applications of the nitride semiconductors family should include multicolour LEDs through the whole visible range (true colour), as well as the highest efficiency heterojunction solar cells. Additionally, with an electron mobility of over 4000 $cm^2V^{-1}s^{-1}$ and very high saturation velocities, InN provides an ideal material platform for the development of electronic transport devices operating up to the terahertz range. To ensure the reliability of commercial devices, a large fundamental research effort is required to establish the optimal growth mechanisms and maximise the electronic and optical performance of this exciting material. As of today, group III-nitrides have gained a significant position in the science and technology of compound semiconductors, as well as in modern electronic and optical devices. Though InN is novel, still many of its properties are poorly known, and much research work is still needed to bring about this knowledge.

In this scope, the contribution of my PhD research is on the “structural, optical and electronic properties of InN films and In heterostructures”. This work was carried out in CIMAP and GREYC laboratories in Caen within the framework of ‘RAINBOW ITN’ European project entitled as “High quality material and intrinsic properties of InN and indium rich nitride alloys”. This manuscript relates a detailed study on transport properties of Plasma Assisted Molecular Beam Epitaxial InN layers, as well as Transmission Electron Microscopy (TEM) and photoluminescence studies of InGaN/GaN Quantum Wells (QWs).

Despite the novel properties of InN, there is still a hindrance for device applications because of an intrinsic charge accumulation at the surfaces. The first target to deal was the issue of bulk electrical conduction in InN thin films. Low frequency noise (LFN) measurements were used as a tool to access the bulk conductivity in InN layers which is crucial to achieve for device applications.

In spite of having huge defect densities $\geq 10^8$ cm^{-2} in the thin films, InGaN/GaN QWs exhibit a higher efficiency in comparison with GaAs based devices. In this scope, the target of this work was to address the issue of the origin of high emission efficiency for solid state lighting applications. So in this context, efforts were dedicated to characterize the structure and morphology of the QWs, to determine how they are affected by the growth conditions and to relate this with the optical properties.

The manuscript starts with a brief overview of growth, properties and applications of group III nitride semiconductors, along with an introduction to the concept of low frequency noise.

The **second chapter** gives a description of the growth and the experimantal techniques used for characterizing the samples.

The **third chapter** describes a brief review of related work done in InN transport properties and emphasizes on electrical conduction in InN layers with LFN technique. Indeed, we have been the first to use the LFN technique to probe bulk conduction in InN layers.

The **fourth chapter** has been focused on investigating the possible origin of "High optical efficiency on InGaN/GaN QWs". It gives an overview of the existing explanations about the origin of high optical efficiency in these QWs. Following the literature, we have systematically studied TEM and optical properties with a variation of parameters such as number of QWs, thickness of QWs, nominal In composition and PL peak emissions. Finally, the TEM observations and its correlation with optical properties give light on the origin of high optical emission in these QWs.

The **last Chapter** summarizes the results and presents some future challenges in relation to this work.

Chapter 1

Introduction to III-nitride semiconductors and low frequency noise

The two aims of this dissertation were to improve the quality of materials and to expand the arena of nitride based devices. A fundamental requisite of a material for device applications is to have a complete knowledge about its intrinsic properties. So the first section of this chapter briefly describes the main properties of group III nitride semiconductors. The second part introduces the basic concepts of low frequency noise (LFN) to understand the upcoming chapters on LFN.

1.1 Brief History of Nitrides

Group III nitrides are one of the most adequate semiconductor families for the optoelectronic, high temperature and high power electronic devices. The fundamental bandgap range of III-nitride alloy system is the widest of all known compound semiconductors, extending from InN (0.7 ± 0.05 eV[1], near IR), to GaN (3.4 eV, mid UV) and finally to AlN (6.2 eV, deep-UV)[2]. Thus group III nitrides can be used for optoelectronic applications ranging from the near infrared to the deep ultraviolet spectral region [3] .Group III nitrides can operate at high temperatures and hostile environments which allow them to be used in space and nuclear reactors where Si and GaAs technologies fail to compete3.

The history of research in group III nitrides dates effectively from about 100 years. The first synthesis of AlN, GaN and InN were reported in 1907[4], 1910[5] and 1932[6] respectively. However it took decades to receive significant research attention. In 1970's a significant advance took place in GaN research by the growth of GaN epitaxial layers on sapphire substrates using Hydride Vapor Phase Epitaxy (HVPE)[7], Molecular Organic Vapor Phase Epitaxy (MOVPE)[8] and Molecular beam epitaxy[9]. The interest in these materials was outburst with the achievement of p-type doping[10,11] which initiated the advent of violet to yellow LEDs[12,13,14], laser diodes[13], UV LEDs[14,15]. The development of InGaN based solar cells is also one of the emerging field of research in III-nitrides[16]. An additional effort has been made towards High Electron Mobility

Transistors (HEMTs) based on nitride heterojunctions[17]; and intense research activity has been dedicated towards the application of III-V nitride materials in high power, microwave-frequency electronic devices[18,19]. The large breakdown fields and high saturation velocities make the nitrides ideal for producing high power HFETs and a full range of unipolar and bipolar devices[20,21].The transport properties of InN are better than those of GaN, which tops InN as the material most adequate for device applications in the ultra-high speed area[22].

1.2 Properties of III nitride semiconductors

1.2.1 Crystalline structure

The three (Al, Ga, In) nitride compounds and their alloys may occur in three configurations namely: Wurtzite (hexagonal), Zinc blende (cubic) and rock salt. The Wutrzite structure (shown in Figure 1.1) is the most stable one[23,24]. It consists of two hexagonal close packed sublattices of group III metal and nitrogen atoms respectively. Crystals with wurtzite structure belong to the space group of $P6_3mc$. The two sublattices are constituted by one atomic species, resulting in four atoms per unit cell and are shifted along [0001] $\vec{c}$ - axis by $u=3c/8$. Each atom of one kind is surrounded by four atoms of the other kind which are arranged at the edges of a tetrahedron. The hexagonal unit cell as shown in Figure 1.1b, is defined by the axis a of the basal hexagon along [11$\bar{2}$0] axis, height c of the hexagonal prism along the [0001] axis, and the anion-cation bond length u along the [0001] axis.

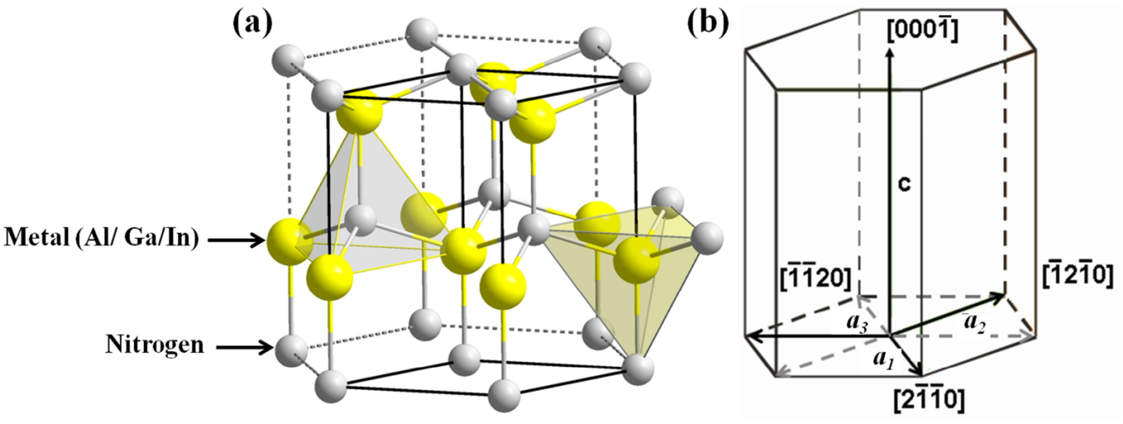

Figure 1.1. (a) Illustration of atomic distribution in wurtzite structure[25]. (b) Hexagonal unit cell. Where a_1, a_2 and a_3 are base vectors.

The anion-cation bond length is significant in consideration as it changes with different cations and ionic radii[26]. In a hexagonal system, the notations for the four indices (h k i l) is assigned to the three base vectors $\overrightarrow{a_1}$, $\overrightarrow{a_2}$, $\overrightarrow{a_3}$ and $\vec{c}$ respectively. The third index i is defined as, $i = -(h+k)$ and these base vectors are separated by 120°.

The lattice parameters of group III nitride binary systems are given in Table 1.1. In case of ternary compounds (e.g. $A_xB_{1-x}N$), the lattice parameters can be deduced by using Vegard's law:

$$a_{AB} = xa_A + (1-x)a_B \tag{1.1}$$

The lattice mismatch in a heterostructure is measured by a misfit parameter (f_m) defined as,

$$f_m = \frac{f_1 - f_2}{f_1} \tag{1.2}$$

where f_1 and f_2 are the lattice parameters of the two material systems. In case of ternary system, for example $In_xGa_{1-x}N$ grown on GaN, its lattice constants depend on the composition x. Assuming that Vegard's law is valid, the lattice constant $a_l(x)$ of the alloy epilayer is given by

$$a_l(x) = a_{GaN} + (a_{InN} - a_{GaN})x \tag{1.3}$$

Now the misfit parameter is also a function of the alloy composition x, *i.e.*, $f_m = f_m(x)$[2].

Table 1.1. Lattice parameters and lattice mismatch of bulk InN, GaN and AlN at room temperature[24].

Parameters (Å)	**InN**	**GaN**	**AlN**	**Heterostructure**	**Lattice mismatch along *a* parameter**
a	3.54	3.189	3.112	InN/GaN	11 %
c	5.705	5.185	4.982	GaN/AlN	2.3 %
u	0.377	0.376	0.380	InN/AlN	13.7%

1.2.2 Crystal polarity

The group III nitrides are not centrosymmetric crystal structures, as a result, the two crystallographic directions [0001] and [000$\bar{1}$] are not equivalent. Conventionally, the [0001] polarity is defined by the direction of the vector associated to the metal (Al/Ga/In)- nitrogen(N) bond as shown in Figure 1. 2. The epitaxial layer grown along this direction is called metal polar and the material grown in the opposite direction is called nitrogen polar. Hence the metal polar and nitrogen polar structures are the mirror images to each other. The two different polar materials possess distinct properties in terms of surface morphology, chemical reactivity, thermal stability and even the growth conditions. For instance, metal-polarity surfaces are more chemically stable than nitrogen polarity surfaces[27,28].

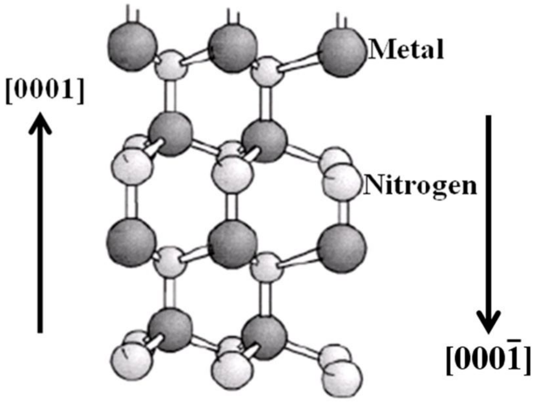

Figure 1. 2. Polarity in Group III nitride: Metal polar along [0001] and Nitrogen polar along [000$\bar{1}$][29].

The realization of the two polarities of this Group III nitride system *i.e.* metal polar or N-polar, is especially sensitive to the chosen substrate material and the applied growth technique as well[30]. The polarity of the films can be probed by various techniques like wet chemical etching, electron microscopic techniques such as Convergent Beam Electron Diffraction (CBED) patterns, Co-Axial Impact Collision Ion Scattering Spectroscopy (CAICISS) and recently hydrogen irradiation has been proposed to effectively determine the polarity[27].

1.2.3 Dislocations

Dislocations are linear defects which arise from the imperfections in the crystalline structure. A material system is often prone to have dislocations irrespective of homo or hetero epitaxy. These dislocations are generated to relax the stress which arises during the growth and to decrease the global energy of the material system. These dislocations can strongly affect the device performance[31,32]. The origin of dislocations is the difference of lattice parameters and thermal expansion coefficients of the substrate and the epilayer. The dislocations are characterized by their Burgers vector ($\vec{b}$) and dislocation line ($\vec{u}$).

In group III nitride epitaxy, the most common dislocations are Threading Dislocations (TDs)[33,34] generated at the interface of the substrate and propagating up to the surface of the layer. A dislocation can either be perfect or partial. A dislocation is said to be perfect, when its Burgers vector corresponds to an entire translation of the lattice; it is partial when the Burgers vector is a fraction of a translation of the lattice. In nitride layers grown along *c*, the main defects are TDs (shown in table 1.2), which forms as edge, screw or mixed type and are distinguished by the angle made between the burgers vector and the dislocation line.

(1) For a pure **edge type** dislocation, the dislocation line is perpendicular to Burgers vector ($\vec{b}$). A schematic diagram of atomic planes can be used to illustrate lattice defects such as dislocations. The "extra half-plane" concept of an edge type dislocation is shown in Figure 1.3.

(2) For a **screw type** dislocation, the dislocation line is parallel to Burgers vector as shown in Figure 1.3.

(3) For a **mixed type** dislocation, there does not exist a particular well defined angular relationship between the dislocation line and the Burgers vector.

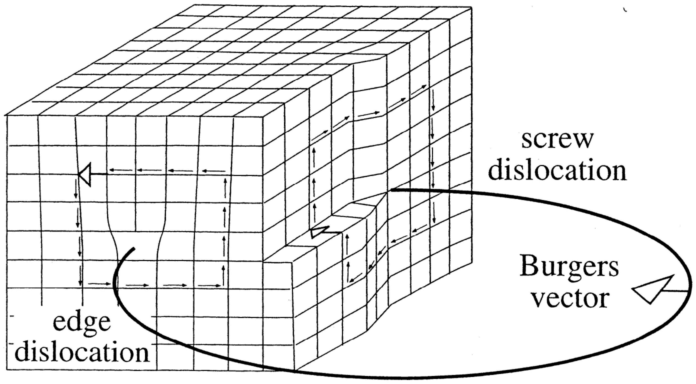

Figure 1.3. A schematic diagram showing, edge and screw dislocation[35].

Table 1.2. Perfect and partial dislocations in group III nitride layers, with lines along [0001] direction[32, 33].

Burger vector ($\vec{b}$)	**Type of dislocation**	**Character**
1/3<11$\bar{2}$0>	Edge type *(a)*	Perfect
<0001>	Screw type *(c)*	Perfect
1/3<11$\bar{2}$3>	Mixed type *(a+c)*	Perfect
1/3<1$\bar{1}$00>		Shockley partial
1/6<20$\bar{2}$3>		Frank-Shockley partial
1/2<0001>		Frank partial

1.2.4 Spontaneous and piezoelectric polarization

As the wurtzite structure is polar, there exists a non zero dipole moment, which gives rise to spontaneous polarization ($\overrightarrow{P_{sp}}$) along the polar directions. Piezoelectric polarization is generated by stress from a lattice mismatch or changes in the anion-cation bond length, which changes the whole lattice structure as shown in Figure 1.4. The total polarization field inside the wurtzite crystal is the sum of spontaneous polarization and piezoelectric polarization.

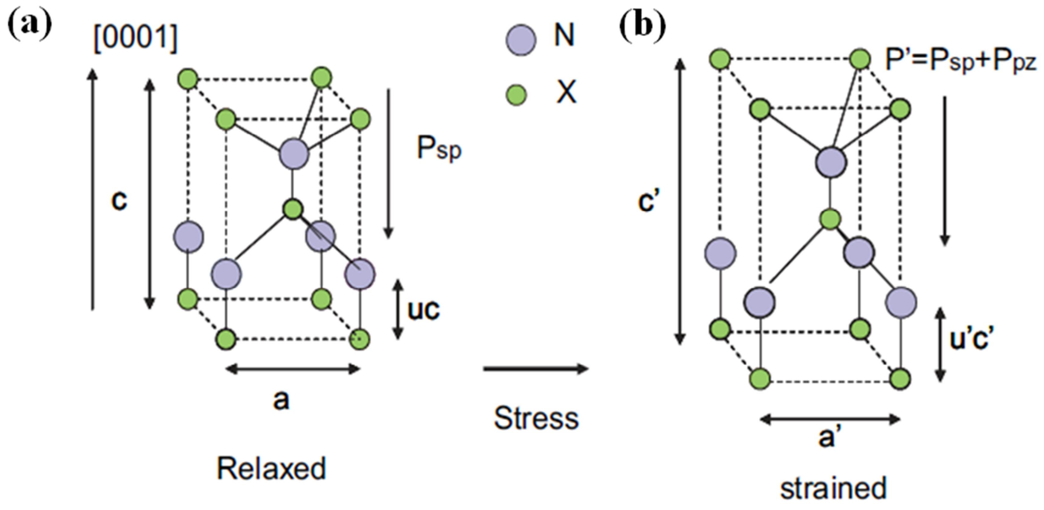

Figure 1.4.(a) Spontaneous and (b) piezoelectric polarization along [0001] direction in wurtzite structure[36].

The values of spontaneous polarization[37,38] is presented in the table 1.3 for the three binary compounds.

Table 1.3. Spontaneous polarization for group III nitrides[37,38].

Material Polarization C/m^2	**InN**	**GaN**	**AlN**
P_{sp}	-0.042	-0.034	-0.090

The magnitudes of the polarization components have different values for various material combinations in heterostructures. For example, in InGaN/GaN system, the lattice mismatch increases steeply with the indium content, so that the resulting piezoelectric polarization dominates rapidly over the spontaneous polarization, whereas in AlGaN/GaN the lattice mismatch is smaller and spontaneous polarization is always dominant or at most comparable to piezoelectric polarization. These polarizations are known to affect considerably the operation of various III-nitride optoelectronic and electronic devices. However, the effects due to polarization can either be eliminated or reduced by appropriately choosing growth orientations such as non polar or semipolar directions.

Quantum Wells (QWs)

A QW is a thin layer which can confine carriers into two dimensions. This is obtained in semiconductors, by fabricating a heterostructure in which a material with a specific band gap is sandwiched between layers of material with a wider band gap. If this thickness of the QW is of the order of Bohr radius (3.4 nm), the energy levels inside will be quantized and their distance increased further as the well width decreases, which is known as quantum confinement energy. This quantum confinement leads to overlap of electron and hole wave functions, which in turn enhances the recombination and transition rate of these carriers. With increasing well width, the transition energy of a QW is expected to converge towards the bandgap of bulk material[39]. For instance in InGaN/GaN QWs, the emission energy is a function of well thickness and indium concentration. When QW structures are grown along the [0001]-direction, as the nitrides are piezoelectric material, a large strain-induced piezoelectric field is expected to be present. This internal electric field which alters the band structure of these heterostructures (shown in Figure 1.5) is called the Quantum Confined Stark Effect (QCSE).

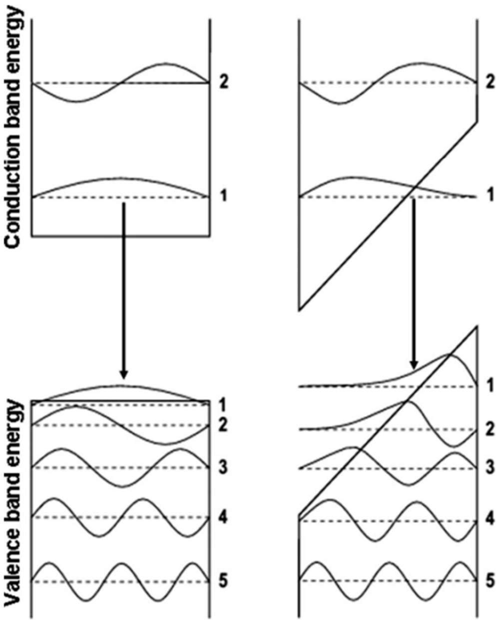

Figure 1.5. Electronic band structure of quantum well under applied bias showing QCSE, resulting in effective bandgap narrowing and spatial separation of electron and hole wave functions[40].

The primary effect of QCSE is the shift of energy levels to lower levels: the first electron level in the conduction band and the first hole level in the valence band get closer in energy. This results in a red shift of the emission[41] in addition to reduction of oscillator strength[42, 43]. There is an adverse affect on emission efficiency due to the reduction of oscillator strength whereas this strong in built internal field is advantageous in GaN/AlGaN system to fabricate high electron mobility transistors.

The other structural, electronic, thermal and optical properties of wurtzite AlN, GaN and InN are listed in Table 1. 4.

Table 1. 4. Physical properties of III nitride materials[2, 3, 44, 45].

Parameter	**AlN**	**GaN**	**InN**
Mass density (gcm^{-3})	3.23	6.15	6.81
Thermal conductivity (W/cm K)	2.85	2.06-2.1	0.8
Thermal expansion (X 10^{-6} K^{-1})	$\Delta a/a$ =4.2 $\Delta c/c$ =5.3	$\Delta a/a$ =5.59 $\Delta c/c$ =3.17	$\Delta a/a$ =3 $\Delta c/c$ =4
Refractive index	2.15 ± 0.05	2.33	2.8-3.05
Dielectric constant	€$_0$ = 8.5 ± 0.2 €$_\infty$ = 4.68 - 4.84	€$_0$ = 9.5 €$_\infty$ = 5.35	€$_0$ = 15.3 €$_\infty$ = 8.4
Electron effective mass (m_e)	0.48	0.2	0.06
Electron concentration (cm^{-3})	$< 10^{16}$	$\sim 10^{17}$	10^{16}- 10^{20}
Electron mobility (cm^{2}V^{-1}S^{-1})	300(Theoretical) 426(Experimental)	1000(Theoretical) 900(Experimental)	4400(Theoretical) 3980(Experimental)
Peak drift velocity (X 10^7 cms^{-1})	1.7	2.9	4.2

1.3 Group III nitrides epitaxy

The common growth techniques for III nitrides are Molecular beam epitaxy (MBE), Metal organic Vapor Phase epitaxy (MOVPE), Hydride Vapor Phase epitaxy (HVPE), Sputtering and Pulsed Laser Deposition (PLD). Among them MOVPE and MBE are the most used for device processing and we have employed these techniques to grow the samples which are investigated in this work.

The quality of epitaxial layers depends upon the growth technique, the epitaxial growth mode (homoepitaxial or heteroepitaxial), the substrate used and the processing conditions. The choice of growth technique depends on the desired structure and needs, for example, in case of industrial production, MBE had less success for nitrides than MOVPE. For group III nitrides growth, although bulk GaN and AlN are available, the small size and high cost prevent their wide usage. Therefore, due to the current lack of affordable bulk nitride substrates, group III nitrides are grown by heteroepitaxy. However, a number of research groups and industries are currently pioneered in the growth of bulk nitride substrates[2]. Lattice and thermal mismatch between epitaxial layers and substrates have long been the major challenge in obtaining high quality devices in the III-Nitride material system. The properties of the most commonly used substrates for group III nitrides are listed in Table 1.5, which indicates a large lattice and thermal mismatch between the III–nitrides and the substrates. Because of this mismatch the growth of good quality epilayers is challenging.

1.3.1 Substrates and buffer layers for group III nitrides

For epitaxial growth, one of the major issues is to select the suitable substrate. Generally, close matched substrates are used to reduce the film stress and dislocations in epitaxial films. There are many factors which contribute to select the substrates for group III nitride epitaxy, and no single material possesses all of the desired qualities. The foremost important factors are the lattice parameters and the thermal expansion coefficients of the substrate closely match with the epitaxial film. Furthermore, the substrates must be chemically and mechanically stable at high temperatures. A substrate should be easily available in large wafer size at relatively low cost in order to make production-scale devices. A high thermal conducting substrate increases device lifetime and allows devices to operate at higher power densities. For optoelectronic purposes, the substrate should have a wide band gap and a high refractive index, so that the photons generated in the active layers of the film are not absorbed by the substrate. A number of substrates have been used for Group III nitrides epitaxy and a complete review was reported by Liu et al[44].

Table 1.5. Properties of substrates for III-Nitride growth[44,45,46].

Substrate	**Crystal symmetry**	**Lattice constant Å**		**Lattice mismatch, $\Delta a/a$ (%)**		**Thermal expansion coefficient ($10^{-6}K^{-1}$)**	
		A	*c*	GaN	InN	$\Delta a/a$	$\Delta c/c$
α-Al_2O_3	Hexagonal	4.765	12.982	~16	~30	5.0	9.03
SiC	Hexagonal	3.0806	15.1173	~3.5	~14.8	4.3	4.7
Si	Cubic	a= b= c=5.431		~21	~8	3.59	

1.3.1.1 Sapphire substrate

Sapphire is the most extensively used substrate for growth of the III–nitrides despite of its large structural and thermal mismatch with GaN and InN (shown in Table 1.5). This is supported by the fact that the layers grown on sapphire have, in many cases, better quality and sapphire is easily available up to inches in diameter at relatively low cost. Sapphire substrates are transparent and stable at high temperatures. In general, the quality of the films grown directly (*i.e*., without the buffer layer) on any plane of sapphire is poor. Obtaining a good quality nitride epilayers necessitates the nitridation of sapphire substrates and an insertion of a low temperature intermediate buffer layer. Furthermore, the optical transparency of sapphire is beneficial in back-illuminated detectors and LEDs for lack of absorption. The main drawback of sapphire as a substrate, is the low thermal conductivity, which causes heat management as an important concern for high current density devices[36].

1.3.1.2 Silicon carbide (SiC) substrate

Extensive work has been done on the growth of III– nitrides on SiC substrates[47, 48]. SiC has several advantages over sapphire for InN and GaN epitaxy, which includes a smaller lattice mismatch and higher thermal conductivity. Additionally, SiC has good electrical conductivity which eases to make electrical contacts to the backside of the substrates and thereby simplifies the device structure compared to sapphire substrates. Large good quality SiC substrates are commercially available. Low temperature GaN or AlN buffer layers are also deposited on the SiC substrates before growing the nitrides. The stress developed in the films grown on SiC is smaller than that grown on sapphire, because of less lattice mismatch. SiC is also a polar material which facilitates the growth of single polar nitrides.

1.3.1.3 Silicon (Si) substrate

Generally, nitride-based devices are grown on sapphire, silicon carbide substrates. However, a considerable work has been done on the growth of group III nitrides on Si substrate. The major attractive points of Si as a substrate includes high quality, low cost, availability of large size, good electrical and thermal conductivity. In addition, Si substrate can accomplish the integration of III nitride devices with other Si based electronics. Although the crystal quality of GaN grown on Si is still poorer than that on sapphire and SiC, research on this is in great progress. A low temperature buffer layer of AlN is usually grown on Si before the growth of the main epilayer to avoid the formation of Si_xN_y. The growth of a polar epilayer on nonpolar substrate is more complicated due to the formation of additional defects, such as inversion domains.

1.4 Applications of group III nitrides

The properties of group III nitride binary compounds and alloys make them exclusive for applications in the fields of electronics and optoelectronics. The quest for these applications has led to extensive research work on these materials from the last two decades. The re-evaluation of InN bandgap has even more broadened the spectrum of these applications.

1.4.1 Optical applications

The Solid State Lighting (SSL) technology has the potential to cut the world lighting energy usage by 20% and could contribute significantly to climate change solutions[49]. So the research aims at bringing LEDs solid-state lighting as the next generation of light sources for general illumination, from homes to commercial applications. In this field, research on group III nitride semiconductors is realizing breakthroughs in efficiency and performance in terms of successful launching of nitride LEDs and Laser diodes.

LED applications

Of group III (Al, Ga, In) N system, InN plays a major role in empowering the fabrication of high efficient light emitting diodes by widening the spectral region with the tuning of indium composition as shown in Figure 1.6. In other words the group III nitrides spans from near infra-

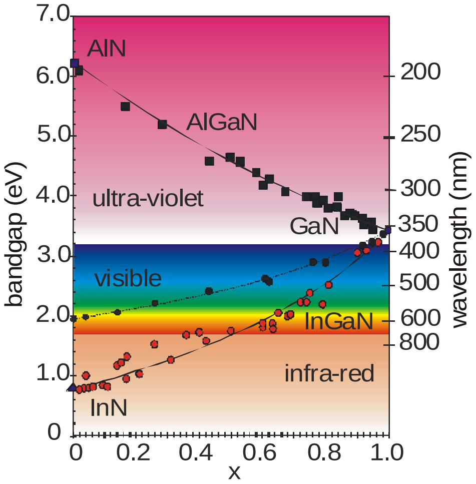

Figure 1.6. (a) Bandgap of all group III nitrides as a function of molar fraction. The solid and dashed lines are bowing curves with best-fit bowing parameters[16].

red to deep ultraviolet region. The research on nitride based LEDs was kindled by the advent of blue/green LED based on InGaN heterostructure grown on sapphire substrate[50]. Thereafter the research in this system was endured by red LED with indium rich InGaN heterostructures and white LEDs which have been developed by coating blue GaN LED with phosphors[51].

Laser applications

The fabrication of high quality LEDs paves the way for the realization of lasers which can operate at light wavelengths from ultraviolet (UV) to green. The blue ray disc technology has replaced the traditional DVDs as the blue laser diodes can allow five times higher storage capacity. A major breakthrough in research has been accomplished by the infrared lasing in high quality single crystalline InN nanobelts[52]. The possibility of making ternary and quaternary nitride systems fosters the semiconductor lasers emitting from deep UV to infrared region.

Emitters and detectors

The wide band gap AlN and GaN binaries posses the potential for fabrication of UV emitters and detectors. UV emitters can be used in various applications such as material identification, forensic location, disinfection and in material processing. These III-nitride based UV detectors finds outmost usage in UV sensing applications such as automobile engine combustion sensing, high temperature flame sensing, environmental monitoring, solar blind detectors, missile plume detection for military use etc. The other most significant application of III nitride semiconductors is in the fabrication of quantum infrared detectors. Photoconductors are the most common type of quantum infrared detectors which can be realized by nitride semiconductors. The narrow band gap of InN and its alloying with GaN makes it perfect for photovoltaic applications. The InGaN ternary system can be tuned to absorb the entire visible range of solar radiation and this could result in high efficiency solar cells.

1.4.2 Electronic applications

The unique properties of InN such as small effective mass, high electron mobilities, and high peak electron velocities make InN promising for electronic devices. InN is of great interest for realization of high speed, high performance, and high frequency devices due to its inherent unique properties. InAlN can be a good candidate for high power, high temperature microwave applications because of its higher breakdown voltages. InN is also ideal for terahertz applications.

1.5 Low frequency noise

The study of fluctuations in physical quantities can yield an insight into the physical phenomena, associated with fluctuations. The spontaneous fluctuations of physical quantities in the domain of electron devices are termed as noise and both terms; fluctuations and noise, are used interchangeably. For the outmost usage of the physical and chemical properties of a material, it is essential to predict the limitations of the device performances. To this end, electrical noise claims to be an accurate indicator of the quality of the materials and devices since it arises from various relaxation processes of the charge carriers, defects, or group of defects[53]. Noise measurement is a diagnostic tool to explore the microscopic and/or mesoscopic properties of materials under study, as noise is sensitive to transport processes; and also noise limits the smallest signal level that can be measured.

In this work, the noise measurements were of considerable interest because of primarily two reasons. Firstly, the noise as a sensitive indicator of material quality, and therefore can be used as a feedback to growers. Secondly, it provides, by comparison with theoretical models, a way to determine the dominant conduction mechanisms.

1.5.1 Noise definition

In the broadest sense, noise is any unwanted signal that comes along with the desired signal. The sources of noise can be classified into mainly two categories. The first is extrinsic noise sources which comes from interactions between the investigated system or device and the external environment which may result from electrostatic or electromagnetic coupling between the circuit and the A.C power lines or fluorescent lights, cross talk between adjacent circuits, humming from D.C. power suppliers or microphonics caused by mechanical vibration of components. Most of these disturbances can often be eliminated or minimized by adequate shielding, filtering or the layout of circuit components[53]. The intrinsic noise is the spontaneous fluctuations which result from the physics of devices and the materials that make up the electrical system. This noise is measured in terms of random fluctuations either in the voltage across the terminals of the device or current flowing through the device and is relative to static values. The noise is randomly distributed in value and sign fluctuations are small compared to static values. From signal point of view, it can be represented as a function, ***b(t)*** which is expressed in volt for voltage fluctuations and in ampere for current fluctuations. One typical view of a noise signal is shown in Figure 1.7.

The mathematical properties of this function are the following: considering at an instant $t=t_0$, it can be written as

$$\overline{b(t)}\Big|_{t=t_0} = \lim_{T\to\infty}\frac{1}{T}\int_{t_0}^{t+t_0} b(t)dt = 0 \tag{1.4}$$

and the mean square, $$\overline{b(t)^2}\Big|_{t=t_0} = \lim_{T\to\infty}\frac{1}{T}\int_{t_0}^{t+t_0} b(t)^2dt \tag{1.5}$$

is constant at instant t_0, and is constant for any t_0 and depends on the physical mechanisms at the origin of the fluctuations, the bias level and the frequency range of measurements.

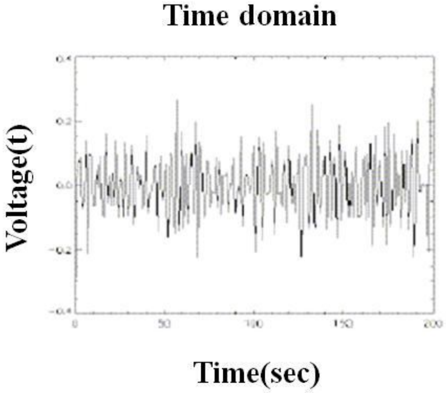

Figure 1.7. A typical view of noise signal in time domain

1.5.2 Noise spectral density

The analysis of noise is more precise in the frequency domain. In the Fourier space, one can define the noise spectral density as

$$S_B(f) = \frac{2}{T_{obs}}|FT\ [b(t)]|^2 \tag{1.6}$$

where $S_B(f)$ is expressed in V^2/Hz for voltage fluctuations and in A^2/Hz for current fluctuations. T_{obs} is the duration of observation of the noise and FT is the Fourier Transform.

Note that, T_{obs} should be sufficiently long, such that the mathematical statistical properties expressed before are approximately verified.

The different contributions can clearly be distinguished when one measures the noise spectral density versus frequency, which is diagrammatically represented in Figure 1. 8 in a log-log scale, where different shapes appear: 1. The white noise, where the noise spectral density is independent of the frequency; 2. Lorentzian noise which consists first in a plateau and then a decrease after a characteristic frequency f_L. Several lorentzian shapes may be observed in one noise spectrum. 3. 1/f noise with a decrease of the noise spectral density that follows a $1/f^{\gamma}$ law. Experimental values of γ between 0.8 and 1.3 have been reported. In our case, γ value was close to 1, so it will not appear in the following.

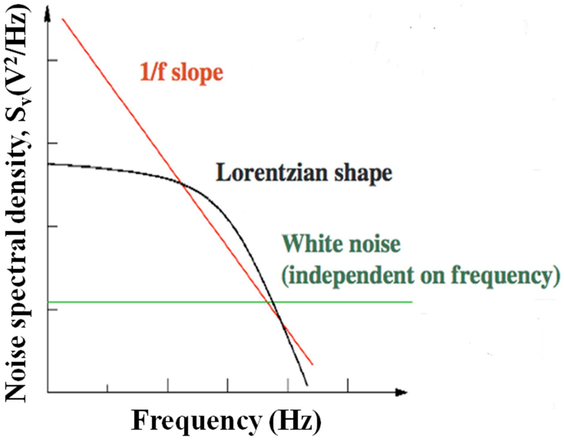

Figure 1. 8. A diagram of the noise spectral density in log-log scale.

Considering the voltage fluctuations, the noise spectral density is expressed as the sum of the three noises, as follows:

$$S_v = A + \frac{B}{f} + \sum_{i=1}^{N_L} \frac{a_i}{1 + \left[\frac{f}{f_i}\right]^2} \tag{1.7}$$

Where A represents the white noise level, $\frac{B}{f}$ is the 1/f noise and the parameter B represents the voltage noise spectral density level at 1 Hz. The third term of the equation contributes a sum of Lorentzian components, with a_i as the plateau value and f_i as the characteristic frequencies.

1.5.3 White noise sources

There are two distinct types of white noise: thermal noise, shot noise.

Thermal noise: It is often termed as Johnson noise or white noise and is caused by the random motion of charge carriers in thermal equilibrium. In every conductor, above the absolute zero temperature, charge carriers are in random motion and this vibration is dependent on temperature.Since the motion is random, at any given time there might be a surge of charge on one side or the other leading to a voltage across the material. For a semiconductor of electrical resistance R at a temperature T, the spectral voltage noise density (S_v) is given as in equation 1.8, which shows that S_v is independent of frequency as can be seen in Figure 1. 8.

$$S_v = 4k_B \mathrm{TR} \tag{1.8}$$

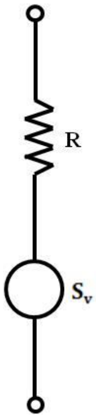

Figure 1.9. Noise representation for a physical resistor[53].

Figure 1.9 represents the thermal noise model by replacing the noisy resistor with the combination of a noise-free resistor in series with a voltage-noise generator.

Shot noise: It arises from discrete carrier motion in devices. The shot noise results from the random emission of charged particles which are discrete and independent. Shot noise can be noticed in Schottky-barriers and in PN-junctions where the current results from the random motion of charged particles. The shot noise spectral density is given by,

$$(S_I)_s = 2qI \tag{1.9}$$

where I is DC bias in amperes and q is elementary charge= 1.6 X 10^{-19} C.

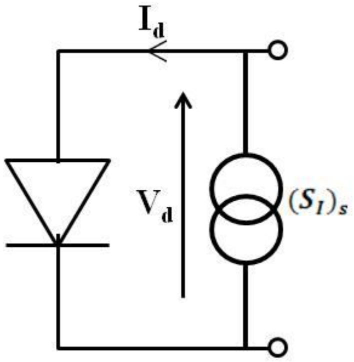

Figure 1.10. Shot noise in a diode: Noise equivalent model.

1.5.4 Lorentzian noise sources

Many kind of mechanisms exists that creates lorentzian shape in the noise spectral density. First order low pass filtering of the white noise sources, popcorn or random telegraph noise for instance. In this work, we have focused on generation recombination (GR) processes of free charge carriers in a semiconductor. Such processes are related to impurities that create a trap level state at energy E_T in the bandgap characterized by a time constant τ. In the noise spectral density the charge carriers generation recombination at such trap level create a lorentzian shape where the characteristic frequency of the lorentzian is $\frac{1}{2\pi\tau}$.

Using result from SRM model[54], a relationship exists between τ and E_T according to the following equation,

$$ln(\tau.T^2) = \frac{E_C - E_T}{k_B T} + ln\left[\frac{h^3}{4\ k_B{}^2\ \sigma_n \sqrt{6\pi^3\ m_e{}^{*\frac{1}{2}}\ m_h{}^{*\frac{3}{2}}}}\right] \quad (1.10)$$

Where h: Planck's constant, $m_e{}^*$: effective electron mass, $m_h{}^*$: effective hole mass, k_B is Boltman constant and σ_n is capture cross section of electrons respectively. By plotting $\ln(\tau.T^2)$ versus $\frac{1}{k_B T}$, one can obtain an Arrhenius diagram. If experimental data are well aligned, from the slope of the linear fit, the energy trap level E_T can be extracted.

1.5.5 1/f noise sources

Whenever a constant voltage is applied to a resistor, a fluctuating component of the current is observed in addition to the thermal noise. Hence it is measured as excess random fluctuations in the voltage when a current flows through the given resistor. The magnitude of these voltage fluctuations is proportional to the current and thus it is measured as fluctuation in the conductivity. 1/*f* noise is also called low frequency noise because it has increasing spectral power at lower frequencies. The GR noise and 1/f noise are often termed as excess noise as they are present in addition to thermal noise and shot noise.

1.5.6 1/f noise models

It is well known that in homogeneous sample, the electrical conductivity (σ), is given by σ = nqμ, where q = 1.6 X 10^{-19} C, n is the free carriers concentration and μ is the free carriers mobility. The conductivity fluctuations in a material can either result from fluctuations in the number of carriers or in their mobility. Thus, 1/f current noise fluctuations can arise from either fluctuations in the number of carriers (ΔN model) or fluctuations in the carrier mobility (Δμ model). Thus the voltage fluctuation spectral density, S_v depends on either number fluctuation spectral density (S_N) or mobility fluctuation spectral density (S_μ), given by

$$\frac{S_v}{v^2} = \frac{S_N}{N^2} \quad \text{or} \quad \frac{S_v}{v^2} = \frac{S_\mu}{\mu^2} \tag{1.11}$$

where *N* is the total number of carriers in a homogeneous semiconductor which is related to the carrier concentration as *N*= n x volume, and μ is mobility of charge carriers.

In chapter 3, the quadratic dependency of S_v versus v is represented as $s_v = \frac{K_v}{f} \cdot v^2$. This relation is used independent of the origin of the fluctuations, whereK_v, gives the noise level at 1 Hz with a DC voltage of 1V which is applied to the resistance.

There is no universal theory for 1/f noise, however, two major competing models are available which will be briefly described in the following sections.

Mobility fluctuations

In this model, it is considered that the carriers scattering due to the lattice vibrations gives rise to the origin of 1/f noise fluctuations[55,56].The mobility fluctuations are connected to the volume effect, as the fluctuations in the mobility of the carriers occur in the bulk of the material which results the observed conductivity fluctuations. By following the semi empirical formula proposed by Hooge, one can write,

$$\frac{S_\mu}{\mu^2} = \frac{\alpha}{fN} \tag{1.12}$$

Where the parameter α is a constant, which is very sensitive to material quality and processing techniques. Thus, it can be used as an indicator to measure the quality and the noise level of materials and devices.

Number fluctuations

Number fluctuations are related to GR centres and as it has already been discussed, GR processes lead to Lorentzian spectrum. One condition for obtaing 1/f noise is to consider GR centres with a distribution of time constants that follows as (1/ τ) law between τ_1 and τ_2. It can then be proved that for frequencies between $\frac{1}{2\pi\tau_1}$ and $\frac{1}{2\pi\tau_2}$, the noise spectral density follows a pure 1/f noise dependency. Interface states allow obtaining such time constant distribution. It follows that number fluctuations, when observed are associated with a surface or an interface localization of 1/ f noise sources.

1.6 References

---

[1] K. M. Yu, Z. Liliental-Weber, W. Walukiewicz, W. Shan, J. W. Ager III, S. X. Li, R. E. Jones, and E. E. Haller, H. Lu and W. J. Schaff, “On the crystalline structure, stoichiometry and band gap of InN thin films”, Appl. Phys. Lett. **86**, 071910 (2005).

[2] S. C. Jain, M. Willander, J. Narayan, and R. V. Overstraeten, “III-nitrides: Growth, characterization, and properties”, J. Appl. Phys. **87**, 965 (2000).

[3] S. N.Mohammad and H. Morkoç, “Progress and prospects of group-III nitride Semiconductors”, Prog. Quant. Electr. **20**, 361 (1996).

[4] F. Fichter, “Uber aluminumnitride”, Z. Anorg. Chem. **54**, 322 (1907).

[5] F. Fichter, and F. Schroter, Berichte der Deutschen Chemischen Gesellschaft, **43**, 1465 (1910).

[6] V.C.Johnson, J. B. Parsons and M. C.Crew, “Nitrogen compounds of gallium”, J. Phys. Chem. **36,** 2588 (1932).

[7] H. P. Maruska, J.J. Tietjen, “The preparation and properties of vapor-deposited single-crystalline GaN”, Appl. Phys. Lett. **15,** 327 (1969).

[8] H. M. Manasevit, F. M. Erdmann and W. I. Simpson, “Use of metalorganics preparation of semiconductor materials; IV. Nitrides of Aluminum and Gallium”. J. Electrochem. Soc. **118**, 1864 (1971).

[9] S. Yoshida, S. Misawa and A. Itoh, “Epitaxial growth of aluminum nitride films on sapphire by reactive evaporation ”, Appl. Phys. Lett. **26**, 461 (1975).

---

[10] H. Amano, M. Kito, K. Hiramatsu, and I. Akasaki, "P-Type Conduction in Mg-doped GaN treated with Low-Energy Electron Beam Irradiation", Jpn. J. Appl. Phys. **28**, L2112 (1989).

[11] S. Nakamura, T. Mukai, M.Senoh and N. Iwasa, "Thermal annealing effects on p-type Mg- doped GaN films", Jpn. J. Appl. Phys. **31**, L139 (1992).

[12] S. Nakamura, M. Senoh and T. Mukai "High-power lnGaN/GaN double-heterostructure violet light emitting diodes", Appl. Phys. Lett. **62**, 2390 (1993).

[13] S. Nakamura, M. Senoh, S. Nagahama, N. Iwasa, T. Yamada, T. Mukai, T. Matsushita, Y. Sugimoto, and H. Hiyoku, "Room-temperature continuous-wave operation of InGaN multi-quantum-well-structure laser diodes with a long lifetime", Appl. Phys. Lett. **70**, 868 (1997).

[14] A. Yasan, R. McClintock, K. Mayes, S. R. Darvish, H. Zhang, P. Kung, M. Razeghi, S. K. Lee and J. Y. Han, "Comparison of ultraviolet light-emitting diodes with peak emission at 340 nm grown on GaN substrate and sapphire", Appl. Phys. Lett. **81,** 2151 (2002).

[15] A. Yasan, R. McClintock, K. Mayes, D. Shiell, L. Gautero, S. R. Darvish, P. Kung and M. Razeghi, "4.5 mW Operation of AlGaN-based 267 nm deepultraviolet light-emitting diodes", Appl. Phys. Lett. **83**, 4701 (2003).

[16] J. Wu, "When group-III nitrides go infrared: New properties and perspectives", J. Appl. Phys. **106**, 011101 (2009).

[17] A. J. Sierakowskia and L. F. Eastman, "Analysis of schottky gate electron tunneling in polarization induced AlGaN/GaN high electron mobility transistors", J. Appl. Phys. **86**, 3398 (1999).

[18] Y. F. Wu, B. P. Keller, P. Fini, S. Keller, T. J. Jenkins, L. T. Kehias, S. P. DenBaars, and U. K. Mishra, "High Al-content AlGaN/GaN MODFETs for ultrahigh performance "IEEE Electron Device Lett. **19**, 50 (1998).

[19] S. T. Sheppard, K. Doverspike, W. L. Pribble, S. T. Allen, J. W. Palmour, L. T. Kehias, and T. J. Jenkins, "High-power microwave GaN/AlGaN HEMTs on semi-insulating silicon carbide substrates " IEEE Electron Device Lett. **20**, 161 (1999).

[20] S.J. Pearton and F. Ren," GaN electronics", Advanced Materials **12**, 1571 (2000).

[21] H. Morkoc, A. D. Carlo, R. Cingolani, "GaN-based modulation doped FETs and UV detectors" Solid-State Electron. **46**, 157 (2002).

[22] A.G. Bhuiyan, A. Hashimoto and A. Yamamoto, "Indium nitride InN.: A review on growth, characterization and properties", J. Appl. Phys. **94**, 2779 (2003).

[23] C.-Y. Yeh, Z. W. Lu, S. Froyen and A. Zunger, "Zinc-blende – wurtzite polytypism in semiconductors", Phys. Rev. B **46**, 10086 (1992).

[24] H. Morkoç, S. Strite, G. B. Gao, M. E. Lin, B. Sverdlov and M. Burns, "Large-band-gap SiC, III-V nitride, and II-VI ZnSe-based semiconductor device technologies", J. Appl. Phys. **76**, 1363 (1994).

[25] http://upload.wikimedia.org/wikipedia/commons/8/8e/Wurtzite_polyhedra.png

---

[26] R. D. Shannon and C. T. Prewitt, “Effective ionic radii in oxides and fluorides”, Acta Crysta B **25**, 925 (1969).

[27] M. A. Mastro, O. M. Kryliouk, T. J. Anderson, A. Davydov and A. Shapiro,“Influence of polarity on GaN thermal stability”, J. Cryst. Growth **274**, 38 (2005).

[28] J. Rouviére, J. Weyher, M. Seelman-Eggebert and S. Porowski, “Polarity determination for GaN films grown on (0001) sapphire and high-pressure grown GaN single crystal”, Appl. Phys. Lett. **73**, 668 (1998).

[29] O. Ambacher, “Growth and applications of Group III-nitrides”, Journal of Physics D: Applied Physics **31**, 2653 (1998).

[30] T. D. Veal, C. F. McConville and W. J. Schaff , “Indium Nitride and Related Alloys”, CRC Press Taylor & Francis Group, Chapter 2 (2010).

[31] T. Sugahara, H. Sato, M. Hao, Y. Naoi, S. Kurai, S. Tottori, K. Ymashita, K. Nishimo, L. T. Romano and S. Sakai,“Direct evidence that dislocations are non-radiative recombination centers in GaN”, J. J. Appl. Phys. **37**, L398 (1998).

[32] D. Cherns, S. J. Henley and F. A. Ponce, “Edge and screw dislocations as nonradiative centers in InGaN/GaN quantum well luminescence”, Appl. Phys. Lett. **78**, 2691 (2001).

[33] X. H. Wu, L. M. Brown, D. Kapolnek, S. Keller, B. Keller, P. DenBaars and J. S. Speck, “Defect structure of metal-organic chemical vapor deposition-grown epitaxial (0001) GaN/Al_2O_3”, J. Appl. Phys. **80**, 3228 (1996).

[34] F. A. Ponce, D. Cherns, W. T. Young, and J. W. Steeds, Characterization of dislocations in GaN by transmission electron diffraction and microscopy techniques. Appl. Phys. Lett. **69**, 770 (1996).

[35] http://www.geology.um.maine.edu/geodynamics/AnalogWebsite/UndergradProjects2010/PatrickRyan/Content/dislocationdiagram.jpg.

[36] A.R.D Yadira, A Ph.D thesis on “Characterization of A-plane Grown GaN on Sapphire Substrates by Electron Microscopy”, Lausanne, EPFL (2009).

[37] F. Bernardini, V. Fiorentini and D. Vanderbilt, “Accurate calculation of polarization-related quantities in semiconductors”, Phys. Rev. B **63,** 193201 (2001).

[38] V. Fiorentini, F. Bernardini and O. Ambacher, “Evidence for nonlinear macroscopic polarization in III–V nitride alloy Heterostructures”, Appl. Phys. Lett. **80,** 1204 (2002).

[39] J. S. Im, A Ph. D thesis on “Spontaneous Recombination in Group-III Nitride Quantum Wells”, Technical University Carolo-Wilhelmina, Brunswick (2001).

[40] J.-H. Ryou, P. D. Yoder, J. Liu, Z. Lochner, H. Kim, S. Choi, H. J. Kim and R. D. Dupuis, “Control of Quantum-Confined Stark Effect in InGaN-Based Quantum Wells”, IEEE Journal of Selected Topics in Quantum Electronics **15**, 4, (2009).

[41] T. Takeuchi, S. Sota, M. Katsuragawa, M. Komori, H. Takeuchi, H. Amano and I. Akasaki , “Quantum-Confined Stark Effect due to Piezoelectric Fields in GaInN Strained Quantum Wells”, Jpn. J. Appl. Phys. **36**, L382 (1997).

---

[42] J.S. Im, H. Kollmer, J. Off, A. Sohmer, F. Scholz and A. Hangleiter,“Reduction of oscillator strength due to piezoelectric fields in GaN/Al*x*Ga12*x*N quantum wells”, Phys. Rev. B **57,** R9435 (1998).

[43] A. Hangleiter, J. S. Im, H. Kollmer, S. Heppel, J. Off, and F. Scholz, “The role of piezoelectric fields in GaN-based quantum wells”, The Third European GaN Workshop, Jadwisin, MRS Internet J. Nitride Semicond. Res. **3**, 15 (1998).

[44] L. Liu and J.H. Edgar, “Substrates for gallium nitride epitaxy”, Mat. Sci. and Engg. R **37,** 61 (2002).

[45] B. Gil, “Group III nitride semiconductor compounds”, Physics and applications, Clarendon Press (1998).

[46] W. Paszkowicz, R. Cerny and S. Krukowski, “Rietveld refinement for Indium nitride in the 105-295 K range”, Powder diffraction **18**, 114 (2003).

[47] S. Tanaka, R. S. Kern and R. F. Davis, “Initial stage of aluminum nitride film growth on 6H-silicon carbide by plasma-assisted, gas-source molecular beam epitaxy”, Appl. Phys. Lett. **66**,1 (1995).

[48] C. D. Lee, Ashutosh sagar, R. M. Feenstra, W. L. Sarney, L.salamanca-riba and J. W. P. Hsu, “Growth of GaN on SiC(0001) by Molecular Beam Epitaxy”, Phys. Stat. Sol. (a) **188,** 595 (2001).

[49] J W. Ortony and C. T. Foxonz, “Group III nitride semiconductors for short wavelength light-emitting devices”, Rep. Prog. Phys. **61**, 1(1998).

[50] S. Nakamura and G. Fasol, “The Blue Laser Diode”, Springer, Berlin, (1997).

[51] D. B. Nicol, A PhD. Thesis on “A novel solid state general illumination source”, Georgia Institute of Technology (2006).

[52] M. S. Hu, G. M. Hsu, K. H. Chen, C. J. Yu, H. C. Hsu, L. C. Chen, J. S. Hwang, L. S. Hong and Y. F. Chen, “Infrared lasing in InN nanobelts”, Appl. Phys. Lett. **90,** 123109 (2007).

[53] C.D. Motchenbacher and F. C. Fitchen, “A book on low noise electronic design”, John Wiley and sons (1973).

[54] W. Scholley, W. Reed and Hall, “Statistics of recombination of holes and electrons”, Phys. Rev. B **87**, 835 (1952).

[55] F. N. Hooge and L. K. J. Vandamme. “Lattice scattering causes 1-f noise”, Phy. Lett. A **66,** 315 (1978).

Chapter 2

Experimental techniques

The chapter outlines the experimental techniques which have been utilized in this dissertation to grow and to characterize the hetero-epitaxial layers. It is organized as follows: firstly the growth techniques are presented followed by the description of the characterization tools.

2.1 Growth Techniques

In chapter 1, we have already mentioned about the different substrates and buffer layers which can be employed in group III nitrides epitaxy. Here we will briefly describe the growth techniques for the epitaxial layers investigated in this dissertation.

2.1.1 Molecular Beam Epitaxy (MBE)

MBE[1] was developed in late 1960s by A.Y. Cho, since then it has evolved into one of the most widely used techniques for producing high purity epitaxial layers. MBE can provide good uniform and atomically sharp interfaces even at substantially low growth temperatures (for instance InN the growth temperature from 420-620 °C depending on the In or N polar[2]). As MBE is operated at high vacuum it provides accurate in-situ monitoring capabilities. Hence, MBE is very suitable for precisely controlling the growth parameters.

The principle of MBE growth essentially consists of atoms or clusters of atoms which are produced by heating up a solid or liquid source. They are then led to impinge on a hot rotating substrate, where they can diffuse and eventually form the desired film. The process takes place in an Ultra High Vacuum (UHV) environment (pressure ~ 10^{-9} mbar). The precursor sources can be shutoff and turned on rapidly using shutters, enabling MBE to make abrupt composition changes within a monolayer.

Nowadays, to take the advantage of liquid and gaseous sources, variations of MBE are used for Group III nitrides as well as for various dopants. There are two variations in MBE which are specific to Group III nitrides: Ammonia MBE and Plasma Assisted (PA) MBE. Ammonia MBE uses ammonia (NH_3) as the nitrogen source and solid sources of In, Ga and Al metals for group III components. However dissociating ammonia to make atomic Nitrogen introduces Hydrogen (H), an impurity for nitride growth. On the other hand, PAMBE uses Nitrogen as the group V source. This necessitates Radio-Frequency (RF) plasma to crack the N_2 and create highly reactive atomic N since the N_2 molecule (unlike NH_3) has a very high thermal stability.

2.1.2 Metal Organic Vapor Phase Epitaxy (MOVPE)

MOVPE[3] is an efficient technique for the growth of Group III nitride heterostructures, quantum wells and superlattices. With this technique one can produce almost atomically sharp interfaces. Its high growth rate, good uniformity, large area and multiple wafer growth has attracted the nitride industry for mass production of devices.

The typical organic precursors for III nitrides are trimethylindium (TMIn) for In, trimethylgallium (TMGa) for Ga, trimethylaluminium (TMAl) for Al and ammonia (NH_3) as the nitrogen source. It is to be noted that, triethyls (In/Ga/Al) can also be used instead of trimethyls (In/Ga/Al). For the growth, the organic precursors are driven on to over hot substrate, with the help of carrier gases like hydrogen and nitrogen where the organic species decompose and react with the atomic nitrogen. In this process molecules of required semiconductor material are produced, which then adsorbs on the substrate surface to produce an epitaxial layer.

MOVPE requires high growth temperature, as it must satisfy the conditions for NH_3 pyrolysis. However, for the growth of InN, this is an inherent disadvantage as it dissociates already below 600 °C.

2.1.3 Epitaxial layers used in this dissertation

The materials mentioned in this dissertation were grown by MBE and MOVPE. The major part of this thesis contains MBE grown samples. The InN samples were grown by plasma assisted Molecular beam epitaxy (MBE) at Instituto de Sistemas Optoelectronicos y Microtecnologia (ISOM), Universidad Politecnica de Madrid (UPM) in Spain. The InGaN/GaN samples, which consist of quantum well structures, were grown by MBE as well as MOVPE techniques at École

Polytechnique Fédérale de Lausanne (EPFL), Lausanne, Switzerland and other samples from Centre de Recherche sur l'Hétéro-Epitaxie et ses Applications (CRHEA),Valbonne, France.

2.2 Samples characterization

The surface of the films was inspected by Scanning Electron Microscopy (SEM). The quantitative information about the surface morphology in terms of roughness (r_{rms}) were investigated by Atomic Force Microscopy (AFM) in the tapping mode. One of the essential parts of this thesis is the micro structural characterization of the thin films, in which the interest was about all kinds of defects in the film itself and in the quality of interfaces between the various heteroepitaxial layers. For such a characterization, Transmission Electron Microscope (TEM) was used. The optical properties were studied by photoluminescence spectroscopy. The electrical transport properties like the electrical resistivity and the low frequency noise were carried out using a semiconductor parameter analyzer (HP 4156B) and a dedicated low frequency noise measurement set-up, including a low temperature four probe equipment (Lakeshore TTP4).

2.2.1 Microscopy techniques

2.2.1.1 Atomic Force Microscopy (AFM)

Atomic Force Microscopy[4,5,6] is a basic technique to determine the surface morphology at atomic resolution and as well as the quantitative surface roughness of thin films. The AFM consists of a microscale cantilever with a sharp tip (probe) mounted at the end of the cantilever and used to scan across the surface of the specimen. The AFM tips are typically made from silicon nitride or silicon with a tip radius of curvature on the order of nanometers.

When the tip is brought into proximity of a sample surface, forces between the tip and the sample lead to a deflection of the cantilever according to Hooke's law. In general, the force acting between the cantilever and the sample is a sum of Vander Waals, electrostatic, magnetic, electrodynamic, chemical bonding and capillary forces, which are compensated by elasticity forces resulting from the cantilever bending and the sample deformation. Typically, the deflection is measured using a laser spot reflected from the top surface of the cantilever into an array of photodiodes. A feedback mechanism is employed to adjust the tip-to-sample distance to maintain a constant force between the tip and the sample. The sample can move in the z direction for maintaining a constant force, and the x and y directions for imaging the surface in Å scale by three piezo crystal sensor which allows driving very precise sample movements. A schematic diagram of AFM is shown in Figure 2.1. There are three scanning modes associated with AFM, namely; contact mode, non-contact mode and tapping mode. In the contact mode, the tip is static and in contact with the sample and the image is obtained by repulsive forces between the tip and the sample. This technique can often damage either the sample surface or the tip. In non-contact mode, the tip oscillates above the surface, and the image is obtained from the attractive forces between the tip and the sample. In tapping mode, the image is obtained by the tip, which just taps the surface for small periods of time. This method lessens the damage done to the surface and the tip compared to the case of contact mode. An important parameter which characterizes the surface of thin films is the roughness. The rms (root mean square) roughness is the standard deviation of the ***z*** values in a given area. It is calculated by the AFM software which processes the acquired images.

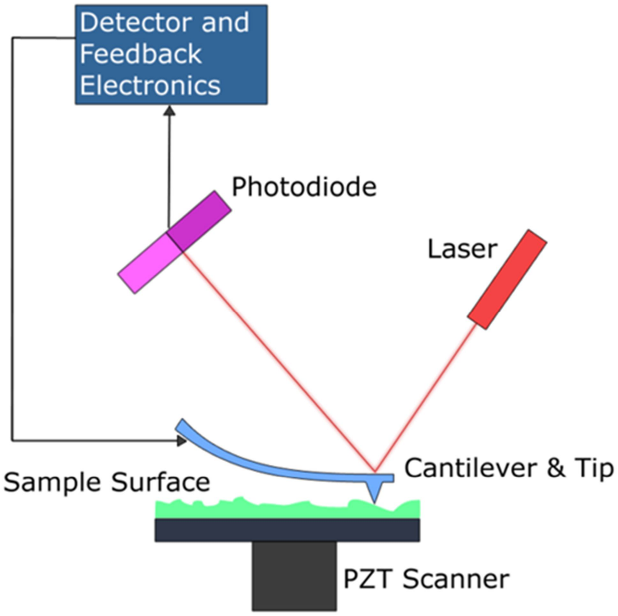

Figure 2.1. A schematic diagram of AFM with components[5].

All the AFM images in this work, which will be shown in the preceding chapters, were obtained in tapping mode using a Nanoscope III (Digital Instrument) atomic force microscope with a silicon tip (10 nm of radius of curvature).

2.2.1.2 Electron microscopy

In the Electron Microscope[6,7], a beam of high energy electrons is used to illuminate the object and a magnified image is formed using electromagnetic lenses. The observations can yield the information about the topography, morphology, composition and structure of the specimen.

Interaction of electrons with matter

When an electron beam hits a specimen, several phenomenons occur as depicted in Figure 2.2. These phenomenons are interconnected and all of them depend to some extent on the topography, structure, atomic number and chemical composition of the specimen. Each signal can be employed to extract different information as illustrated in Figure 2.2.

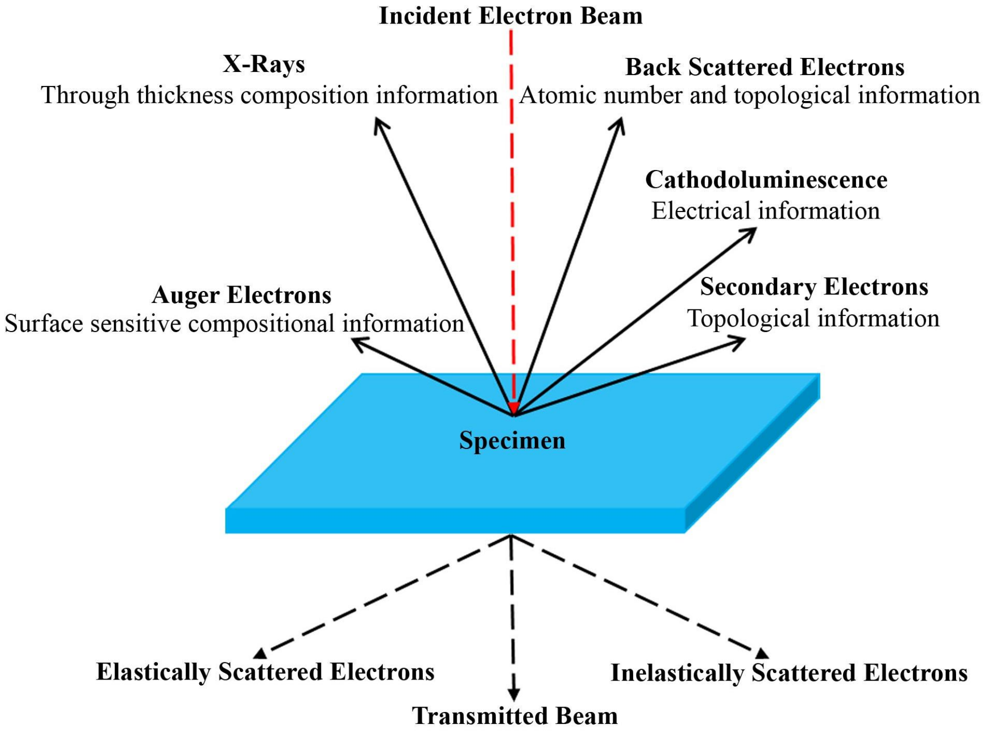

Figure 2.2. The signals generated by interaction of electron beam with a specimen[7].

The Back Scattered Electrons (BSEs) constitute a fraction of the incident electrons and their quantity depends on the atomic number of the scattering atomic nucleus *i.e.* heavier the nucleus, greater the number of back scattered electrons. The BSEs may be used to detect contrast between areas with different chemical compositions. BSEs can also be used to form Electron Back Scatter

Diffraction (EBSD) image which can yield the crystallographic structure of the specimen. The main topography information is obtained from secondary electrons in the Scanning Electron Microscopy (SEM). The elastically scattered electrons are the major source for image contrast in Transmission Electron Microscopy (TEM) techniques such as bright and dark field TEM images. The inelastically scattered electrons are used for analytical electron microscopy, such as electron energy loss spectroscopy, X-ray microanalysis, Scanning Transmission Electron Microscopy (STEM), energy dispersive spectroscopy and cathodoluminescence.

2.2.1.2.1 Scanning Electron Microscopy

SEM[8] is the most widely used form of electron microscope in the field of materials science for surface analysis of bulk materials and thin films. SEM uses a focused beam of high-energy electrons to generate a variety of signals at the surface of solid specimens. The signals that derive from electron-sample interactions reveal the information about the sample including external morphology (texture), chemical composition etc. Areas ranging from approximately 1 cm to 5 microns in width can be imaged in a scanning mode using conventional SEM techniques (magnification approximately 300,000 X, spatial resolution of 10 nm)[9]. This technique is simple with the possibility of large area observation and it does not involve complex sample preparation unlike TEM. The schematic diagram of SEM is shown in Figure 2.3.

In SEM, the electrons with energy ranging from 0.2 keV to 40 keV are generated by a thermoionic or field emission gun and are accelerated by a high potential difference and collimated to a sharp beam. Cathodes like W or LaB_6 are used for thermionic emission while W or ZrO are used for field emission[12]. The electron beam is made to raster the surface of the sample under observation. The high energetic beam undergoes interactions with the specimen, giving rise to many signals such as the secondary electrons (see in Figure 2.2), which are then turned to electrical signal and gives the information about the topography and the morphology of the specimen. The secondary electron yield depends on many factors, and is generally higher for high atomic number targets, and at higher angles of incidence[10].

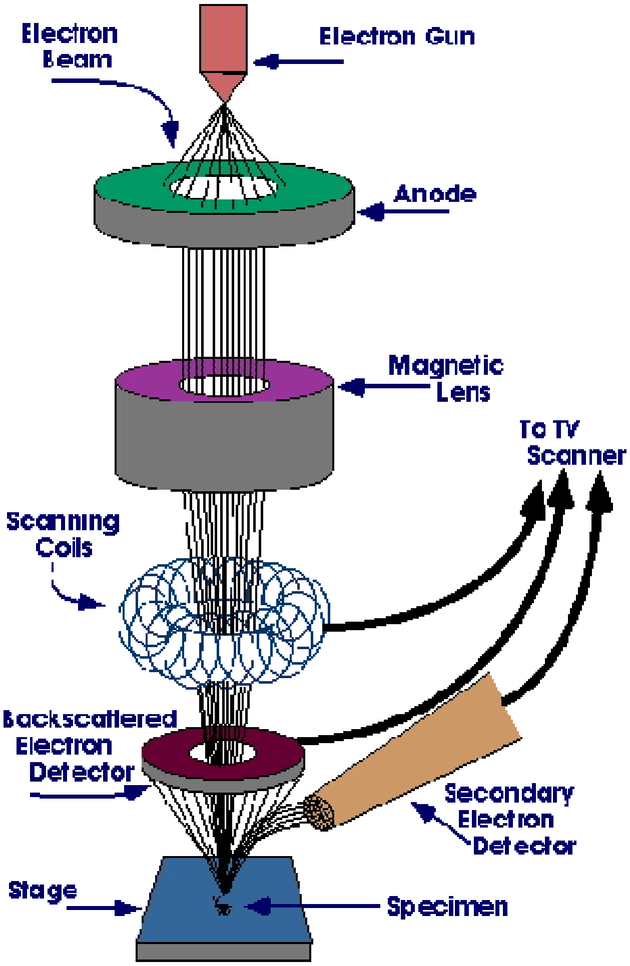

Figure 2.3. Schematic diagram of a SEM set-up[11].

The SEM images were taken with ZEISS SUPRA 55[12] on InN heterostructures. In this case, we have used field emission cathode (W) for generating the high energetic electrons.

2.2.1.2.2 Transmission Electron Microscopy

TEM[7] is a versatile instrument, which is capable of characterizing the internal structure of materials with a wide range of imaging and analytical methods. The major advantage of using a TEM rests on the fact that real and reciprocal space information is available simultaneously at various length scales. Small sampling volume, specimen preparation for TEM are the main drawbacks and radiation damage due to high incident beam energies can be a cause of concern depending on the system under investigation. Despite of these limitations, TEM has emerged as a powerful tool for materials science, as it offers a wide range of complementary information (crystallographic information about defects, strain, interfaces and boundaries). These informations are available as a result of different operation modes and imaging techniques, like Bright Field (BF), Dark Field (DF), Selective Area Electron Diffraction (SAED) and High Resolution TEM (HRTEM). In TEM, we consider the scattering of high energy electrons, whose accelerating voltage is ≥ 50 kV and having small scattering angles, which obeys Bragg´s law, and we also consider very thin crystals of thickness about zero to less than 500 nm.

This section presents a short review of the instrument, modes of operation and analytical procedures in TEM.

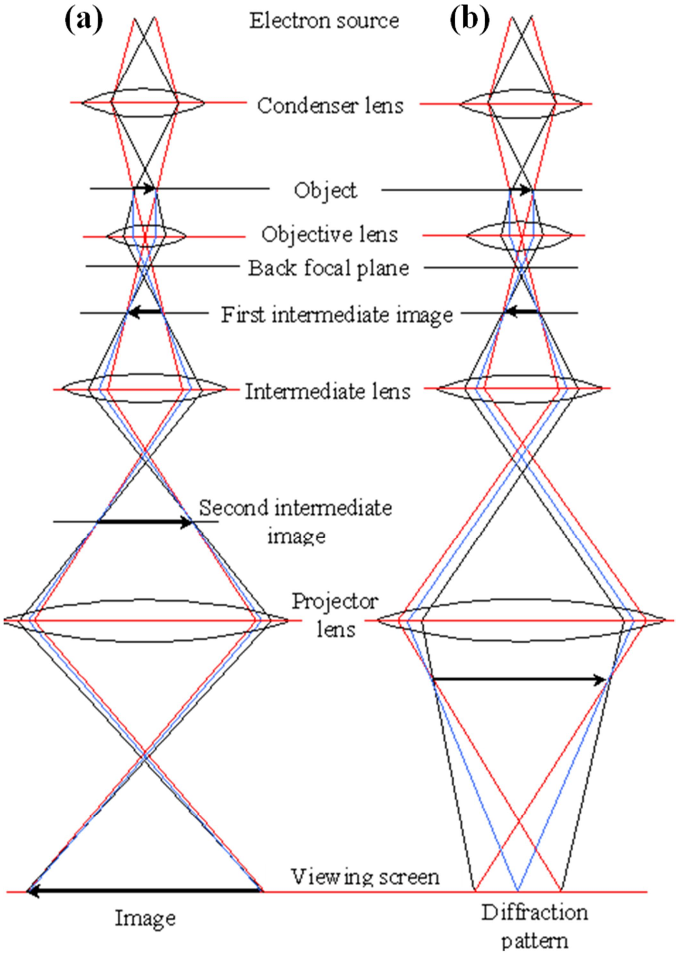

Figure 2. 4. The two basic operations of TEM imaging system (a) imaging mode, (b) diffraction mode[13].

TEM mainly consists of four types of lenses which are condenser, objective, intermediate and projector lenses, are shown in Figure 2. 4. The condenser lens controls how strongly the electron beam is focussed onto specimen. The objective lens forms the image of the specimens. The intermediate lens is used to magnify the image or the diffraction pattern, which is formed in the focal plane of the objective lens. And finally the projector lens is used to control the magnification of final image or the diffraction pattern which may be collected on a fluorescent screen, CCD cameras and electron sensitive plates.

The TEM can mainly be operated in two modes: diffraction mode and imaging mode, the corresponding ray diagrams are shown in Figure 2. 4 (a) and (b) respectively.

Diffraction mode

When the electron beam passes through the sample, it experiences scattering as a result of an interaction of the beam with crystal structure of the specimen. The elastic scattered electrons suffers small scattering angles and which obeys Bragg´s law ($2d_{hkl}\theta = \lambda$). The scattered beams from the same set of atomic planes are brought to one diffraction spot in the back focal plane of the objective lens (diffraction plane), in which the central spot corresponds to the transmitted beam and the other spots originate from the diffracted beams as shown in Figure 2. 4(b). It is possible to select a specific spot or set of spots from the diffraction pattern for generating different images (will be explained in the next section). The control of the diffraction spots is achieved by tilting the sample to a desired orientation.

Imaging

Bright or Dark field imaging modes

Bright Field (BF) and Dark Field (DF) imaging techniques are employed to form images using the transmitted beam or a diffracted beam as shown in Figure 2.5. When the direct beam is selected by the objective aperture, we form the BF image whereas the selection of diffracted beam gives the DF image. Usually, the DF images are obtained by a slight tilting the incident beam to have the diffracted beam on the optical axis, thus minimizing aberrations.

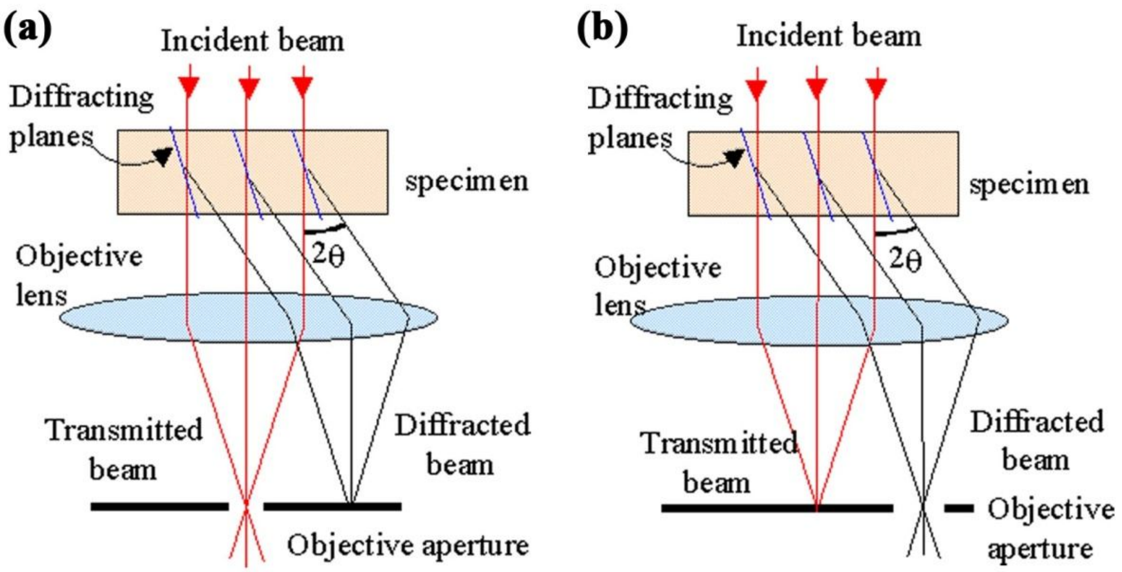

Figure 2. 5. Ray diagrams for: (a) Bright Field image and (b) Dark Field image[14]

High resolution TEM imaging

High resolution imaging is used for direct observation of the sample lattice at atomic resolution. The contrast in high resolution is due to the interference of the transmitted and diffracted beams; it is called phase contrast, in other words, more than one beam is required for phase contrast imaging. In phase contrast, the electrons wave experiences a phase shift, as they interact with the atoms of the specimens. In the image formation process, the interactions of the transmitted and diffracted beams give rise to constructive or destructive interference whose patterns corresponds to lattice fringes along the particular zone axis.

Dislocations analysis from TEM images

For characterization of dislocations, we extract some important information from TEM images, which are mentioned as follows:

1. The direction and the magnitude of the Burgers vector (**b**), normal to the (hkl) diffracting planes
2. The dislocation line direction and hence the character of the dislocation (edge, screw or mixed)
3. The density of dislocations

To a first approximation called invisibility criteria, one used the diffracting vector **g** and the burgers vector **b**. When **g.b**=0, there will be no contrast from the dislocation in the image, and hence it will not be visible in the bright or dark field images[15]. In Table 2. 1, we have summarized the invisibility criterion for the dislocations which are commonly observed in group III nitride epitaxial layers.

For this work, a major part of TEM was performed by JEOL JEM-2010 operated at 200 kV using a thermoionic lanthanum hexaboride (LaB6) source.

Table 2. 1. Invisibility criterion of dislocations in Wurtzite systems

Burger vector, $\vec{b}$	$\vec{g} = 0001$	$\vec{g} = 11\bar{2}0$	$\vec{g} = 10\bar{1}0$
$[0001]$	Visible	Invisible	Invisible
$[000\bar{1}]$	Visible	Invisible	Invisible
$\frac{1}{3}[11\bar{2}0]$	Invisible	Visible	Visible
$\frac{1}{3}[\bar{2}110]$	Invisible	Visible	Visible
$\frac{1}{3}[1\bar{2}10]$	Invisible	Visible	Invisible
$\frac{1}{3}[\bar{2}113]$	Visible	Visible	Visible
$\frac{1}{3}[1\bar{2}13]$	Visible	Visible	Visible
$\frac{1}{3}[11\bar{2}3]$	Visible	Visible	Visible

2.2.1.2.3 Scanning Transmission Electron Microscopy (STEM)

STEM[16] is another mode in TEM, in which the electron probe is formed by focussing electron beam into a fine spot, which is scanned across the sample. Each pixel of STEM image is generated by the scattered intensity recorded corresponding to the same point. The STEM may use a High Angle Annular Dark Field (HAADF) detector, which allows chemically sensitive imaging.

The image intensity strongly depends on the specimen thickness (*t*) and composition. The integrated intensity (I) on the detector is a function of the mean atomic number Z of the atomic columns illuminated by the focused electron probe, which is represented[16] as equation 2.1.

$$I \sim Z^2 t \tag{2.1}$$

Figure 2. 6 shows a schematic diagram of a STEM-HAADF system. We have used STEM as a tool to investigate the chemical mapping of composition in InGaN QWs. The STEM images were further analyzed in order to extract the local indium composition inside InGaN QWs.

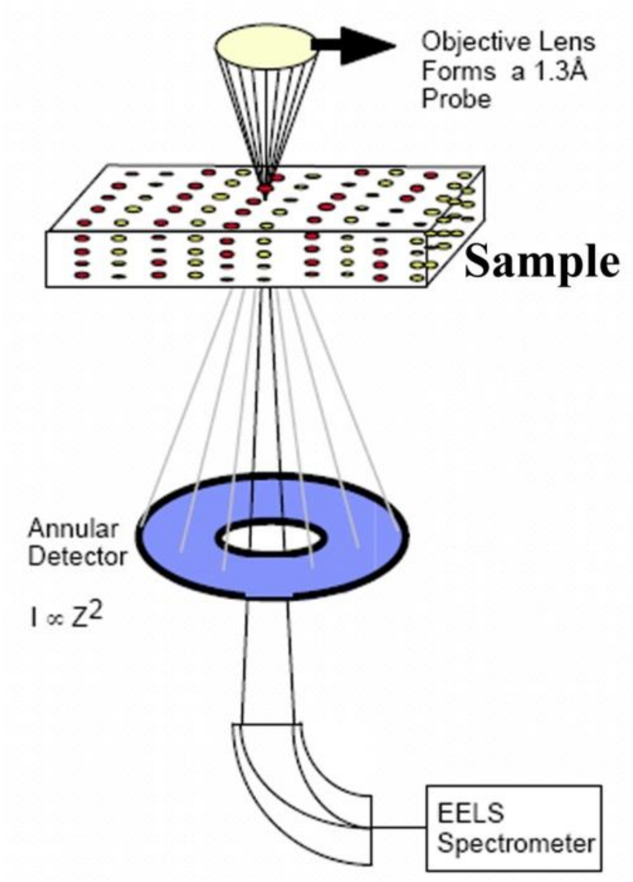

Figure 2. 6: Schematic of STEM-HAADF system configuration[17].

2.2.1.2.4 TEM sample preparation

A convenient way to study the epitaxial films and the interfaces is to investigate them in cross section. The samples presented in this thesis for TEM observation, were prepared by two different methods. The first was mechanical polishing and the other was tripod polishing. The steps involved in these two different sample preparation techniques are shown in the flow chart in Figure 2. 7. As can be seen few steps are common in both of these methods.

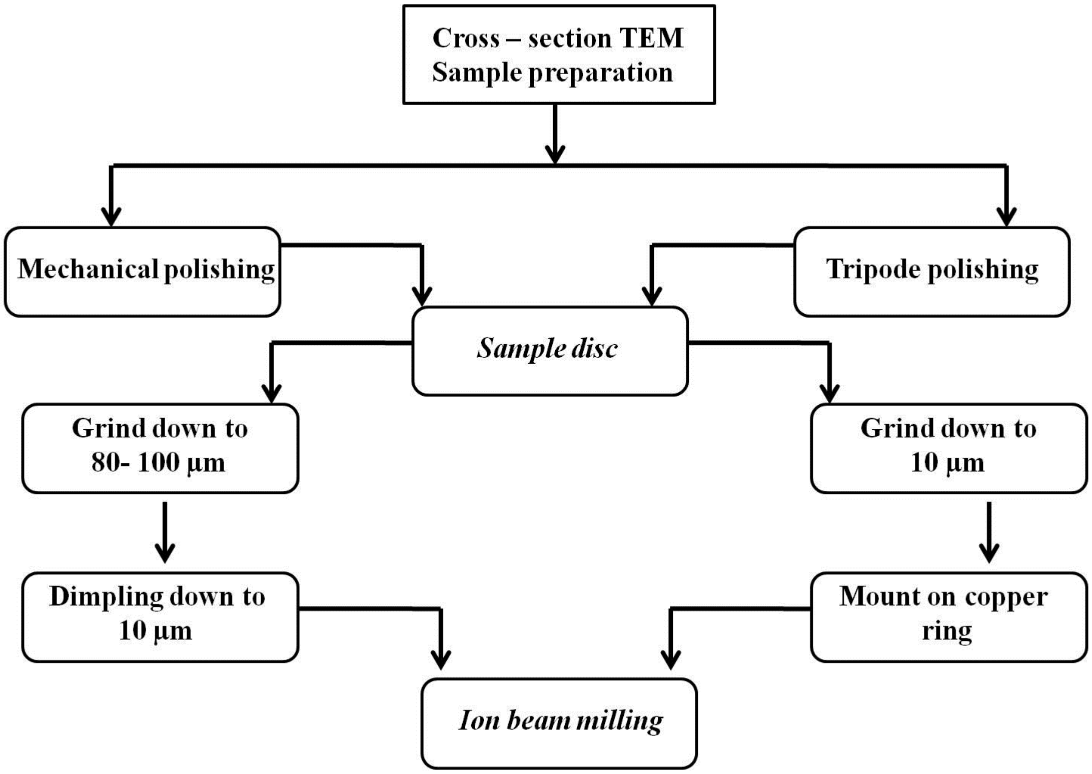

Figure 2. 7. A flow chart for TEM sample preparation.

Mechanical polishing

First, the specimens are sliced into small rectangular pieces (length ~ 10 mm, width~ 2.5 mm). The slices are bonded using a epoxy with the multilayers facing each other. Then the as prepared sandwich is introduced into a cylindrical tube as shown in Figure 2. 8 (a), (b) and (c) and then fixed inside with epoxy. Afterwards it is closed by a cap of cylindrical structure of 3 mm diameter shown in Figure 2. 8 (d). Then the whole structure is heated at about 100° C for about half an hour to cure the glue. This cylindrical structure is then cut into discs of about 800 µm thicknesses. Subsequently, different grain sizes silicon carbide papers are used to polish the 800 µm thick disc from both sides to reduce it down to 80-100 µm thickness. Then dimpling is performed to reduce further thickness of the disc in the central portion, in order to decrease the time for ion beam thinning. The final step is ion milling.

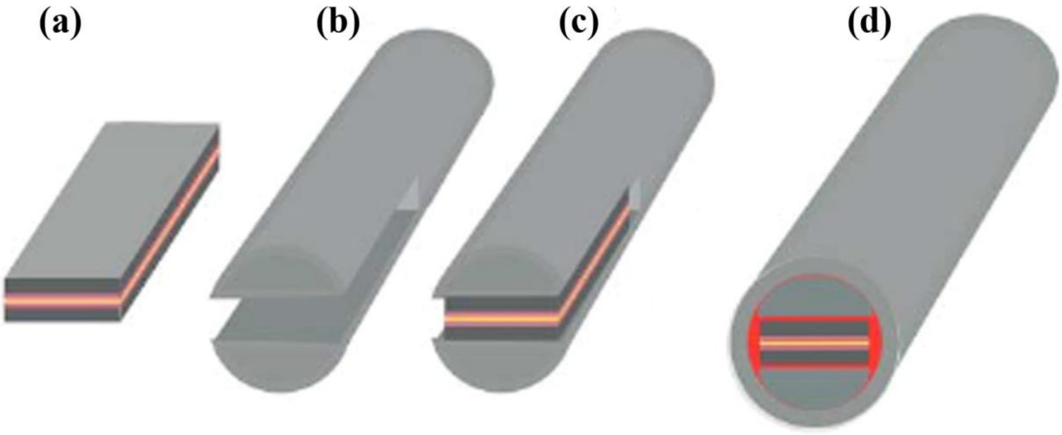

Figure 2. 8. Specimen preparation steps from (a) sandwich structure, (b) cylindrical tube, (c) sample embedded inside tube, (d) cylindrical tube closed with cap[18].

Tripod polishing

In this case, the sandwich structure is prepared with two slices of specimen (800 µm wide and 3 mm long) are bonded using (MBOND 610 b) epoxy. After allowing near about 2 hours for bonding, the sandwich is mounted on the tripod support (shown in Figure 2.9) and polished using different grain size (30 µm, 15 µm, 9 µm, 6 µm, 3 µm, 1 µm and 0.5 µm) diamond papers. This process is done for both sides of the sandwich and the thickness is reduced down to less than 10 µm. Next a copper ring is glued on the polished sample and the set is processed by ion milling down to electron transparency.

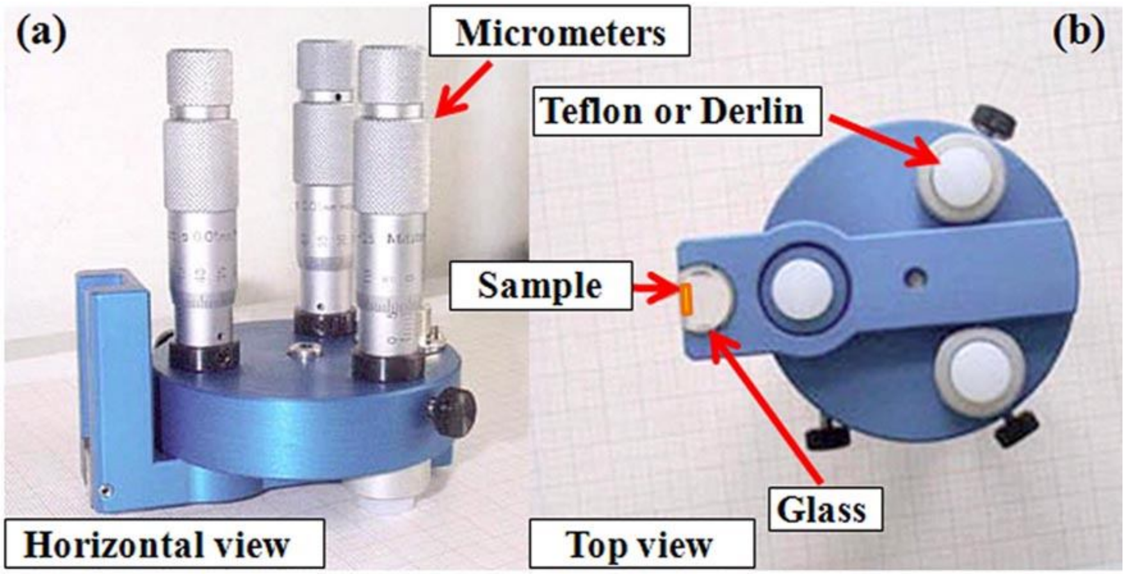

Figure 2.9. Tripode set[18].

Ion milling

The TEM samples are ion milled down to the formation of a small hole. In order to minimize the ion beam damage, the samples were maintained at the liquid nitrogen temperature during ion milling using the Gatan PIPS at 5 keV, with a final step at 0.7 keV for cleaning the amorphous layer formed while thinning. During the whole procedure, the beam angle was set at 5°. This low incidence leads to large electron transparent areas around the hole.

2.2.2 Optical characterization

If electron and hole pairs are excited and then recombined radiatively, the phenomenon is called luminescence. The electrons and holes can be created for example by an impinging electron beam in Cathodoluminescence (CL) or by light in Photoluminescence (PL) or as in case of a p-n junction by carrier injection in Electroluminescence (EL). Such experiments are used to probe the optical properties of semiconductors. In this work, the photoluminescence spectroscopy was used to characterize the films, and it is briefly described in the following sub section.

2.2.2. 1 Photoluminescence spectroscopy

It is a contactless, non-destructive method to probe the optical transitions in the semiconductors and other materials. Light is absorbed when directed onto a sample and it transfers excess energy into the material in a process called photo excitation. One way this excess energy can be dissipated by the sample is through the emission of light, or luminescence. In the case of photo-excitation, this luminescence is called photoluminescence.

The intensity and spectral content of this photoluminescence is a direct measure of optical properties. Photo-excitation causes the electrons to move within the material into allowed excited states. When these electrons return to their equilibrium states, the excess energy is released and may emit the light through a radiative process or a nonradiative process. The energy of the emitted light (photoluminescence) relates to the difference in energy levels between the two electron states involved in the transition between the excited state and the equilibrium state. The quantity of the emitted light is related to the relative contribution of the radiative process. In a semiconductor, the fundamental optical band edge transition and impurity or defect related transitions can be probed by

PL directly and precisely. The PL measurements were performed at room temperature as well as close to liquid Helium temperatures. For temperature dependent measurements a cold finger of a closed-loop gaseous helium cryopumps from APD Cryogenics was used to measure in temperature range between 5 K and 300 K. The experimental set up used for the PL measurement of InN and In-rich InGaN alloys is shown in Figure 2.10.

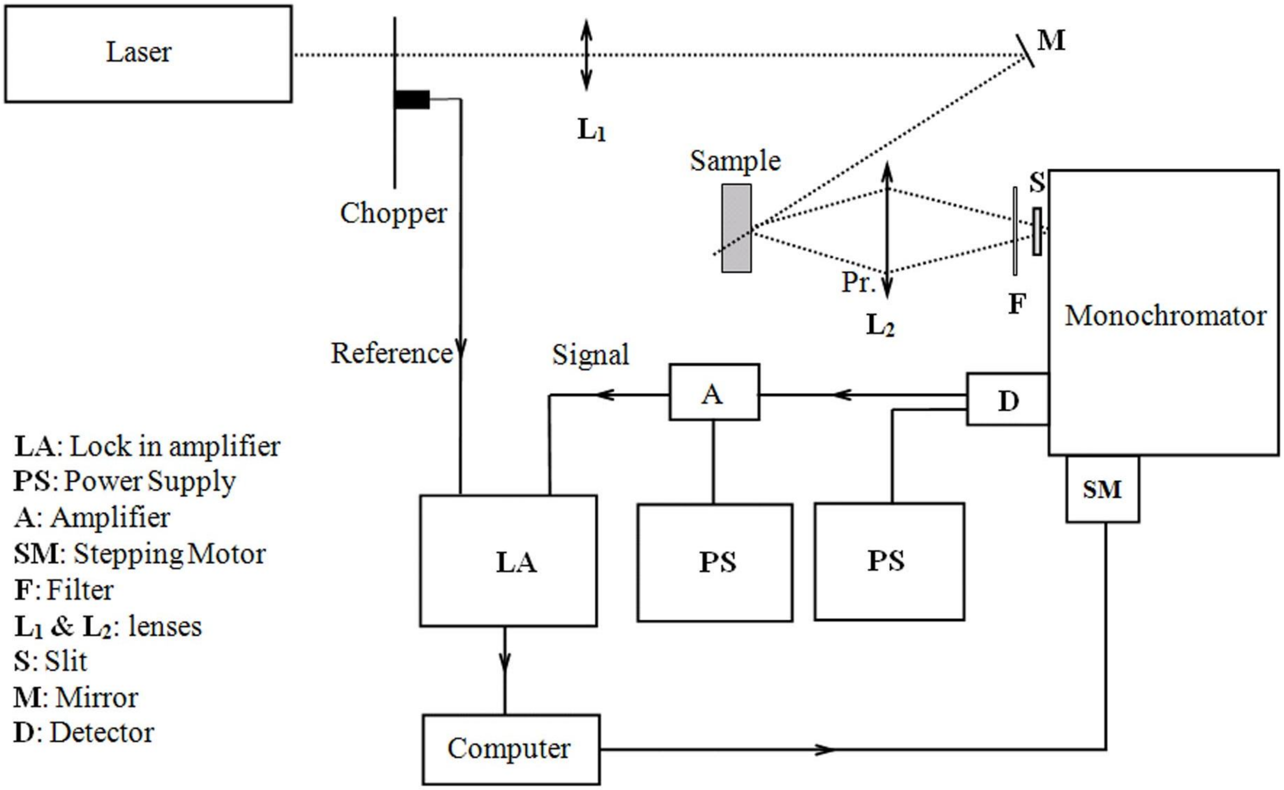

Figure 2.10. A schematic diagram for PL experimental set up.

A Lakeshore temperature controller was used to monitor and as well as to control the temperature of the cryostat. All the measurements took place in one run for an easier comparison of the samples. The wavelength measurement was done with a monochromator. The detection system is constituted by an InGaAs detector for wavelengths over 1 µm and a photomultiplier for wavelengths below 1 µm, which then produces an electrical current signal. An optical chopper and lock-in amplifier is used in order to improve the signal to noise ratio.

The analog electrical signal is transformed into a digital one, which is then transferred into the computer. The spectrometer is controlled by the computer which also collects the obtained data. In this work we used, different lasing sources. For instance, in case of InGaN layers, PL was studied by using a CW He–Cd laser whose excitation energy was 3.815 eV (325 nm). In case of InN samples, we employed argon laser whose excitation wavelength was 488 nm.

The raw photoluminescence spectra depend on the grating and detector response used in this system. In order to normalize the obtained PL spectra, the calibration was done with a tungsten lamp, whose spectral response behave like a blackbody source at the temperature of the filament, so all the as acquired PL spectra were corrected with this calibration.

2.2.3 Electrical characterization

The study of carrier kinetics is an essential aspect in characterizing the semiconductors towards the development of devices. There are several techniques available for studying the transport properties of these materials. In this work, we have performed the temperature dependence (80 K to 300 K) of electrical resistivity and low frequency noise, to investigate the transport properties of InN heterostuctures.

The low frequency noise versus temperature technique is a powerful diagnostic technique for determining Generation Recombination (GR) trapping parameters in semiconductors. The noise measurement set up was automated by GPIB interfacing using LABVIEW 7. In the following section, we present the probe stations, the experimental peripheral apparatus and the instrumentation for DC and low frequency noise characterizations.

2.2.3.1 Probe Stations

Probe stations allow us to achieve electrical contact with or access to a point in the active circuitry of the device. It employs a special piece of equipment known as a microprobing station, which is commonly referred to as a 'probe station’. In this work, two probe stations (Suss Microtech PM5 prober and Lakeshore TTP4 prober) were used accordingly with the working temperature conditions. These probe stations are equipped with built-in cameras. Both probers are used for non-destructive testing of devices. The photographs of these two probe stations are shown in Figure 2.11.

Electrical contact is made by positioning fine-tipped probe needles directly on the point of interest, or on an area to which the point of interest is connected.

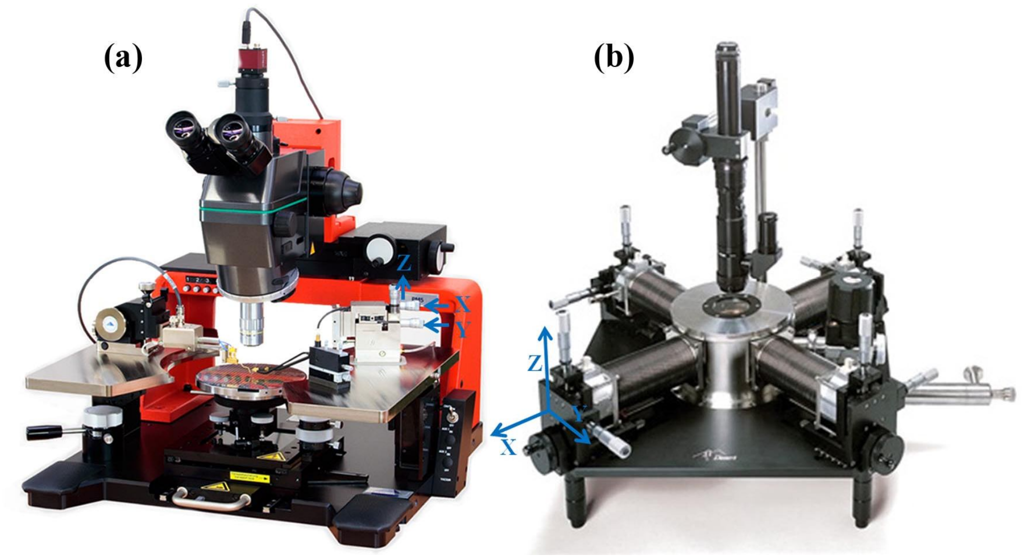

Figure 2.11. Probe stations: (*a*) Suss Microtech PM5 prober dedicated for room temperature measurements[19], (*b*) Lakeshore TTP4 prober for 80 K – 475 K[20].

Suss Microtech PM5 prober: The SUSS PM5 is simple and manual, probing solution for wafers and substrates up to 150 mm. Large application flexibility is ensured for DC and HF measurements, device and wafer characterization tests, failure analysis, submicron probing, MEMS tests. This prober is easy to use and allow convenient access to the probes and Device Under Test (DUT). The X and Y axes can be adjusted independently. Once it has reached the test position, the stage locks into place and provides additional fine adjustment in the Z direction. A pull-out stage permits quick loading and unloading of the DUT. This prober has been used for the measurements carried at room temperature.

Lakeshore TT prober (TTP4): It is a versatile cryogenic micromanipulated probe station used for the devices on full and partial wafers up to 2 inches in diameter. The sample chamber is very well shielded from external electrical effects and the capacitive coupling is extremely small. Temperatures can be varied from 4 K to 475 K, in our case we limit the temperature investigation between 80 K to 300 K. The probe station provides efficient temperature operation and control with a continuous refrigeration system using either liquid helium or liquid nitrogen. Two control heaters on the cold head, minimize temperature gradients across the sample and, along with the radiation shield heater, provide the probe station with fast thermal response. The TTP4 is user configured with up to four ultra stable micro-manipulated stages, each providing precise 3-axis control of the probe position to accurately land the probe tip on the device features. Proprietary probe tips in a variety of sizes and materials minimize thermal mass and optimize electrical contacts to the DUT. Probe tips are thermally linked to the cold head to minimize heat transfer to the DUT.

2.2.3.2 Peripheral apparatus

Semiconductor Parameter Analyzer (SPA): It is capable of measuring, analyzing and graphically displaying the DC characteristics of voltage and current sensitive devices easily. It is provided with 4 Source Monitor Units (SMUs), two programmable Voltage Source Units (VSUs) and two Voltage Monitor Units (VMUs) and a floppy drive which can be used to store the measured data. Precision DC I-V measurements are typically made with high-precision Source-Measure Units (SMUs) to generate current versus voltage curves. SMUs can source and measure both current and voltage. With the appropriate programming of SMUs and VMUs as current and voltage sources, one can perform a wide range of operations (like I vs V, V vs I, interfacing the SPA with probe stations for automation etc) on the DUT. The measured data stored in the internal disc can be transferred through the floppy disc. In our case we have employed Hewlett-Packard HP 4156B Precision Semiconductor Parameter Analyzer.

Dynamic Signal Analyzer: We have used HP 3562A Dynamic Signal Analyzer for extracting the low frequency noise data. It features a dual-channel fast Fourier transform-based network, spectrum and waveform analyzer which provides analysis capabilities in both the time and frequency domains. This unit operates from 0.1 Hz to 100 kHz frequency range. For transient analysis, the signals can be digitized and stored internally or exported via HP-IB interface to a computer (which is the case in our set up).

2.2.3.3 Current-Voltage (I - V) and resistance measurements

Electrical resistivity is one of the most important electrical parameter of semiconductors. The electrical resistivity and its variation with the temperature are often used to classify the materials into metals, semiconductors and insulators.

Bulk resistivity: The bulk resistivity (ρ) is an intrinsic electrical property related to carrier drift in materials such as metals and semiconductors. From a macroscopic point of view, the resistivity (ρ) can be viewed as the normalization of the bulk resistance (R_M) by its geometrical dimensions; the cross-sectional area (A = Wt, where W is width and t is thickness) through which the current flows, and the distance between the two ideal contacts L, as shown in Figure 2.12. The electrical resistivity is given by,

$$\rho = \frac{R_M\ A}{L} \tag{2.2}$$

In case of thin semiconductor layers, the sheet electrical resistivity ρ_s is often used instead of the bulk electrical resistivity ρ. The sheet electrical resistivity is the bulk electrical resistivity divided by the thickness of the sample. This normalized parameter is related to the resistance of a square of side L and is called the sheet resistance as $\rho_s = R_\square$, in Ω/square.

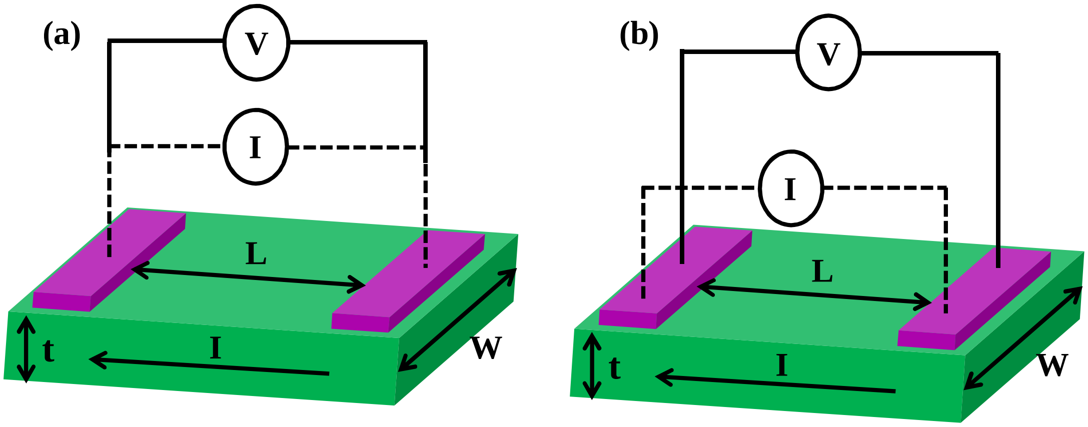

Figure 2.12. Bulk electrical resistance and its geometrical dimensions in: (a) two probe configuration, the voltmeter is connected to the probes where a source is connected, (b) four probe configuration where 2 other probes are used (This four probe configuration was used for measurements on TLM structures).

The simple way to determine bulk electrical resistivity is to measure the voltage drop along a uniform semiconductor bar through which a DC current (I) flows, as shown in the Figure 2.12. Thus, the measured electrical resistance and the knowledge of the geometrical dimension can lead to an estimation of the bulk electrical resistivity.

The total measured resistance (R_T) includes the contact resistance ($2R_c$), probes metal contact resistance ($2R_P$) and the resistance of the sample (R_M). The different contributions of contact, sheet and probe resistances are schematically shown in Figure 2.13.

$$R_T = R_M + 2R_c + 2R_P \tag{2.3}$$

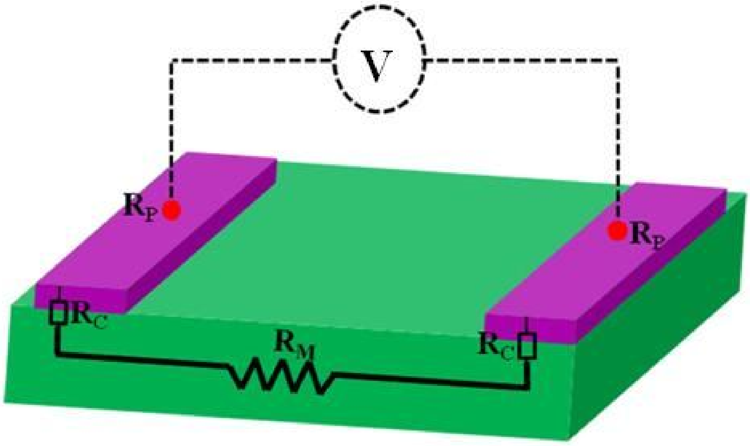

Figure 2.13. Schematic diagram for showing contact, probe and measured resistances.

In order to eliminate or at least to minimize the contact contribution to the measured resistance value, techniques based on a separated current injection and voltage drop measurements have been developed[21]. In this dissertation, for DC measurements, the two probes are used for current injection and two probes are used for measuring voltage drop, which will suppress the resistance $2\boldsymbol{R_P}$[21]. The contact resistance includes the resistance of the metal R_{metal}, interfacial metal-semiconductor resistance R_i and the resistance associated with the semiconductor just below the contact in the contact region, R_{sc}[21]. Thus contact resistance can be expressed as,

$$R_c = R_{metal} + R_i + R_{sc} \tag{2.4}$$

The contact resistance can be significant for small-geometry samples because R_c is strongly dependent on the metal–semiconductor structure. Hence the contact resistance measurements are of great importance. One of the main test structures to determine contact characteristics is Transmission Line Model (TLM) structure.

Transmission Line Model test structures: The TLM test patterns are commonly used for assessing the electrical quality of planar ohmic contacts[21]. The TLM test structures consist of depositing a metal grid pattern of unequal spacing between the contacts. From this linear TLM structures, the contact resistance and specific contact resistance can be determined through the linear relationship between the resistance and the spacing between the contacts. TLM patterns must be mesa-isolated to prevent fringing currents around the edges of the pattern. Metal pads of finite Length S and width W are deposited on the mesa at a linearly increasing pad spacing Li, such that L1<L2<… <L5. The schematic TLM structure is shown in Figure 2.14.

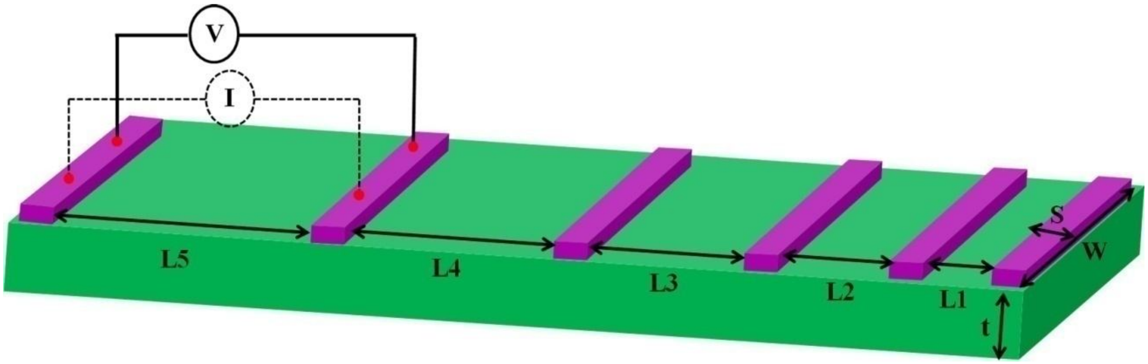

Figure 2.14. Schematic diagram of a semiconductor material with ohmic contact pads of the TLM structures.

Each resistor is changed by its distance *Li* between two adjacent contacts as shown in the Figure 2.14 and which can be expressed as

$$R_L = R_M + 2R_c \tag{2.5}$$

where R_c is resistance due to contact and R_M is the resistance of the semiconducting material. From Rs we can extract the sheet resistivity$\rho_{S,}$ as R_M is given by,

$$R_M = \frac{\rho_S \, L_i}{Wt} \tag{2.6}$$

A constant current is passed through two adjacent contact pads through two probes and two other probes are used to measure the voltage drop across the same pads to eliminate the resistance contribution due to the probes. This process is repeated and then by plotting the measured resistance across each adjacent contact pads as a function of the contact spacing *Li* and according to the equation 2.5, the sheet resistance R_S and the contact resistance *Rc*, can be deduced from the slope and from the intercept at *Li* = 0 respectively as shown in the Figure 2.15.

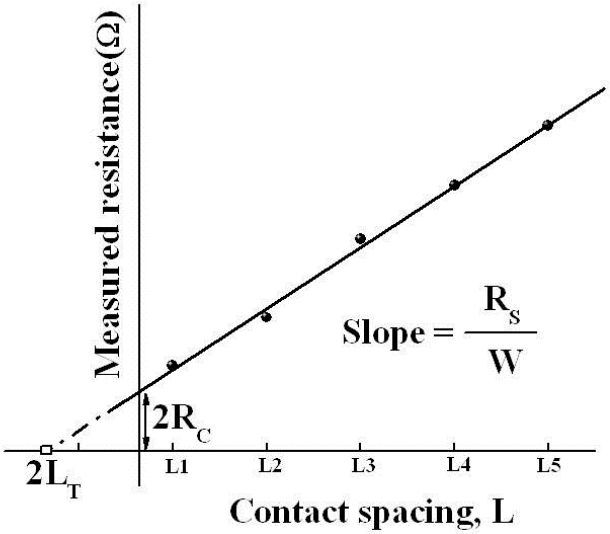

Figure 2.15. Measured resistance versus length between adjacent pads. This plot is a schematic for extracting contact and sheet resistances using TLM test structures.

L_T is called transfer length (which is shown in Figure 2.15), within which the current transfers from the metal to the semiconductor. The physical meaning of L_T is the characteristic distance inside the contact from its edge where 1/e of total current has been transferred from the semiconductor to the contact[22].

2.2.3.4 Instrumentation for DC measurements

The set-up for DC characterization is mainly constituted of a probe station and a Hewlett-Packard HP 4156B Precision Semiconductor Parameter Analyzer (SPA). The device under test is placed inside the probe station and is connected to the SPA via a set of BNC cables. It is important to note that probing should be done with sufficient optimum pressure on the contacts; not too much to avoid pierce through the layer and not too low to ensure consistent measured results. In the present work, the DC characteristics: I vs V measurements, contact and sheet resistances were investigated using SPA, configured with two SMUs which provide the current and two VMUs which measure the voltage across the sample. The I-V characteristics were deduced with this set up.

2.2.3.5 Instrumentation for low frequency noise

The noise measurements were performed in four probe configuration as shown in Figure 2.16. A DC source is connected to two current pads and a low noise voltage amplifier is AC connected to two voltage pads and is used to measure the voltage fluctuations. It is considered that the input impedence of the differential amplifier is very high, that the differential amplifier noise current can be neglected and that the voltage gain of the amplifier is constant over all the frequency range of interests. The fluctuations are small and a voltage gain of around 2000 is necessary so that the spectrum analyzer calculates the noise spectral density in optimum conditions. This set up has been developed at GREYC laboratory in Caen[23]. In order to remove all contact contributions, the output impedence of the DC current source has to be much higher than sample resistance. The noise spectral density can then be measured by a spectrum analyzer connected at the output of the amplifier[24]. These noise measurements were made in the frequency range of 10 Hz and 100 kHz and in some cases from 5 Hz to 50 kHz using either using the room temperature prober (Figure 2.11 (a)) or cryogenic prober (Figure 2.11 (b)) depending upon the need of measurements.

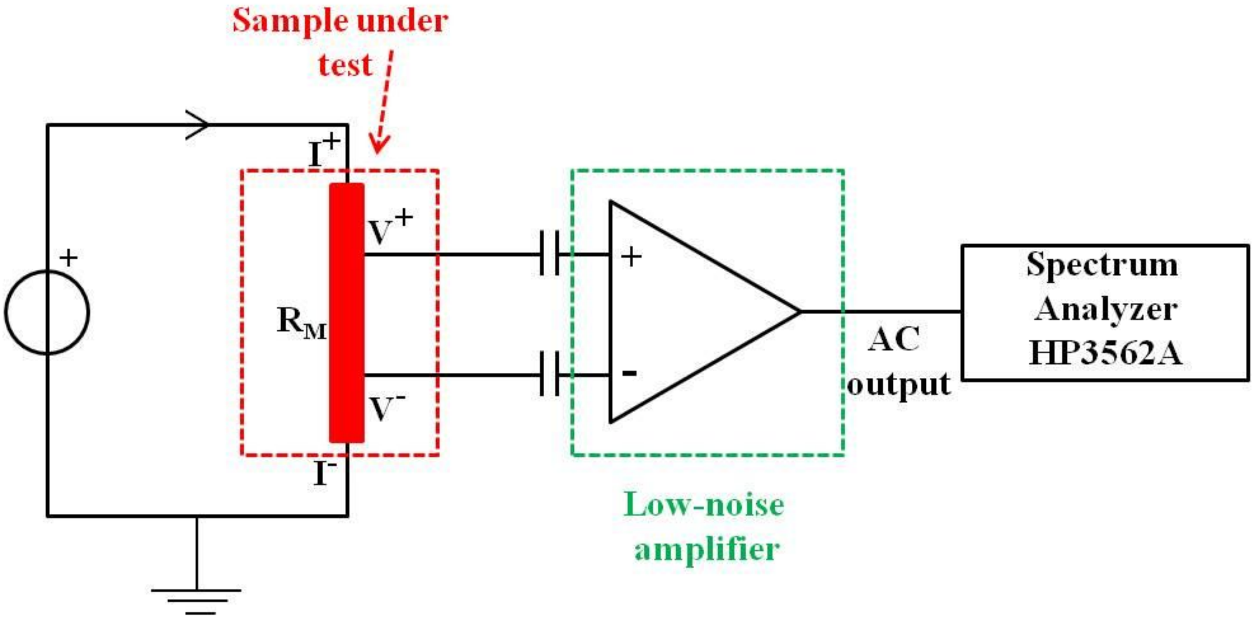

Figure 2.16. A schematic representation of the four-probe noise measurement setup[24].

To minimize the external noise, shielding boxes were used throughout. All the measurements were performed at low bias (in our case up to 8 mA) in order to carry out the measurements in a safe mode of the devices. For all the data reported in chapter 3, the 1/f noise level was obtained by dividing the output noise by the gain of the amplification chain (gain of the amplifier = 2095). A voltmeter was also connected between the voltage pads in order to measure the sample resistance and to confirm the results that obtained using HP4156B SPA set up. For all the resistance values and at each frequency much care has been taken to ensure that the set up noise level was negligible compared to the device noise, thus providing a guarantee that the observed noise came from the material and not from the electronics.

2.3 References

---

[1] A. Y. Cho and J. R. Arthur, “Molecular beam epitaxy”, Progress in solid state chemistry **10**, 157 (1975).

[2] T. D. Veal, C. F. McConville and W. J. Schaff, “Indium Nitride and Related Alloys”, CRC Press Taylor & Francis Group (2010).

[3] S. Nakamura, T. Mukai and M. Senoh, “Candela-class high brightness InGaN/AlGaN double heterostructure blue light emitting diodes”, Appl. Phys. Lett. **64**, 1687 (1994).

[4] G. Binning, C. F. Quate and Ch. Gerber, “Atomic Force Microscope”, Phys. Rev. Lett. **56**, 930 (1986).

[5] http://universe-review.ca/R11-13-microscopes.htm

[6] http://www.fei.com/uploadedFiles/Documents/Content/2006_06_AllYouWanted_pb.pdf

[7] D. B. Williams, C. B. Carter: “Transmission Electron Microscopy: A Textbook for Materials Science”, Ed. Springer (2009).

[8] Ludwig Reimer: Scanning Electron Microscopy: Physics of Image Formation and Microanalysis, Ed.Springer (1998).

[9] http://serc.carleton.edu/research_education/geochemsheets/techniques/SEM.html

[10] http://www2.warwick.ac.uk/fac/sci/physics/postgraduate/current/regs/mpags/ex5/techniques/structural/sem3/

[11] http://www.purdue.edu/rem/rs/graphics/sem2.gif

[12] http://134.74.50.69/em/files/SUPRA_Brochure.pdf

[13] http://www.mete.metu.edu.tr/pages/tem/TEMtext/raydiagram.gif

[14] http://www.mete.metu.edu.tr/pages/tem/TEMtext/TEMtext.html

[15] B. Fultz and J. M. Howe, “Transmission electron microscopy and diffractometry of material", Ed. Springer (2009).

[16] P. Hartel, H. Rose and C. Dinges, “Z-contrast stem for material science”, Ultramicroscopy **30**, 58 (1989).

---

[17] S. J. Pennycook, “Structure Determination Through Z-Contrast Microscopy”, Adv. in imaging and electron physics **123**, 173 (2002).

[18] http://cime.epfl.ch/files/content/sites/cime2/files/shared/Files/Teaching/MSE_603_2011_Autumn/Chapter%208%20-%20Sample%20preparation.pdf

[19] http://www.cmicro.com/products/probe-systems/applications/150mm-wafer/pm5/pm5-150mm-manual-probe-system.

[20] http://www.lakeshore.com/ObsoleteAndResearchDocs/TTP4.pdf.

[21] D.K. Schroder, “Semiconductor material and device characterization”, John Wiley & sons, INC. 2nd edition, (1998).

[22] M. Lijadi, F. Pardo, N. Bardou and J.-L. Pelouard, “Floating contact transmission line modelling: An improved method for ohmic contact resistance measurement”, Solid-State Electronics **49**, 1655 (2005).

[23] J. M. Routoure, D. Fadil, S. Flament, and L. Méchin, “A low-noise high output impedance DC current source”, AIP Conference Proceedings **922**, 419 (2007).

[24] J. M. Routoure, D. Fadil, C. Barone, S. Flament and L. Méchin, “Four probe low noise measurement set-upusing a high output impedence low noise DC current source”, (article under preparation).

Chapter 3

Plasma Assisted Molecular Beam Epitaxial InN layers electrical conduction

In this chapter, low frequency noise measurements were used as a tool to qualify the quality of the material and to access the bulk conductivity in InN layers which is crucial to achieve for device applications.

3.1 Introduction

Indium Nitride (InN) is known from six decades, but until recently there had been a lack of research attention mainly, because of the difficulty in growing high quality single crystalline InN. In 2002, the reevaluation of band gap from 1.89 eV[1] to 0.7 eV[2], has rekindled the research in nitride community and afterwards InN came up with its many interesting properties like the smallest electron effective mass[3], the largest mobility[4] and the highest peak and saturation electron drift velocities among the known semiconductors3. Therefore, InN has emerged as a promising candidate for high speed electronic and optoelectronic applications up to terahertz frequencies[5]. However, there are still many challenges for device fabrication which are related to material's properties. One of them is the presence of high residual n – type carrier concentration above $2x10^{17}$ cm^{-3}, irrespective of growth technique used[6]. The lowest room temperature n- type residual carrier concentration and mobility achieved were about $3.5x10^{17}$ cm^{-3} and 2050 $cm^2V^{-1}s^{-1}$ by (MBE)[7] and $4x10^{17}$ cm^{-3} and 1180 $cm^2V^{-1}s^{-1}$ by (MOVPE)[8]. In other words, the material properties of InN changes dramatically with the growth techniques employed. It is commonly admitted that MBE grown samples exhibit better quality in terms of structural and superior electrical properties than MOVPE or other techniques. Though MBE left a benchmark in growing first single crystalline InN films, it is still a challenge to obtain higher quality layers. The major two bottlenecks to obtaining high quality layers are the low dissociation temperature of InN and the extremely high equilibrium vapor pressure of nitrogen. The lack of native substrates is also an additional difficulty for InN epitaxy[9].

This chapter is related with the electrical transport properties of InN layers grown by Plasma Assisted Molecular Beam Epitaxy (PAMBE). The following section will give a brief review about the growth of InN layers with PAMBE and its transport properties as found in the literature.

3.1.1 PAMBE growth regimes of InN

InN layers are known to grow at reduced processing temperatures due to its low dissociation temperature. Therefore, the temperature-processing window for the growth of InN is very narrow, about 400-480° C for In polar InN[10] and 480-600ºC for N polar InN[11]. Most of the InN films are grown on GaN or AlN buffer layers on sapphire substrates. InN has two growth regimes as In rich and N rich regions. Polarity is an important issue, which affects the surface and bulk properties of InN layers. The growth temperature is also greatly influenced by the film polarity. The growth details of In polar and N polar InN are given in the following paragraphs.

Gallinat *et al.*[9] proposed a growth diagram for In polar and N polar InN material system which is shown in the Figure 3. 1. The figure 3.1 (a) represents the growth diagram of In polar InN.

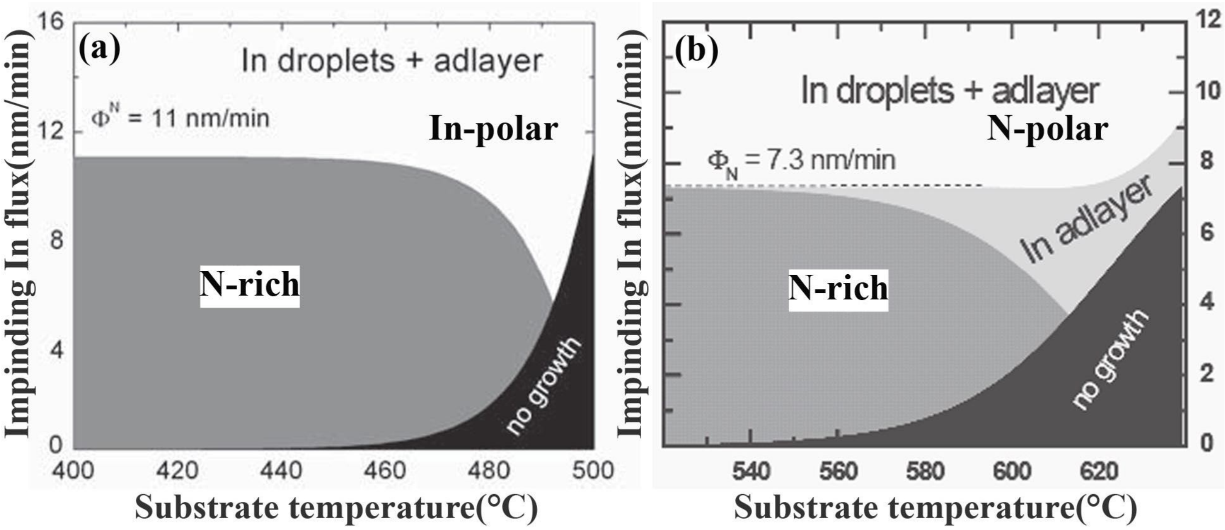

Figure 3. 1. PAMBE growth diagram of : In polar InN[10] and (b) N polar InN[11], where Φ_N is nitrogen flux .

As it can be seen, the decomposition rate of InN is significant for substrate temperature above 480° C. There are two regimes: (i) In droplet region under In rich growth conditions and slightly N rich conditions and (ii) dry region under more N rich conditions. The boundary between the In-rich and N-rich regimes is assumed to occur, when the active nitrogen and indium fluxes are equal. The transition from the In-rich to intermediate regime is possible only when there is significant In flux (Φ_{In}) desorbing from the surface, such that an equilibrium metal accumulation can be achieved. This curve has been estimated from the desorption of indium from indium metal as described by the Hertz-Knudsen equation[12]. The N polar InN has three different growth regimes as shown in Figure 3. 1 (b). It consists of (i) In droplet on top of adlayer structure under In rich growth conditions, (ii) In adlayer structure under slightly In-rich and also slightly N-rich growth conditions at high temperatures and (iii) a dry no adlayer terminated surface under more N - rich growth conditions. In short, the best growth temperature of N-polar InN is higher than that of In-polar InN. The growth temperatures beyond 500° C are not possible for In face InN, while growth temperatures as high as 640° C can be achieved for N face InN. The smoothest surface morphologies for both InN polarities were obtained in films grown with excess In, in which a metallic In-adlayer was present (2.5 ML for the In-face and ~1 ML for the N-face; where ML is monolayer) during growth9. To attain atomically flat surface, four important factors are necessary:

(1) In-polarity is preferred because it exhibits a smoother morphology than N-polar films[13]. In fact, the step height is 2 or 4ML for the smoothest surface of the N-polar InN and it is difficult to obtain an atomically flat surface with a one-monolayer step height[9,14, 15].

(2) A slightly In-rich growth condition has to be chosen9.

(3) A GaN template with low dislocation density has to be used9.

(4) A high growth temperature should be used, as close as possible to the decomposition limit9.

3.1.2 Transport properties of indium nitride

Figure 3. 2 shows the dependence of electron concentration9 on growth temperatures for three different Φ_{In} corresponding to In droplet, stoichiometric and N rich growth for In face InN. As shown in Figure 3. 2 (a) the electron concentrations are lower for the films grown in In droplet region and the mobilities of these In rich InN layers are the highest as can be seen in Figure 3. 2 (b). The

minimum electron concentrations and maximum electron mobilities were measured for In-face InN films grown at the highest possible temperatures (prior to thermal decomposition) in the In-droplet growth regime.

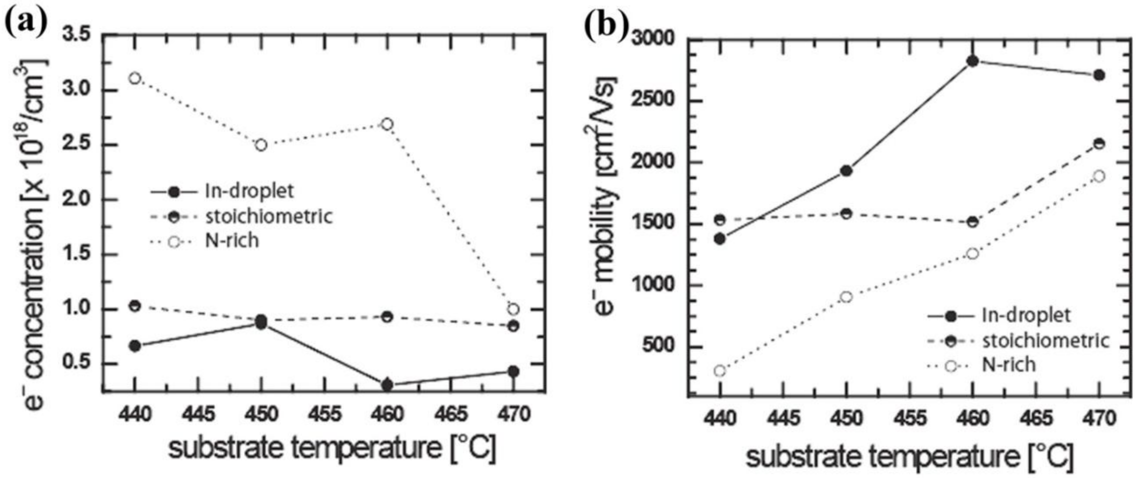

Figure 3. 2. (a) Dependence of electron concentration and (b) electron mobility on substrate temperature for InN samples grown at three different In flux (Φ_{In}) and constant N flux (Φ_N)[9].

Figure 3. 3 shows reported values of InN electron density and mobility as a function of the layer thickness[16]. The electron mobility increases with layer thickness, while the free electron concentration decreases. Closed symbols are grown on a GaN buffer, open are on AlN. Circles

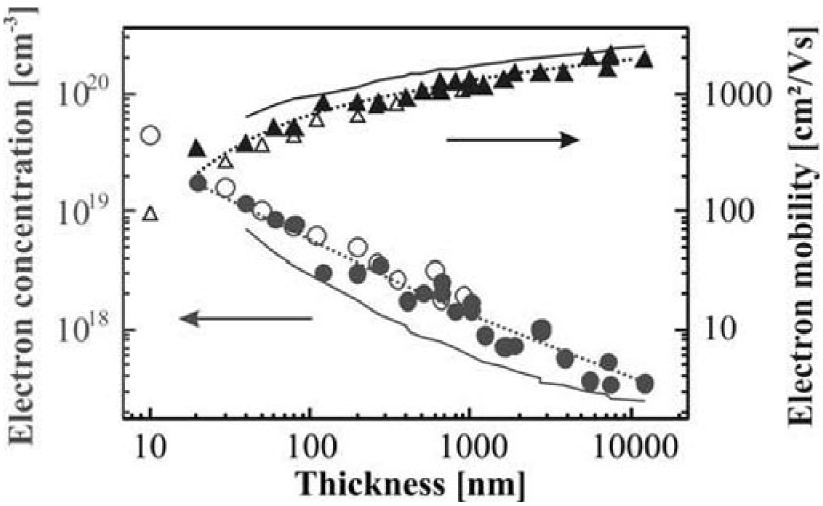

Figure 3. 3. Electron density and mobility as a function of InN thickness[16,] 9.

are carrier density, triangles are mobility. Dotted lines are fits to GaN characteristics to provide a smoothed function for differentiation. Solid lines are extraction of differential density and mobility[16]. Lu *et al.*[17] observed a gradient of carrier concentration ranging from 10^{20} to 10^{18} cm^{-3} within 6 nm in depth at the InN surface which shows a strong accumulation of charge carriers at the surface.

Surface electron accumulation is observed as an intrinsic property of the InN epitaxial layers. Recently, this surface electron accumulation phenomenon on InN layers has attracted much attention. Indeed, despite the novel properties of InN, there is still a hindrance for device applications because of the presence of this intrinsic charge accumulation at InN clean surfaces. However the presence of an electron accumulation layer is of great interest for sensor applications[18]. The main cause of electron accumulation on the InN surface and how it is related to the surface atomic configuration are still not clear. A number of reports have shown that this electron accumulation layer is strongly localized within several nanometers of the film surface[17,19.] These surface effects are pronounced in the layers of InN less than 300 nm thickness. The magnitude of the electron accumulation layer is highly accounted for polarity effects, and hence is likely due to a high density of donors near or at the surface. Swartz *et* al[20] reported that there were two distinct conducting layers. A high mobility layer with a mobility of >1000 $cm^2V^{-1}s^{-1}$ was assigned to bulk conduction, while a low mobility layer of ~200 $cm^2V^{-1}s^{-1}$ was assigned to surface and/or interface conduction. An additional factor which can influence the electron accumulation within films is the surface morphology[21]. There are many reports on surface charge accumulation in InN layers, including the measurements of sheet carrier density as a function of InN film thickness and Capacitance-Voltage (C-V) profiling[18]. Photoemission results from Ti deposited on Ar-sputtered InN indicated that the Fermi level is located high in the conduction band[22]. The existence of an electron accumulation layer on clean InN (0001) surfaces has been confirmed by High Resolution Electron Energy Loss Spectroscopy (HREELS) and X-ray Photoemission Spectroscopy[23]. Angle-resolved Photoemission Spectroscopy was used to observe quantized energy levels in the surface electron accumulation layer on InN films grown by Radio Frequency Plasma - Assisted Molecular Beam Epitaxy[24]. Bhatta *et al.*[25] claimed the presence of charge accumulation on InN layers grown by High Pressure Chemical Vapour Deposition by using HREELS and suggested that the excess surface electron accumulation presence in InN was not due to excess indium or In-In bonds. This is consistent with the pinning of the surface Fermi level in the conduction band[26]. As was shown during the last few years, the surface Fermi energy in InN is pinned at 0.9 eV above the bottom of the conduction band by donor like surface defects, which creates a *n*-type accumulation layer at the surface that seems unaffected by chemical or physical treatments[19]. Obviously, the conductivity of this surface layer has to be considered in any investigation of the electrical properties of InN samples. The electrolyte based chemical C-V measurements have been used to point out a net concentration of ionized acceptors below the *n*-type surface and demonstrated the possibility of InN p-type doping using Mg acceptors[27].

Despite the large amount of studies on electron accumulation at InN surfaces, we have been the first to use noise measurements to investigate this issue. With these measurements, one can overcome the problem of other conventional techniques like C-V measurements, which needs schottky contacts. We have been able to distinguish between surface conduction and bulk conduction in InN layers by using low frequency noise[28].

3.2 Objectives of this research

In this work, we have carried out Low Frequency Noise (LFN) measurements to qualify the devices in terms of material quality and then to investigate the electrical conduction mechanisms, and finally to relate them to the bulk and surface transport properties.

3.3 Description of samples

3.3.1 Samples schematic

This chapter contains two different sets of InN heterostructures grown at ISOM, Madrid. All the samples were grown on c-plane sapphire substrates by (PA-MBE). The schematic of the InN heterostructures used in this work is shown in Figure 3. 4. The wafers consisted of the following multilayer structure: A commercial LUMILOG semi-insulating Ga polar GaN layer (5µm) grown by MOVPE on sapphire substrates served as a template. The PA-MBE then started with the growth of a 90 nm thick GaN layer and the InN layers were grown on top with a nominal thickness of ~250 nm to 400 nm. All of the samples are In polar InN layers and were grown in slightly N-rich (A series and B3) or slightly In-rich (B1 and B2) conditions as mentioned in Table 3. 1. The structural investigations of as grown InN epilayers show that they are of substantially good crystalline quality[21].

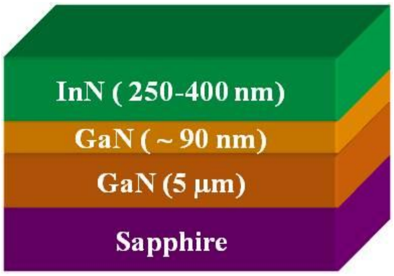

Figure 3. 4 Schematic heterostructure of InN sample

Table 3. 1 Specification of as grown InN epilayers from ISOM

Series of samples	**Wafer**	**Sample No.**	**Specimen name**	**Growth temperature (° C)**	**InN nominal thickness (nm)**	**Growth regime**	**Roughness of as grown wafer by AFM (nm)**
A-series	R465	1-5	A1, A2, A3, A4, A5,	400	400	N - rich	10.9
B-series	R489	6	B1	325	255	In - rich	1.44
	R338	7	B2	440	400		0.7-2.03
	R441	8	B3	440	345	N - rich	11

As it can be seen from Table 3. 1, there are two different series of samples named as A and B series, respectively, the description and the motivation behind the studies related to both series are mentioned below.

A series of samples were used to optimize the device fabrication steps on InN layers. This set consists of 5 samples cut from a single layer (R465), the description of as grown layer is given in Table 3.1. The AFM observations confirmed that this sample R465 has been grown in slightly N rich conditions (roughness: 10.9 nm, Table 3. 1). As stated earlier these samples were grown and fabricated at ISOM. So after following the sample specifications, we counter checked that this wafer is grown in slightly N rich growth condition, which was confirmed after surface morphology studies.

B series and along with the optimized A series samples, were used to investigate the electrical transport properties versus growth conditions. (In and N rich InN, growth temperatures and layers thickness).

3.3.2 Samples geometries and fabrication process

A- Series

Geometry: Each sample of this series consists of four devices as shown in Figure 3.5 (a), which is an optical microscopy picture. Every device has a specific mask (shown in Figure 3.5 b) which is repeated all over the wafer as shown in Figure 3.5 (a). Hence, each device has three different geometries for different purposes like (I) Hall measurements, (II) TLM structures to study contact and sheet resistances and (III) noise properties studies. In this work, we have utilized the geometries II and III respectively. The lengths and widths of these geometries are schematically represented in Figure 3.5 (b).

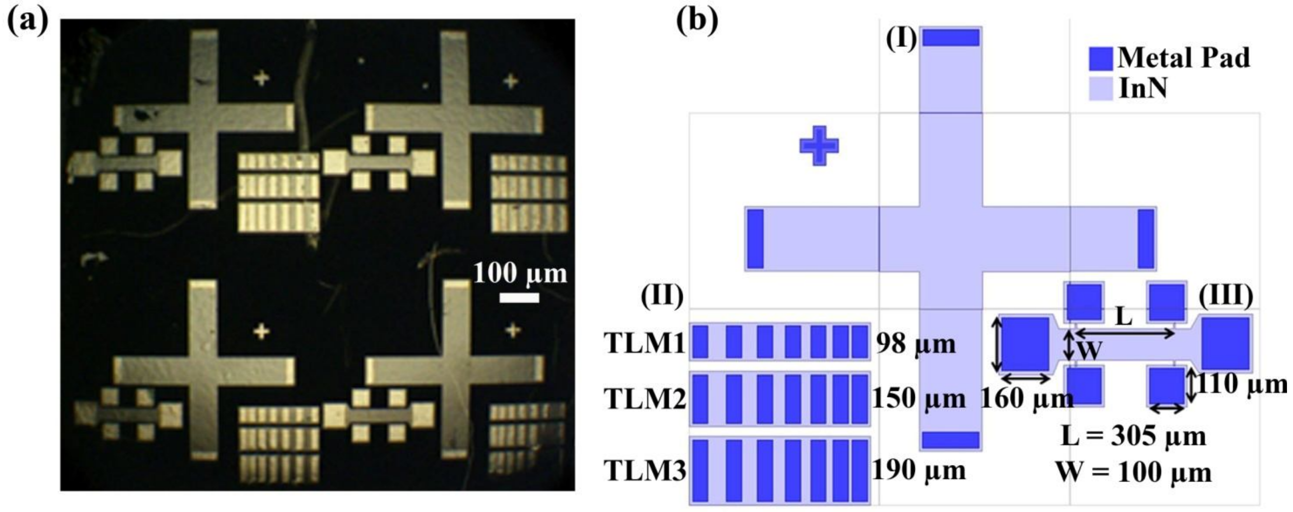

Figure 3.5. Geometry of A series samples. (a) An optical image of one of the samples composed of 4 devices, (b) Mask geometry of one device.

On each device, we have three TLM structures of different sizes of contact pads as 98 x 50 µm^2, 150 x 50 µm^2 and 190 x 50 µm^2, and the distances between the metallic pads were 56µm, 48 µm, 38 µm, 30 µm, 19 µm and 10 µm respectively. As shown in Figure 3.5 (b), the geometry III has 6 contact pads in which we have used four pads: 2 pads across L , for current(160 x 160 µm^2) and the other two along either of the sides of the geometry as voltage pads(100 x 100 µm^2). The noise measurements were done at all the temperatures across this geometry III.

Fabrication process: In these series, two different fabrication steps were followed: (1) electrical isolation of every device through a mesa; (2) deposition of metallic contacts(Ti/Al/Ni/Au) and photolithography. In the patterned devices, one can notice in Figure 3.5 (b), the light blue colour corresponds to InN, while around it is white or transparent, which means absence of InN, and hence GaN. Usually, Mesa etching induces damages to the material; which can be reduced by thermal annealing. In order to see the impact of thermal annealing before and after electrical isolation, we followed the fabrication steps as shown in the flow chart of Figure 3. 6.

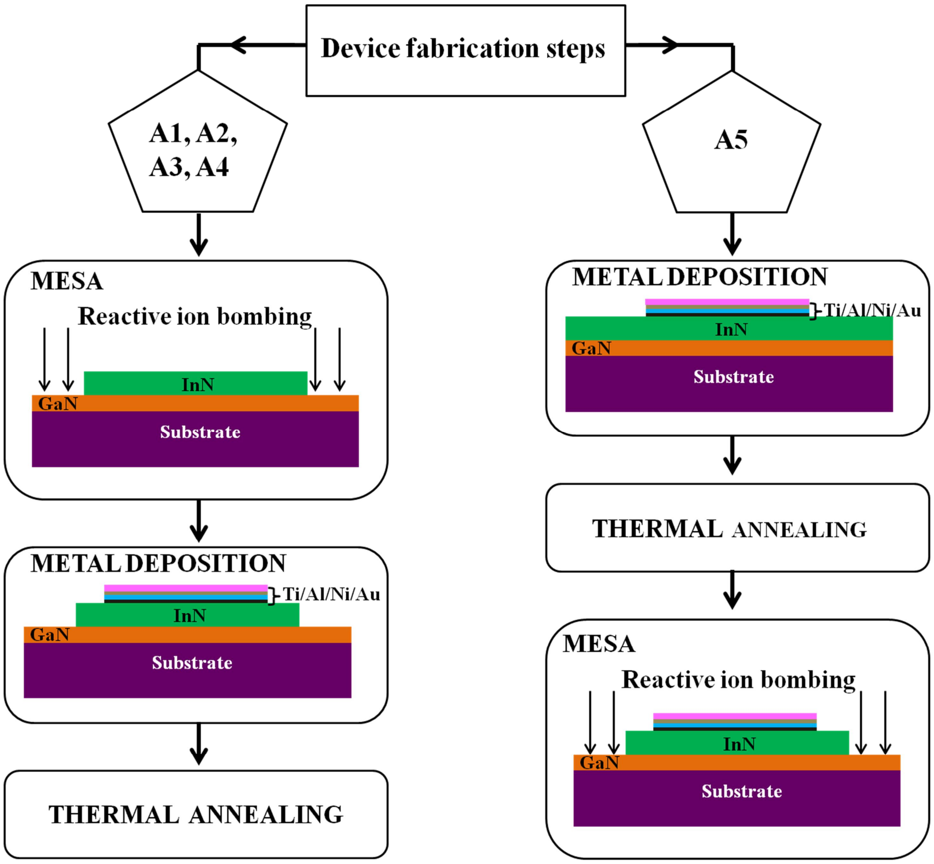

Figure 3. 6: A flowchart for fabrication steps: A cross section view of fabrication steps. for samples A1, A2, A3, A4 and A5.

Samples A1, A2, A3 and A4 are first went through the electrical isolation followed by metallization and then thermal annealing was done at 400°C in a nitrogen atmosphere. For sample A5, first metal contacts were deposited and then thermal annealed followed by electrical isolation. For samples A1, A2, A3, A4 and A5, the annealing time was varied as 0 min, 5 min, 10 min, 20 min and 10 min respectively.

B- series

Geometry: Each sample of this series consists of many devices. Every device has a specific mask which is repeated all over the wafer as shown in Figure 3. 7 (a). As shown in the Figure 3. 7 (a) , each device was made of three TLM structures, constituted of a series of contact pads (area 94 x 48 µm^2) with spacings of 210 µm, 170 µm, 114 µm, 57 µm and 38 µm respectively mentioned for TLM1. The contact and sheet resistance were extracted from three TLM structures which are sown in Figure 3. **7** (b). The noise measurements were performed on TLM1 across contact spacing of 210 µm.

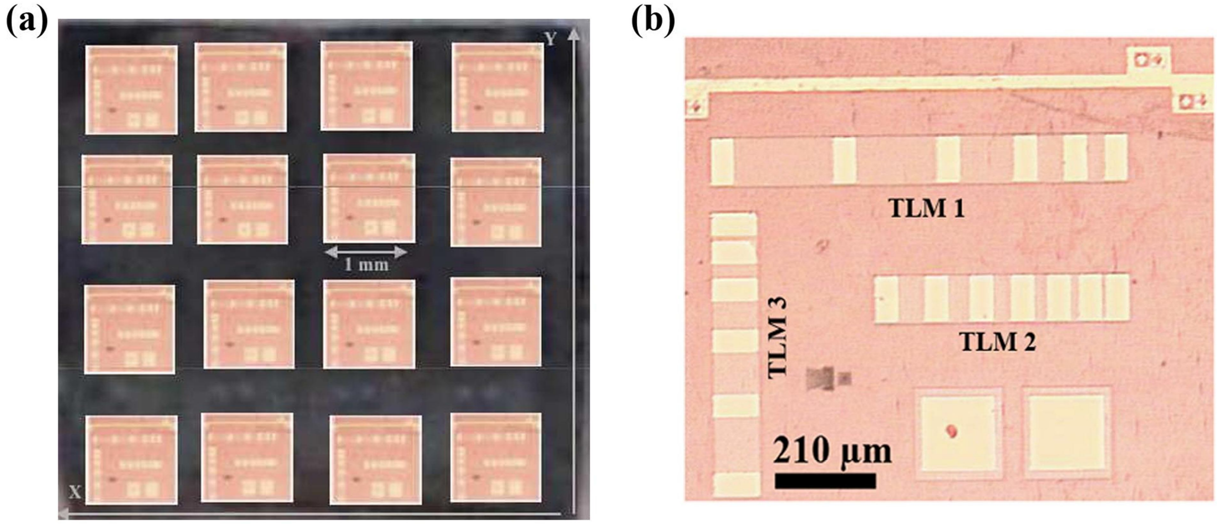

Figure 3. 7. Geometry of B series. (a) A photograph of one of the samples, (b) A view of the elemental device.

Fabrication process: All 3 samples of this series were fabricated using the same process. A stack of metals Ti/Al/Ni/Au (20 nm/40 nm/20 nm/80 nm) was deposited using e-beam evaporation. Films were photolithographically patterned and processed by Reactive Ion Etching to form Transmission Line Method (TLM) structures and were annealed at 400°C during 15 min in a N_2 flow. The fabrication steps followed were same as A1, A2, A3 and A4 (Figure 3. 6).

3.4 Effect of processing modulation on electrical performances of N rich InN layers

The device fabrication processes can also have an effect on the material properties, as in the case of the passivation induced stress or the change of strain after annealing. The objective for this section of work is to study the effect of device technological processing steps and the role of annealing on the surface roughness, photoluminescence and transport properties of the InN layers. To this end, we have chosen N rich InN layer, because it gives more accurate transport properties due to the higher surface conductivity contribution to the total electrical conduction as stated by Fehlberg *et al.*[29] . For a careful investigation of this topic, we used same InN wafer which was cut into 5 pieces and then subjected to different technological steps and annealing.

3.4.1 Characterization

3.4.1.1 The surface morphology by AFM and SEM

Figure 3. 8, shows the 10 x 10 µm^2, AFM images of patterned InN resistors which were grown in slightly N rich condition. The left hand side image corresponds to the non-annealed InN layer(A1) and the right hand side picture represents the sample annealed for 20 mins(A4). As it can be seen the morphology of the two specimens exhibit platelets propagating in a zigzag manner and surrounded by deep trenches which leads to the observed large surface roughness (around 14 nm). As the annealing time increased, the roughness of InN resistors are proportionally increasing upto 10 mins and then decreasing, which is confirmed from the Figure 3. 9 (a): the solid spheres represent the roughness of metal pads, while the open squares represent that of InN layer. The roughness of the metal pads are also increasing with the increase of annealing time, indeed, the surface roughness of InN layer and the metal pads are almost identical for A1, A3 and A5, whereas for A2 and A4 the metal pads have much higher roughness than the InN layers, have metal pad follows the surface morphology of InN, which is reflected from the SEM image (Figure 3. 9 (b)) taken across the metal pad and the InN layer where one can see their different morphologies. For the same annealing time, the samples A3 and A5 exhibited close surface roughness irrespective of technological steps. The other properties may throw light on these observations to come up with some conclusions or the reasons behind these behaviors.

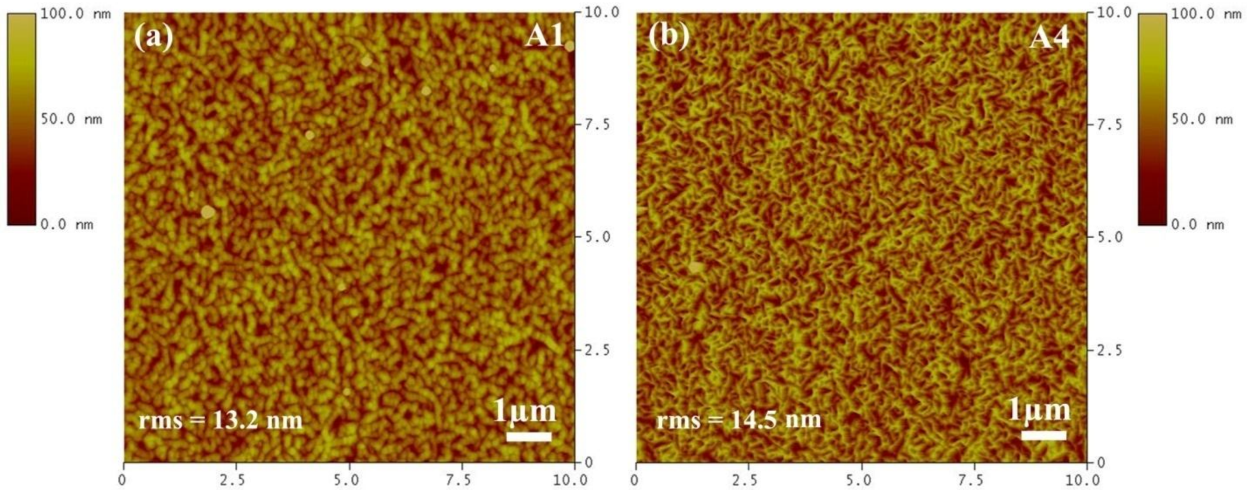

Figure 3. 8. AFM image of samples InN/GaN/sapphire (a) A1 (un annealed) (b) A4 (t = 20 mins). The RMS roughness is (a)13.2 nm for A1 and (b)14.5 nm for A4 respectively.

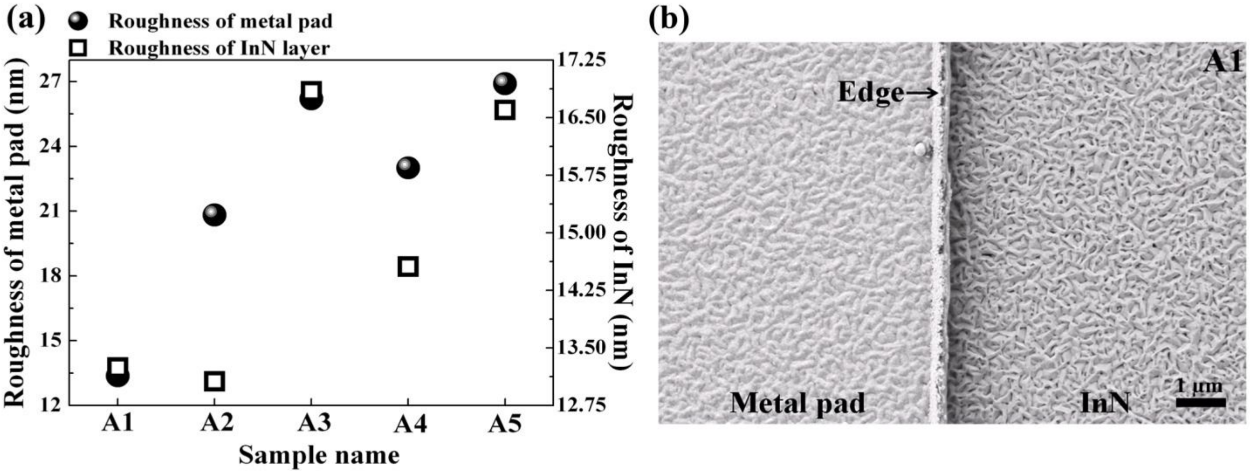

Figure 3. 9 (a) Roughness of InN resistors and the metal pads, (b) SEM image of sample A1.

3.4.1.2 Photoluminescence characteristics

We selected A1, A3 and A5 samples to study the influence of the annealing process of prior and post metallization using photoluminescence. Specifically A3 was chosen among A2, A3 and A4, because A3 has the same annealing time as of A5. Photoluminescence measurements were conducted at 12 K. The PL signals were observed in the vicinity of 0.72 eV which is close to the optical absorption edge. It demonstrates that, these InN films were of good quality. The small band gap corresponds to low level of residual carrier concentration, which gives the indication, that electrical isolation before metallization would be the better option in the fabrication steps and thermal annealing at the end of fabrication steps is more appreciated.

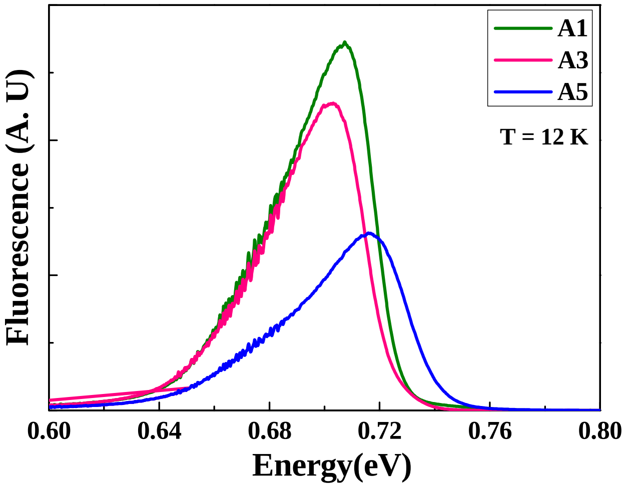

Figure 3. 10. PL spectra on patterned InN layers (Sample A1 , A3 and A5).

The PL intensity is observed as inversely proportional to the surface roughness. This may be accounted for the high roughness of the surface which diffuses the light emitted, as a result reduces the intensity of PL emission. This reveals that the fabrication steps followed and the time of thermal annealing have direct influence on the optical properties. From the Figure 3. 10, it is clear that electrically isolation after metallization will degrade the optical quality and also thermal annealing lowers the PL intensity. In order to better understand the layers properties further, electrical measurements were done.

3.4.1.3 Electrical properties studies at room temperature

Estimation of contact and sheet resistances using TLM patterns

The Current-Voltage (I-V) characteristics of all the InN films in these A series samples are accessed with SPA. InN TLM patterns for different geometries as shown in Figure 3.5 (b), were measured; we had an ohmic behaviour for both the InN material and the metallic contacts as reflected from the I-V plots shown in Figure 3. 11 (a). The contact and InN sheet resistance values were extracted from the measured resistance as a function of spacings between metallic pads as described in Chapter 2, which are shown in Figure 3. 11 (b). For different TLM geometries, the measured sheet resistance is similar as that shown in Figure 3. 11 (c), which confirms the homogeneity of the InN wafer. The contact and sheet resistances for all of these layers are shown in Figure 3. 12. The measured contact resistances were always 10^2 to 10^3 times smaller compared to the measured InN resistances. Extremely low contact resistance of Ti/Al/Ni/Au metallization on InN is demonstrated. The samples were showing ohmic with or without annealing, as it is known the ohmic behaviour was proposed to be associated with an electron accumulation layer in the InN and a Schottky barrier – height reduction mechanism. The sheet resistance is increasing with an annealing time upto 10 mins and then, it is decreasing as shown in Figure 3. 12. The lowest sheet resistance

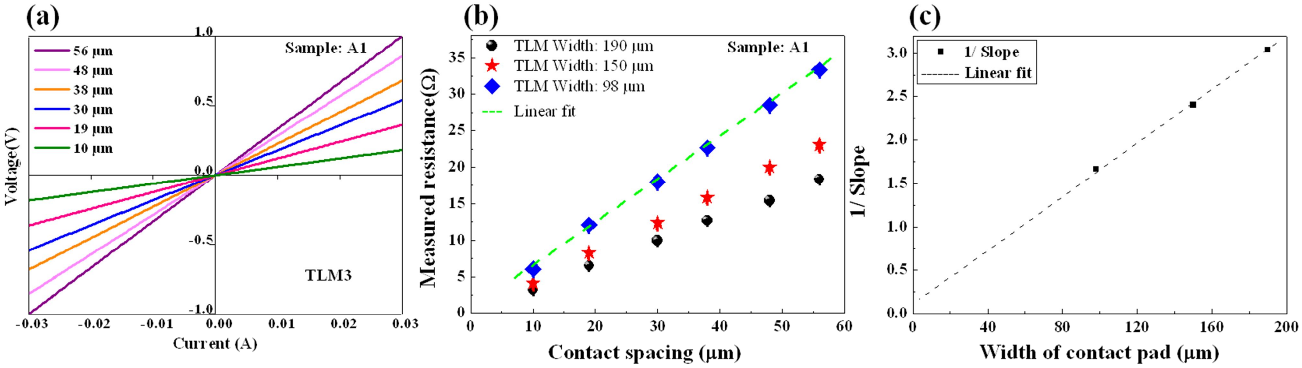

Figure 3. 11 (a) I versus V (b) measured resistance versus contact spacing for 3 TLMS with different widths, (c) Inverse of slope extracted from (b) versus widths.

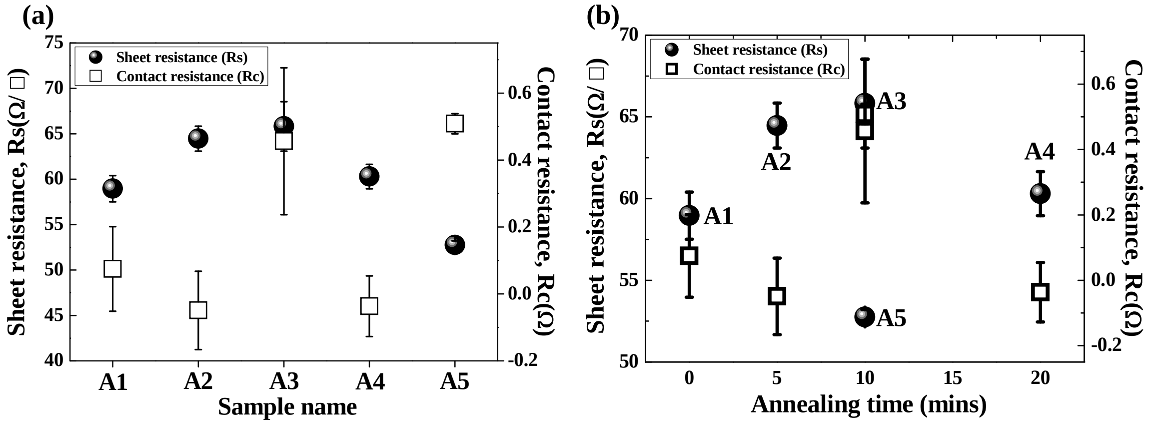

Figure 3. 12. Contact and sheet resistance of A samples series: (a) for each sample, (b) versus annealing time.

was observed for the sample A5, which has gone metallization prior to electrical isolation. However, the contact resistance is not sensitive for the difference in technological steps (A3 and A5). The error bars were extracted from the standard deviation of contact or sheet resistance with that of the average resistances.

Mapping of resistance and 1/f noise level

First a mapping of the electrical resistivity as well as the noise level was performed at room temperature. Each position was referenced by the (X, Y) position on the sample as indicated in Figure 3. 13(corresponding to figure 3.5 a). It is to be noted that, the resistivities are calculated here

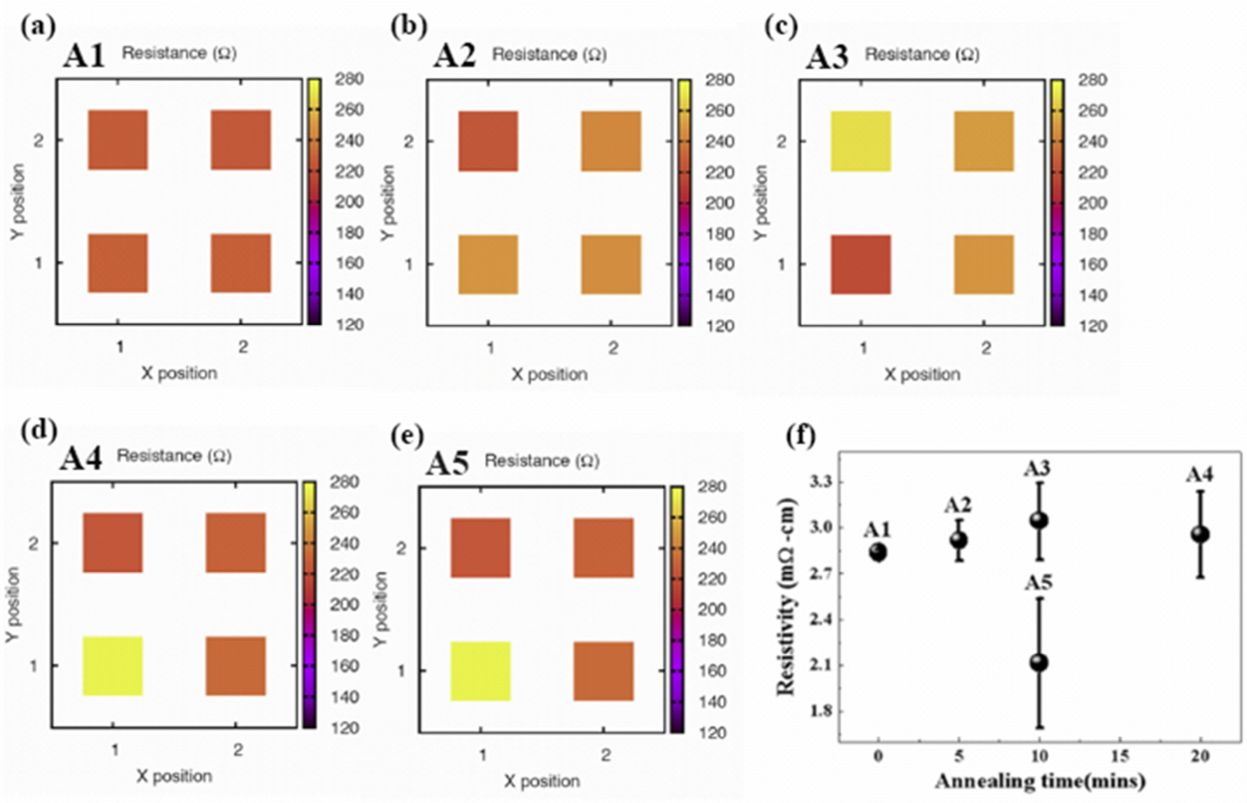

Figure 3. 13. (a)-(e) Mapping of resistances with colour code scales, (f) Resistivity versus annealing time.

as explained in chapter 2, by taking into account the nominal thickness of the InN layers. As it can be seen from the colour code scales in Figure 3. 13, the resistances of all of these samples are in the range between 280 Ω code. The dispersion in the resistances across the wafer is increased upon annealing and is more worsen with the metallization prior to electrical isolation as in sample A5. The average resistivities across the wafer are plotted with annealing time as depicted in Figure 3. 13

(f). The resistivity is slightly lower for A5. For all of these samples, the resistivities are in line with the literature[30]. The lower resistivity in A5 could be related as, after etching the mesas, the damage of InN was not cured by thermal annealing, which in turn resulted highly conductive paths along the side walls or the current crowding at the side walls.

The low-frequency voltage-noise analysis was performed at various bias currents. The spectra were acquired in the 10 Hz to 100 kHz frequency range. A typical frequency dependence of the spectral density S_V of voltage fluctuation processes in the investigated thin films is shown in Figure 3. 14 (a) for A3. Apart from a number of peaks at definite frequencies due to external noise sources, all the spectral density traces are seen with two main components. The first one, at low frequencies, which shows 1/*f* dependence and the other, is a constant amplitude spectrum, corresponding to white noise. The noise voltage spectral density S_V at 1 Hz has a quadratic dependence with the bias current. This

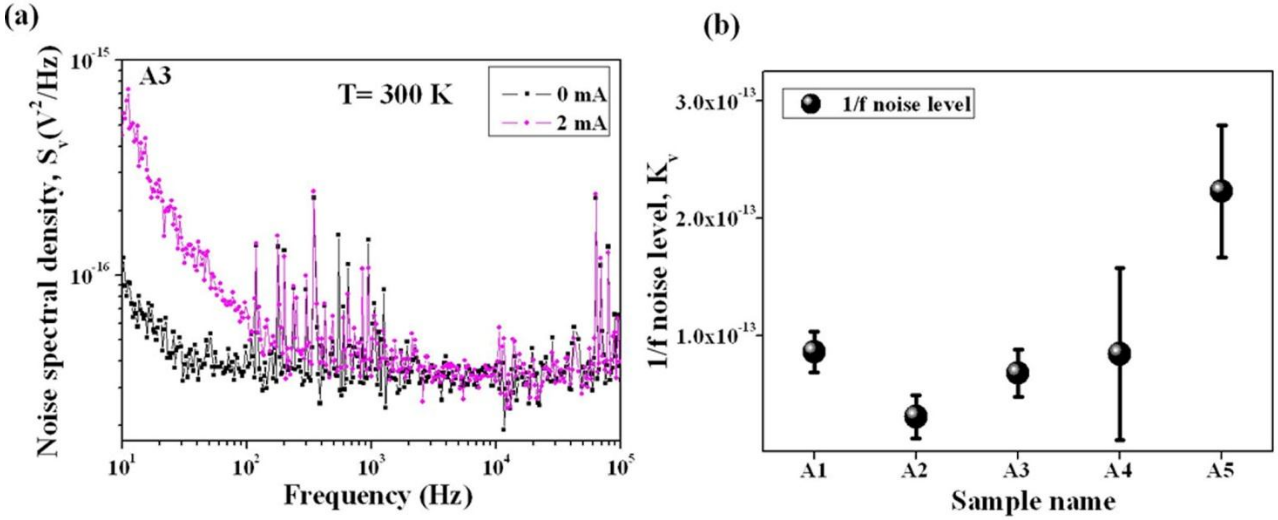

Figure 3. 14. (a) Voltage Noise spectral density for different DC bias currents for sample A3, (b) 1/f noise levels of all A series samples.

1/f noise level at 1 Hz and 1V defined as K_V (for equation see page number 18) . This is a measure of InN layers quality. This quantity K_v is plotted for all of these samples as shown in Figure 3. 14 (b). We observed that there is no significant change of 1/f noise level upon annealing and the dispersion in case of non annealed sample is less in comparison with other annealed or technologically different sample as A5. The sample A2, showed to have less level of noise.

A few conclusions were drawn after following the surface morphology, optical and electrical properties:

- The electrical isolation of InN layer has to be done before metallization, so further in these conclusions, we will mention only about the other samples (A1, A2, A3, A4)
- The thermal annealing has not showed to reduce the damage caused by mesa, as non annealed sample showed to emit high PL, dispersion of resistance over the wafer was less and the mean resistivity obtained was same of the order of other thermally annealed samples (A2, A3, A4). The 1/f noise is showed to have a small increase in comparison with A2, which is having the lowest 1/f noise level of all of these samples.
- Although, we could not see the effect of higher values of roughness of metal pads in comparison to InN layers, in electrical properties.
- A interesting point to be noted from PL studies that upon annealing, the band gap of InN layer is decreasing , which in turn reduces, the residual carriers in the InN layer. Hence a compromise has to be made, so it remains short time annealing should be the option.
- The noise levels obtained here are among the lowest one reported ever on InN. Using Hooge theory as mentioned in chapter 1, we calculate Hooge parameter, α_H to be about 2.4×10^{-3} has been compared with InAs which is about 1×10^{-3} at room temperature[31].

3.5 In and N rich InN layers

We have chosen A3, A5, B1, B2 and B3 InN epitaxial layers to study the effect of growth parameters on the electrical transport properties. All of these InN layers have carrier concentration of the order of 10^{18} cm^{-3}. The details of structural studies on these layers can be found in the reference[32].

3.5.1 Surface morphology

We have first, studied the surface morphology and roughness with AFM. Figure 3. 15 shows representative 5×5 μm^2 AFM images for the two distinct growth regimes in In-face InN. Figure 3.

15(a) shows the surface morphology of 400 nm InN sample grown with excess In. The InN surface of Figure 3. 15 (a) exhibited a relatively smooth morphology typical. This is a morphology characteristic of that seen in all In-face InN films grown with excess In. As reported throughout various studies, all samples grown with excess In exhibited In droplet accumulation visible by optical microscopy. Droplets became larger and more dense as increased excess In was supplied during growth[10]. In contrast, sample (B3) exhibits a much higher roughness due to N-rich growth conditions. This is agreement with Gallinat *et al.*[10] who reported that when In flux becomes lower than the N flux, the surface looses the step flow growth which is the characteristic of slightly indium rich conditions. For N-rich conditions, the differences in morphology between the two samples (A3 and B3) can be explained by the fact that in A3, we are further away from stoichiometry compared with B3.

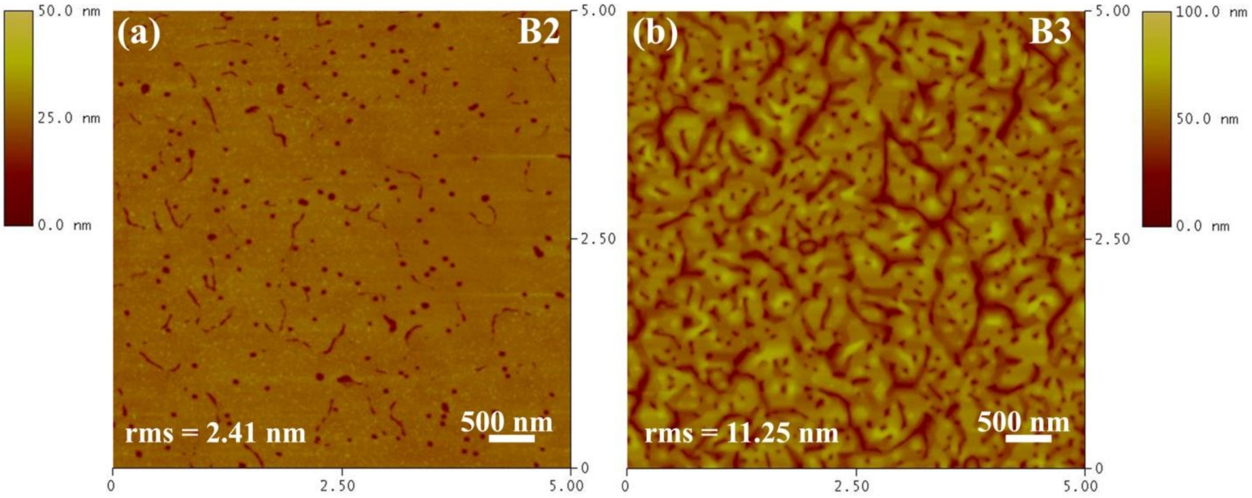

Figure 3. 15. A 5 × 5 μm^2 AFM micrographs of In-face InN layers grown on Ga-face GaN templates under (a) In-rich conditions, and (b) N-rich conditions. The growth temperature for both layers was 440° C.

3.5.2 Electrical properties studies at room temperature

Resistivity versus roughness

Figure 3. 16 shows the resistivity versus surface roughness for In rich and N rich InN layers. N rich samples (A3 and B3) exhibited higher roughness. The resistivity of InN layers are increasing with the increase of InN layers roughness. This is quite consistent with the literature[33]. Using Figure 3. 3, one can derive that $n \approx c/\sqrt{t}$ with $c = 9.48\text{x}10^{18}$ at/cm^3 to estimate mobility from the measured

resistivity. The estimated normalized mobility values are plotted in Figure 3. 16 (b) versus roughness along with silicon values from the reference 36. One can observe a clear dependency between charge carrier mobility and roughness as already observed in Silicon MOS devices[34].

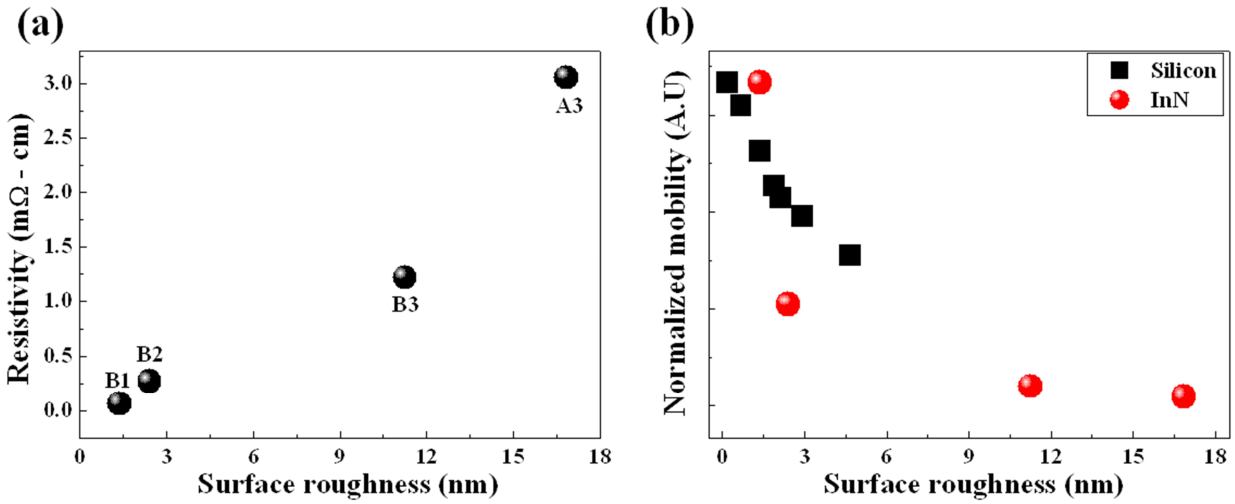

Figure 3. 16. (a) Resistivity versus surface roughness of In and N rich InN layers at room temperature , (b) Normalized mobilities of InN layers and Silicon MOS devices from reference 33.

It is known that in MOS devices, the voltage bias of the gate creates an inversion layer at the interface with the dielectric gate. Thus conduction only occurs at the surface of the Silicon layer. This data extracted from reference 33 were also been plotted as shown in Figure 3. 16(b) and one can notice the similarity in the two trends observed for these two different materials. Surface roughness dependence with mobility indicates the existence of a surface charge layer in these samples. As a conclusion these mobility values trend with surface morphology can be interpreted as a surface mechanism. It is to be noted that, it is difficult to estimate the absolute values in mobility since; we do not know the real conduction thickness in InN.

Resistivity versus Noise

DC and noise measurements have been performed on all devices at room temperature using the following conditions. From DC measurements, electrical resistivity was deduced. The noise measurements were performed at different bias voltage. S_V at 1 Hz was deduced and then plotted versus voltage across the sample to deduce K_v.The noise parameter K, given by, $K = K_V . W . L . t$

(where *W*: width, *L*: length of the geometry across which noise measurements were performed and t: thickness of InN layer), was calculated to remove the geometry dependence of these electrical parameters. Then these K values are plotted versus electrical resistivity for all the devices available on each wafer in Figure 3. 17.

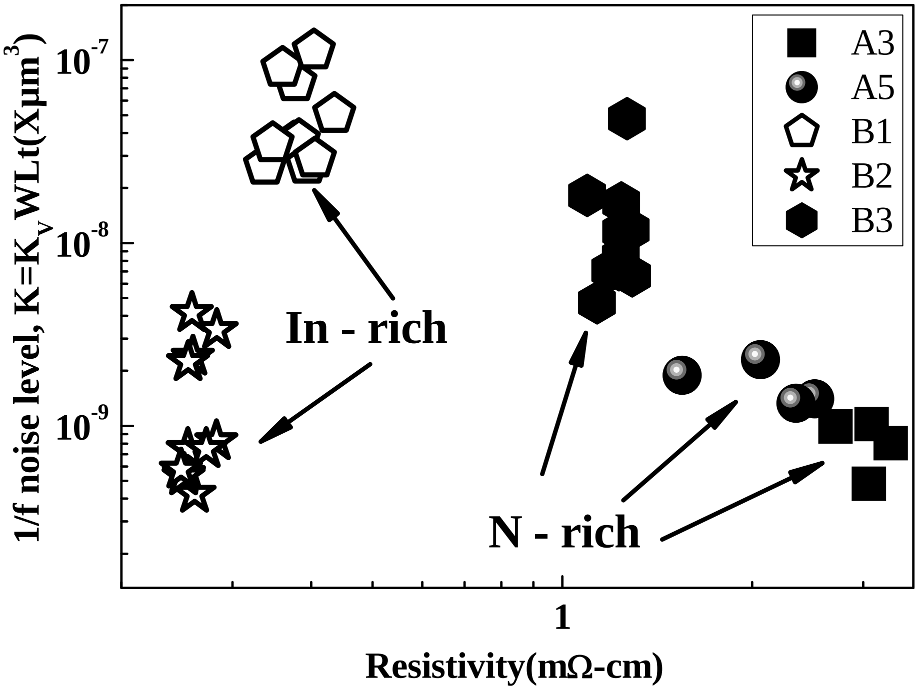

Figure 3. 17. Mapping of resistivity and 1/f noise level of all available devices at room temperature for slightly In rich and N rich InN layers.

It can be observed that electrical resistivity varies over less than one decade. The noise level dispersion is more than two decades from wafer to wafer and less than one decade within one wafer. No clear dependency between these two parameters can be observed. The impact on the N or In rich is visible only in electrical resistivity, showing that noise source are not directly connected to these morphology parameters. Even if these layers are MBE grown the K values obtained and TEM pictures reported on the same wafers in the reference 32, clearly show that multiple origins of fluctuation (surface, interface states or defect in the vicinity of the surface) exist. Each of them may contribute in different ways and different level of fluctuation. More time will be needed to achieve defect free layers where correlation between noise level or morphology parameters could be observed. Even in silicon process where the technological steps are well controlled, this kind of correlation is difficult to find and were not often reported[35].

3.5.3 Electrical properties studies with temperature

As seen above, in N rich InN MBE layers, it is possible to estimate transport properties more precisely, so we have chosen A3 and B3 samples to investigate electrical resistivity and low frequency noise properties with temperature 77 K to 300 K. Current-Voltage (I-V) characteristics of InN patterned layers showed an ohmic behaviour for both the InN material and the metallic contacts in the whole temperature range.

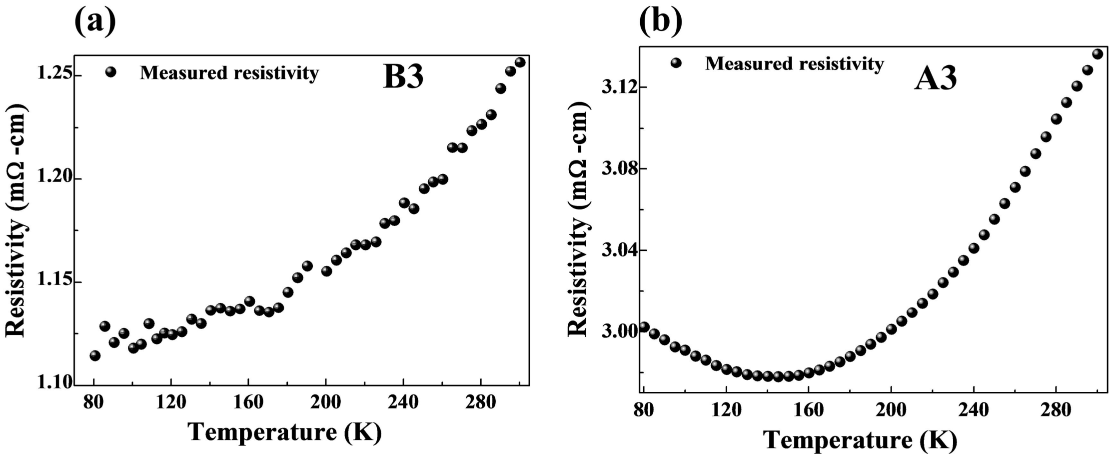

Figure 3. 18. The electrical resistivity of the InN layer between 77 K and 300 K.

The measured contact resistances were always $10^{3 \text{ to }}$ 10^2 times smaller compared to the measured InN resistance for B3 and A3 samples respectively. A decrease in the electrical resistivity with decreasing temperature down to approximately 130 K was observed as can be seen in Figure 3. 18. The temperature dependence of the resistance above 130 K exhibited a positive temperature coefficient of about 7.70 x 10^{-4} K^{-1} at 300 K(for instance in sample B3), which is in agreement with reported results in InN nanowires.[36] This resistivity dependence with temperature is characteristic of a metal like behaviour in contrast to a non-degenerate semiconductor.[36, 37]

In order to better understand the physical mechanisms behind the transport properties in these InN layers, noise measurements at different temperatures have been carried out. As pointed out in chapter 1, Low frequency noise sources and especially 1/f noise sources are related to mobility fluctuations in the bulk[38]or number fluctuations which usually originate from the surface[39]. (For more details refer to section 1.5.6 of chapter 1 and annex I)

The identification of this kind of fluctuation mechanisms can be used to probe electrical conduction.

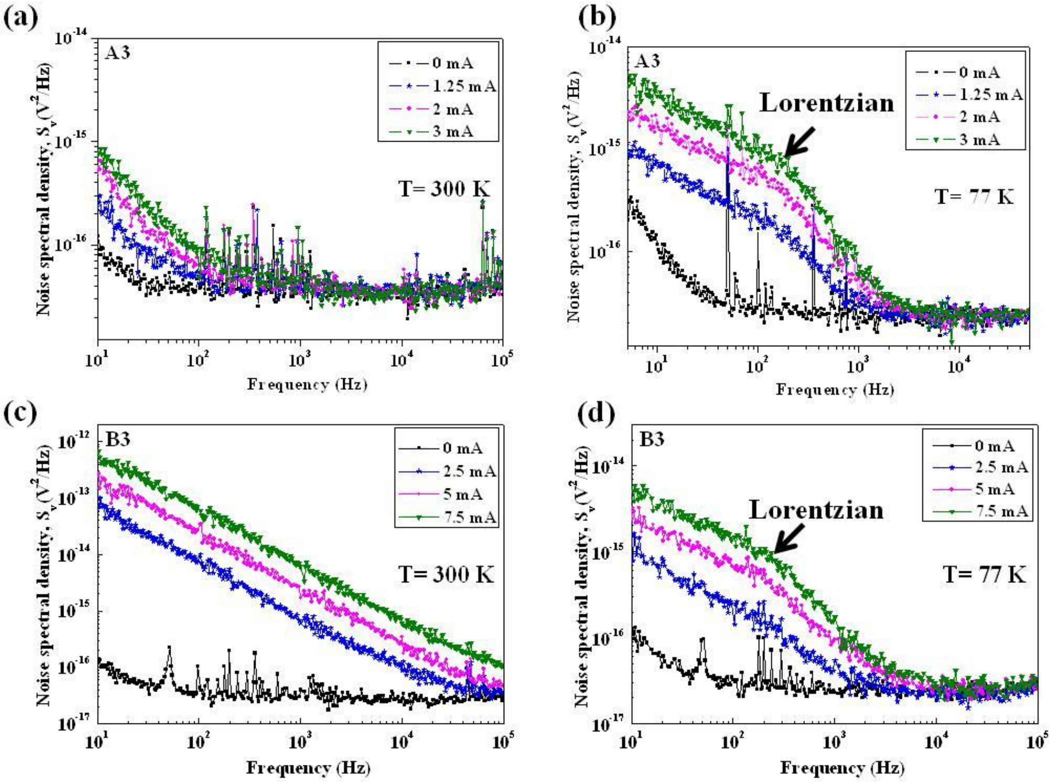

Figure 3. 19. Voltage noise spectral densities measured for different DC bias currents: (*a*) and (c) at 300 K the curves are dominated by the 1/f noise contribution. (b) and (d) At 77 K, a Lorentzian contribution is now visible (shown with an arrow).

Figure 3. 19 shows two examples for B3 and A3 of typical noise spectral densities S_v as a function of frequency for different bias currents. These measurements were performed on a 94 µm wide and 210 µm long bridge on TLM1 (see Figure 3.7 b) for sample B3. For A3 sample, we have conducted noise as well as resistivity studies on geometry III shown in Figure 3.5. Before each noise measurement at different bias currents and temperatures, the resistance of the devices was systematically measured to check that it did not vary in the considered bias current range as a consequence of self heating. In Figure 3. 19, two different trends were observed above and below 100 K. Above 100 K up to 300 K range, the spectra clearly consisted of following two parts: a 1/f

noise contribution that depends on the bias current and frequency, and the white noise part which remains constant Figure 3. 19 (a and c). For each temperature the measured white noise level was in agreement with the dc electrical resistance according to $4k_BTR$, where k_B is the Boltzmann constant. The slope of the low frequency part was around -1 in the 10– 100 Hz frequency range, thus confirming the “1/f” behavior. We checked the quadratic dependency of Sv versus the bias current (0 to 7.5 mA in case of B3 and 0 to 3 mA in case of A3), as expected in homogeneous samples. At lower temperatures (≤ 100 K), apart from the 1/f noise and white noise, a Lorentzian shape appears with a characteristic frequency f_c and plateau levels that depend on the temperature (Figure 3. 19 d). The characteristic frequency of the Lorentzian curves did not depend on the bias current and it decreased when the temperature was reduced as illustrated in Figure 3. 20.

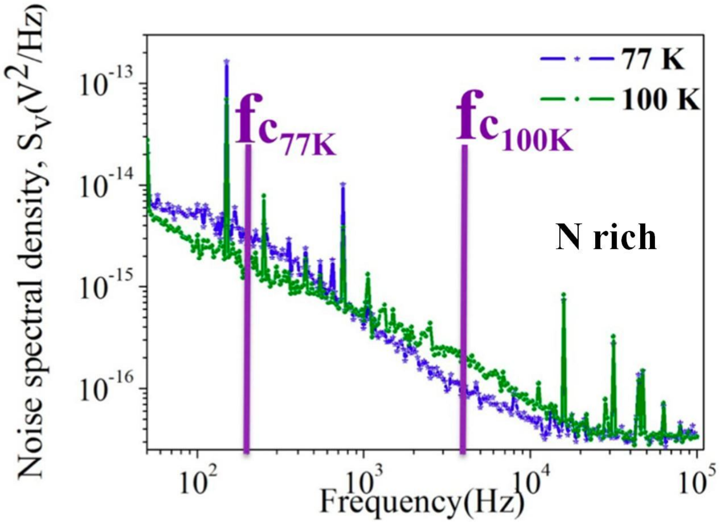

Figure 3. 20. Characteristic lorentzian frequency variation with temperature (sample B3): fc_{77K}. fc_{100K} are the lorentzian frequencies for sample B3.

As described in chapter 1, this Lorentzian profile is attributed to a Generation Recombination process due to a trap that has a discrete energy level in the band gap. A single relationship $\tau = \frac{1}{2\pi f_c}$ exists between the time constant τ of the trap and the characteristic frequency of the Lorentzian[40]. The Arrhenius diagram obtained by plotting $ln(\tau.T^2)$ as a function of $1/(k_BT)$ is shown in Figure 3. 21. For all the devices under study, the results were identical and showed a clear linear dependence. Using equation (1.10) in chapter 1, the energy level of the trap was deduced from the slope of the linear fit, its energy position being around 52 meV for B3 and 55 meV for A3, below the conduction band minimum.

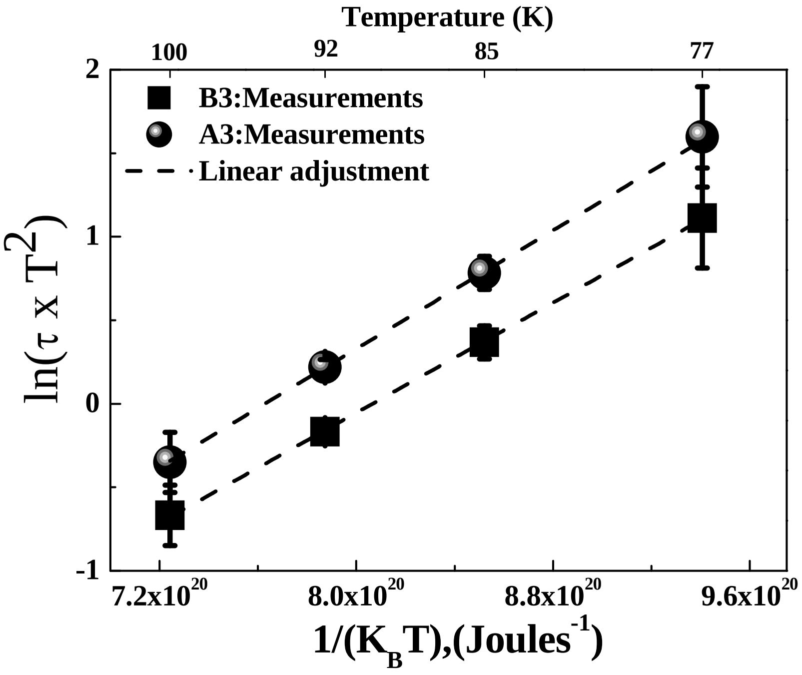

Figure 3. 21. The Arrhenius diagram obtained for N rich InN layers by plotting *ln(*$\tau.T^2$*)* as a function of *1/(*k_BT*)*, a trap energy level of 52 meV for B3 and 55 meV for A3 respectively below the conduction band minimum is obtained.

As a consequence, these results can be interpreted as a transition from non degenerated (below 100 K) to a degenerated semiconductor. For temperature higher than 100 K, only 1/f noise is observed and the electrical resistivity increases with the temperature: InN acts like a metallic conductor and no single trap generation recombination process can be observed. Below 100 K, Lorentzians appear and electrical resistivity is more or less constant with the temperature (Figure 3. 18): InN acts as a semiconductor. It was possible to probe a bulk trap thus indicating the part of the electrical conduction occurs in the bulk. A volume charge carrier number fluctuations was thus probed by the LFN measurements.

After subtraction of the Lorentzian, the 1/f noise level from 77 K up to 300 K is observed and plotted the same in Figure 3. 22. All the measurements values have been normalized to 1 at room temperature to keep an insight on the temperature variation. Two typical trends can be observed: (i) an increase with temperature from 80 K for B3 device and starting upper 100 K for A3 and A5 devices. (ii) a decrease or a constant value for the lowest temperature. In order to explain these behaviors, basic models were tested in order to distinguish between number or mobility fluctuations with constant doping of free carriers. The concerned mathematical derivation about this model is given in the annex I.

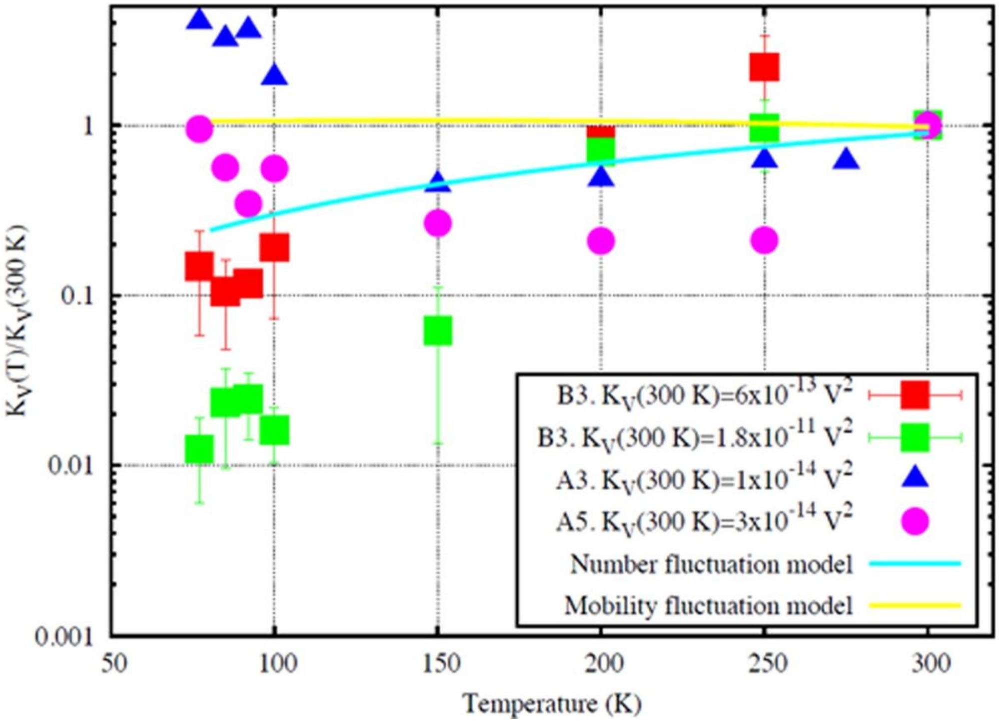

Figure 3. 22. The normalized 1/f noise level with versus temperature with number and mobility fluctuation models. The normalization of 1/ f noise levels was done at room temperature values.

Mobility fluctuations model predicts either no or a small decrease of the 1/f noise level with temperature. On the other hand, number fluctuation model predicts an increase of the noise. Therefore, it follows that our measurements are better explained with number fluctuations which are probably originating at the surface, with a constant concentration of free carriers. Therefore, at higher temperatures (>100K), the measured 1/f noise agrees with the already reported surface charge accumulation of InN[17]. The measurements at low temperature cannot be explained by these models. In this range of temperature, either the concentration of free carriers of the mobility may be effected by another mechanism such as carriers freezing that have already been reported in this range of temperature. However, this point needs further investigations with new measurements at lower temperature to extend the range of investigated temperature.

In summary, LFN measurements were performed on MBE grown InN layers from 77 K up to 300 K. The increase in the 1/f noise level with temperature may be a confirmation of the electron accumulation layer at the surface which was already reported by other techniques. However, the Lorentzians observed at or below 100 K and the evolution of their characteristic frequencies with temperature are consistent with a generation-recombination mechanism due to a discrete trap level which has been determined at around 50 meV below the conduction band. These results show that with the present technique, it is possible to probe the part of the electrical conduction that takes place in the bulk of InN films.

3.6 Conclusions

DC measurements on TLM patterned InN layers, revealed an extremely low contact resistance of non alloyed Ti/Al/Ni/Au metallization, which is about 10^3 times lower than the sheet resistances.

The effect of different fabrication steps and annealing effect draw a conclusion of: annealing induces dispersion in electrical resistivity over the entire wafer; however annealing time did not show effective differences in the measured electrical resistivities of InN layers. As dispersion indicates the material non homogeneity across the wafer, annealing should be avoided in order to achieve a good quality contacts. As the dispersion in resistivities as well as 1/ f noise levels are higher as compared to the wafers which have gone electrical isolation prior to metallization, electrical isolation after metallization has to be avoided,

The resistivities of In rich and N rich InN layers at room temperatures showed a strong relation with the surface roughness, indicating the dominant electrical conduction is at the surface.

The estimation of Hooge parameter of these InN layers from 1/ f noise revealed that the low frequency noise is sensitive to the material quality as these InN layers having a high dislocation densities of ~ 10^{10} cm^{-2}, shows the InN layers quality is comparable with that of GaAs and InAs devices.

The low frequency noise versus temperature showed that there exist a number of charge carrier fluctuations which indicates that a part of electrical conduction takes place at the surface, which is coherent with the electron accumulation layer at the surface.

Though the 1/ f noise levels variation and even levels are different for both of these samples A3 and B3, we noticed the located trap levels are around 50 meV. This indicates that these traps are intrinsic of the InN layers. The noise measurements versus temperature probed a trap level near the conduction band, which gives an indication of accessing bulk electrical conductivity in InN layers.

3. 7 References

---

[1] T. L. Tansley and C. P. Foley, “Optical band gap of indium nitride”, J. Appl. Phys. **59**, 3241 (1986).

[2] J. Wu, W. Walukiewicz, K. M. Yu, J. W. Ager III, E. E. Haller, H. Lu, W. J. Schaff, Y. Saito and Y. Nanishi, “Unusual properties of the fundamental band gap of InN”, Appl. Phys. Lett. **80**, 3967 (2002).

[3] A.G. Bhuiyan, A. Hashimoto, A. Yamamoto, “Indium nitride InN: A review on growth, characterization and properties”, J. Appl. Phys. **94**, 2779 (2003).

[4] K. I. Lin, J. T. Tsai, T. S. Wang, J. S. Hwang, M. C. Chen, and G. C. Chi, “Drift current dominated terahertz radiation from InN at low-density excitation”, Appl. Phys. Lett. **93**, 262102 (2008).

[5] V. M. Polyakov and F. Schwierz, “Low-field electron mobility in wurtzite InN”, Appl. Phys. Lett. **88**, 032101 (2006).

[6] T. Inushima, M. Hingashiwaki, T. Matsui, T. Takenobu and M. Motokawa, “Low-field electron mobility in wurtzite InN”, Phys. Rev. B **72**, 085210 (2005).

[7] S. X. Li, J. Wu, E. E. Haller, W. Walukiewicz, W. Shan, H. Lu and W. J. Schaff, “Hydrostatic pressure dependence of the fundamental bandgap of InN and In-rich group III nitride alloys”, Appl. Phys. Lett. **83**, 4963 (2003).

[8] S. Ruffenach, M. Moret, O. Briot and B. Gil, “Ammonia: A source of hydrogen dopant for InN layers grown by metal organic vapor phase epitaxy”, Appl. Phys. Lett. **95**, 042102 (2009).

[9] T. D. Veal, C. F. McConville and W. J. Schaff “Indium Nitride and Related Alloys”, CRC Press Taylor & Francis Group, Chapter 2 (2010).

[10] C. S. Gallinat, G. Koblmüller, J.S. Brown and J. S. Speck “A growth diagram for plasma-assisted molecular beam epitaxy of In-face InN”, J. Appl. Phys. **102**, 064907 (2007).

[11] G. Koblmüller, C. S. Gallinat and J. S. Speck , “Surface kinetics and thermal instability of N-face InN grown by plasmaassisted molecular beam epitaxy” J. Appl. Phys. **101**, 083516 (2007).

[12] M. A. Herman and H. Sitter, "Molecular Beam Epitaxy Fundamentals and Current Status”, Springer, Verlag, 2nd edition (1996).

[13] M. Stutzmann, O. Ambacher, M. Eickhoff, U. Karrer, A. Lima Pimenta, R. Neuberger, J. Schalwig, R. Dimitrov, P. J. Schuck, and R. D. Grober, “Playing with polarity”, Phys. Stat. Sol(b) **228**, 505 (2001).

[14] K. Xu and A. Yoshikawa, “Effect of film polarities on InN grown by molecular beam epitaxy”, Appl. Phys. Lett. **83**, 251 (2003).

[15] K. Xu,W. Terashima, T. Hata, N. Hashimoto, Y. Ishitani, and A. Yoshikawa, “Step-flow growth of InN on N-polarity GaN template by molecular beam epitaxy with a growth rate of 1.3 μm/h”, Phys. Stat. Sol (c) , **381**, 377 (2002).

---

[16] W. J. Schaff, H. Lu, L. F. Eastman, W. Walukiewicz, K. M. Yu, S. Keller, S. Kurtz, B. Keyes, and L. Gevilas, "State-of-the-Art Program on Compound Semiconductors XLI-and-Nitride and Wide Band Gap Semiconductors for Sensors, Photonics, and Electronics", in V. H. Ng and A. G. Baca, editors, Fall ECS meeting Proceedings, **06**, ISBN 1-56677-419-5 (2004).

[17] H. Lu, W. J. Schaff, L. F. Eastman, and C. E. Stutz, "Surface charge accumulation of InN films grown by molecular-beam epitaxy", Appl. Phys. Lett. **82**, 1736 (2003).

[18] H. Lu, W. J. Schaff and L. F. Eastman, "Surface chemical modification of InN for sensor applications", J. Appl. Phys. **96**, 3577(2004).

[19] I. Mahboob, T. D. Veal, C. F. McConville, H. Lu, and W. J. Schaff, "Intrinsic electron accumulation at clean InN surfaces", Phys. Rev. Lett. **92**, 036804 (2004).

[20] C. H. Swartz, R. P. Tompkins, N. C. Giles, T. H. Myers, H. Lu, W. J. Schaff and L. F. Eastman, "Investigation of multiple carrier effects in InN epilayers using variable magnetic field hall measurements", J. Cryst. Growth **269**, 29 (2004).

[21] A. Vilalta-Clemente, G. R. Mutta, M. P. Chauvat, M. Morales, J. L. Doualan, P. Ruterana, J. Grandal, M. A. Sanchez-Garcıa, F. Calle, E. Valcheva, and K. Kirilov, "Investigation of InN layers grown by molecular beam epitaxy on GaN templates", Phys. Stat. Sol (a) **207**, 1079 (2010).

[22] K. A. Rickert, A. B. Ellis, F. J. Himpsel, H. Lu, W. Schaff, J. M. Redwing, F. Dwikusuma, and T. F. Kuech, "X-ray photoemission spectroscopic investigation of surface treatments, metal deposition, and electron accumulation on InN", Appl. Phys. Lett. **82**, 3254 (2003).

[23] T. D. Veal, I. Mahboob, L. F. J. Piper, C. F. McConville, H. Lu, and W. J. Schaff, "Indium nitride: Evidence of electron accumulation", J. Vac. Sci. Technol. B **22**, 2175 (2004).

[24] L. Colakerol, T. D. Veal, H. K. Jeong, L. Plucinski, A. DeMasi, T. Learmonth, P. A. Glans, S. Wang, Y. Zhang, L. F. J. Piper, P. H. Jefferson, A. Federov, T. C. Chen, T. D. Moustakas, C. F. McConville, and K. E. Smith, "Quantized Electron Accumulation States in Indium Nitride Studied by Angle-Resolved Photoemission Spectroscopy", Phys. Rev. Lett. **97**, 237601 (2006).

[25] R. P. Bhatta, B. D. Thomas, M. Alevli, and N. Dietz, "Surface Electron Accumulation in Indium Nitride Layers Grown by High Pressure Chemical Vapor Deposition", Surf. Sci. Lett. **601**, L120 (2007).

[26] W. Walukiewicz, "Intrinsic limitations to the doping of wide-gap semiconductors", Physica B **302**, 123 (2001).

[27] X. Wang, S. B. Che, Y. Ishitani, and A. Yoshikawa, "Systematic study on *p*-type doping control of InN with different Mg concentrations in both In and N polarities", Appl. Phys. Lett. **91**, 242111 (2007).

[28] G. R. Mutta, J. –M. Routoure, B. Guillet, L. Méchin, J. Grandal, S. Martin-Horcajo, T. Brazzini, F. Calle, M.l A. Sánchez-García, P. Marie and P. Ruterana, "Volume charge carrier number fluctuations probed by low frequency noise measurements in InN layers" , Appl. Phys. Lett. **98**, 252104 (2011).

---

[29] T. B. Fehlberg, C. S. Gallinat, G. A. Umana-membreno, G. Koblmüller, B. D. Nener, J. S. Speck and G. Parish, “Effect of MBE Growth Conditions on Multiple Electron Transport in InN”, J.Elect. Mats. **37**, 593 (2007).

[30] P. A. Anderson, A Ph.D thesis on “Indium Nitride: An Investigation of Growth, Electronic Structure and Doping”, University of Canterbury, New Zealand (2006).

[31] M. Tacano, M. Ando, I. Shibasaki, S. Hashiguchi, J. Sikula and T. Matsui, “Dependence of Hooge parameter of InAs heterostructure on temperature”, Microelectronics Reliability **40**, 1921 (2000).

[32] A. Vilalta-Clemente, A Ph.D thesis on “Structure of InN and InAlN alloys”, University of Caen (2012).

[33] H. Marom and M. Eizenberg, “The effect of surface roughness on the resistivity increase in nanometric Dimensions”, J. Appl. Phys. **99**, 123705 (2006).

[34] T. Yamanaka, S. J. Fang, H. –C. Lin, J. P. Snyder and C. R. Helms, “Correlation Between Inversion Layer Mobility and Surface Roughness Measured by AFM”, IEEE Electron Device Letts. **17**, 178(1996).

[35] N. Valdaperez, J. –M. Routoure, D. Bloyet, R. Carin, S. Bardy, J. Lebailly. “Low frequency noise in single-poly bipolar transistors at low base current density”, Microelectronics Reliability 41, 265 (2001).

[36] C. Y. Chang, G. C. Chi, W. M. Wang, L. C. Chen, K. H. Chen, F. Ren and S. J. Pearton, “Transport properties of InN nanowires”, Appl. Phys. Lett. **87**, 093112 (2005).

[37] T. Richter, H. Lüth, T. Schäpers, R. Meijers, K. Jeganathan, S. Estèvez Hernández, R. Calarco and M. Marso, “Electrical transport properties of single undoped and n-type doped InN nanowires”, Nanotechnology **20,** 405206 (2009).

[38] F. N. Hooge and L. K. J. Vandamme, “Lattice scattering causes $1/f$ noise”, Phys. Lett. A **66**, 315 (1978).

[39] A. L. Mcwhorter, PhD thesis on “1/f noise and related surface effects in Germanium”, Massachusetts Institute of Technology (1955).

[40] V. Grassi, C. F. Colombo, and D. V. Camin, “Low frequency noise versus temperature spectroscopy of recently designed Ge JFETs”, IEEE Trans. Electron Devices **48**, 2899 (2001).

Chapter 4

InGaN Quantum Wells: Transmission Electron Microscopy and Photoluminescence studies

This chapter addresses the issue of the origin of high emission efficiency in InGaN/GaN quantum wells (QWs) for solid state lighting applications. In this context, we have characterized the structure, morphology and chemical composition of the QWs, in order to determine how they are affected by the growth conditions and to correlate this with the optical properties.

4.1 Introduction and Motivation

Wurtzite nitride semiconductors are under an extensive worldwide research attention as highest potential materials for the realization of multicolour emitting diodes and laser diodes, due to the wide range of emission wavelengths which extends from ultraviolet to near infrared[1,2].The development of InGaN alloys opened the way to all solid state light sources such as blue and green LEDs, white LEDs[3]. The nitride semiconductor laser diodes are used from flat panel displays to compact disc players, for instance 400 nm laser diodes[1] for high density optical storage. Recent developments confirmed InGaN system capability in photovoltaic applications[4] as well. At present, highly efficient violet and blue-emitting diodes have been achieved[5,6], but this is not yet the case for green LEDs6[,7]. For longer wavelengths LEDs, these alloys need to contain higher concentrations of In, this gives rise to poor crystalline quality. Additionally, a large piezoelectric field results with high Indium content and forms another bottleneck to achieving high emission efficiency. Nevertheless, a large amount of research is going on all over the world to sort out this issue.

4.1. 1 Effect of polarization fields in InGaN/GaN QWs

In the InGaN/GaN system, the lattice mismatch increases rapidly with the indium concentration and the resulting piezoelectric polarization dominates over the spontaneous polarization. Fiorentini *et al.*[8] theoretically predicted a strong bowing of the polarization properties upon alloying, which was referred to as ‘‘nonlinear polarization’’.

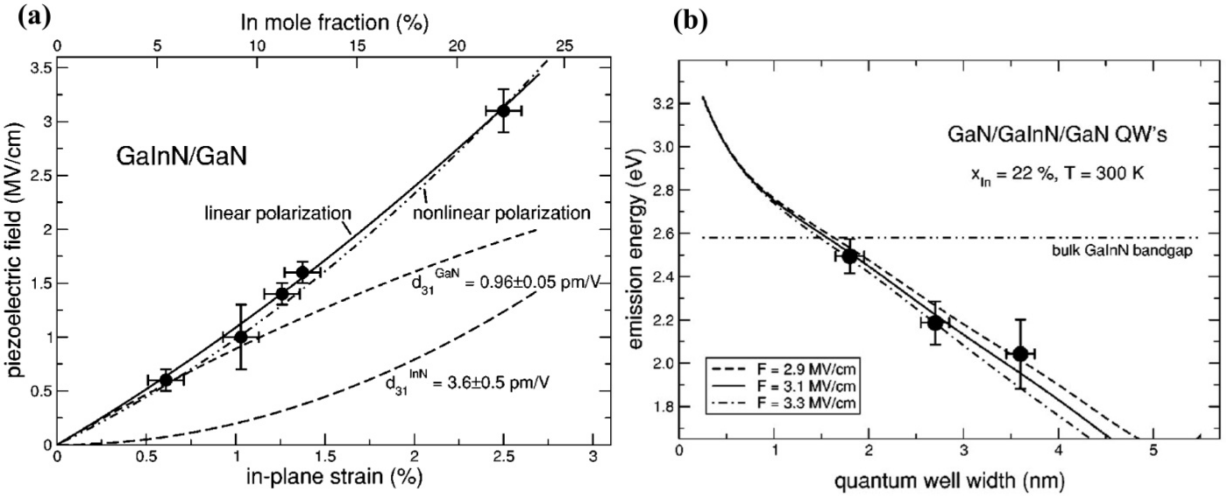

Figure 4. 1. (a)Polarization field vs in-plane strain (In mole fraction), (b) Emission energy vs well width for a series of GaN/GaInN/GaN multiple QWs with about 22% In[9].

An experimental determination of the internal polarization field in GaInN/GaN QWs, due to piezoelectric and spontaneous polarization was done by Hangleiter *et al*[9]. Figure 4. 1a shows almost linear increase of the field with increasing In content and pseudomorphic strain which was determined from a series of QWs. The full line represents a quadratic fit to the data, the dashed lines represent the components associated to GaN and InN, respectively. The dashed-dotted line is from first-principles calculations[6]. The magnitude of the internal fields in InGaN/GaN QWs was estimated from PL emission energy with QW width variation. The emission energies obtained from a series of GaN/GaInN/GaN multiple QWs with about 22% In and different QW widths is shown in Figure 4. 1b. The best fit was obtained for a field of 3.1MV/cm[6].

4.1.2 Origins of high efficiency emission in InGaN Quantum Wells

In comparison with GaAs based devices, nitride devices exhibit a higher efficiency[1] in spite of high defect densities ≥ 10^8 cm^{-2} which can be present inside the active layers[10,11,12,13]. Moreover, the insertion of InGaN underlying layer under InGaN QWs showed pronounced quantum efficiency in comparison to GaN underlayer[14]. In the same vein, it was recently shown that inserting delta InN layer in InGaN QWs or using staggered InGaN QWs, can improve the emission efficiency[15,16]. Up to date, there is a number of models which have been proposed to explain the origin of this defect-insensitive emission[17, 18, 20, 23, 32, 34]. The exhibition of high efficiency in nitride semiconductors, has been often attributed to the presence of In rich clusters that behave like quantum dots and limit the interaction of the excitons with the dislocations[17,18,19, 20, 21,22]. Figure 4.2 shows a TEM image of InGaN MQWs which exhibits many dark spots in the wells. The diameter of these dark spots ranges from 2 nm to 5 nm. It has been proposed by Narukawa et al[14], that the dark spots originate from isotropic dot-like structures which were self-formed in the wells.

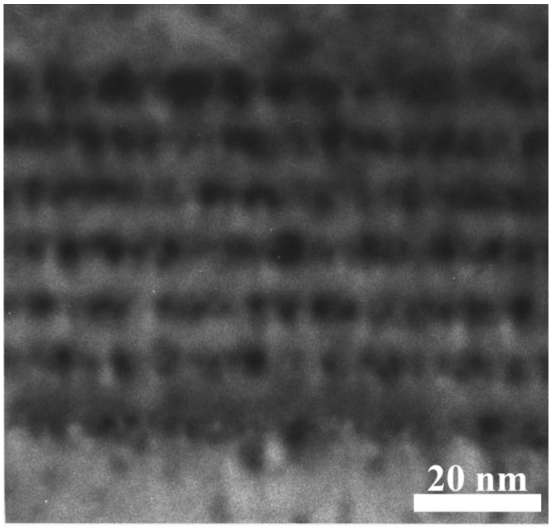

Figure 4. 2 Magnified TEM image showing the MQW region[14].

However, more recent reports have shown that such image contrast could be due to electron beam damage if no particular care is taken during sample analysis in the TEM[23]. Smeeton et al[20] investigated the InGaN QWs sensitivity to irradiation by the electron beam in TEM. Figure 4. 3 (a) and (b) shows high-resolution TEM images, acquired during the first seconds of irradiation at the QW region and the same area after a few minutes of exposure to electron beam. As it can be seen from these HRTEM images, the relatively uniform contrast of the InGaN in the first image (Figure. 4.3a) are replaced by strong local changes in intensity in the second (Figure 4.3 b). It was concluded that such changes in image contrast could be related to the development of an inhomogeneous strain in the InGaN lattice, which may erroneously be attributed to indium clustering. Subsequently, a thorough analysis of the best practice for obtaining the correct information has been proposed, it appears that exposure times of an area below some 20 s will not be enough to introduce alterations at 200 KeV[24,25, 26].

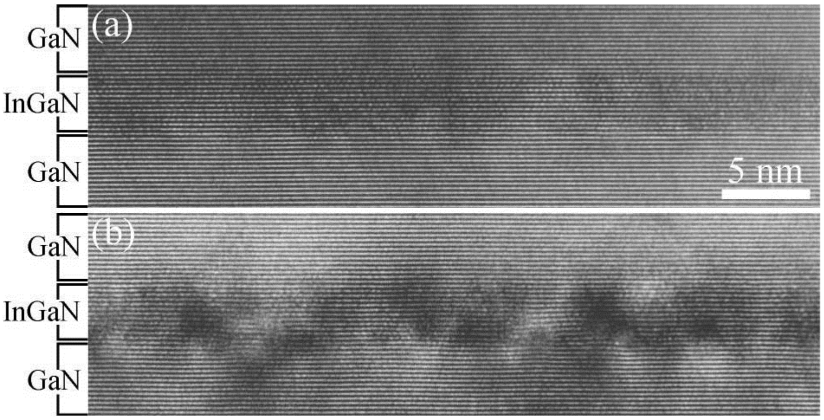

Figure 4. 3. (0002) lattice fringe images of an In0.22Ga0.78N SQW: (a) recorded within 20 s of first exposing this part of the QW; (b) same area after a few minutes of exposure to a 400 kV electron beam[23].

There are few reports available in the literature which quote the nano scale phase separations an evidence for localization centres in InGaN layers as the root of high efficiency[27, 28]. Indeed phase diagram investigations have shown that GaN and InN should have a miscibility gap at temperatures between 600°C and 850ºC[29,30]. More recently, Chichibu et al[31] reported that the existence of In–N–In–N zigzag chains gives raise to localization of carriers inside InGaN alloys rather than by 2-3 nm In rich clusters. These widely believed concepts of gross indium fluctuations was also questioned by Humphreys et al[32], who proposed to correlate the high efficiency in InGaN/GaN system with the QW thickness fluctuation. In their work, a three dimensional atom probe analysis of InGaN QWs did not show any indium clustering. Figure 4. 4 shows a reconstruction of the InGaN/GaN structure with the indium and gallium atoms displayed. Four QWs are clearly visible, in which the bottom three of these QWs were chosen to analyze in detail for the indium distribution, because, the top

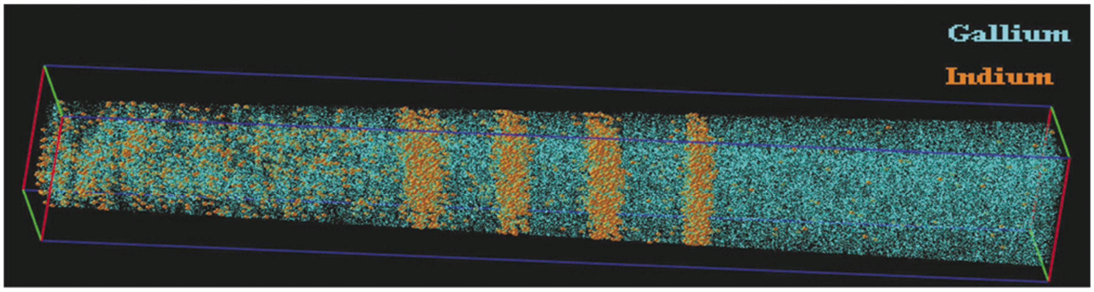

Figure 4. 4. Three-dimensional Atom Probe Field Ion Microscope (3DAP) image ofInGaN/GaN multi quantum wells. Each dot represents a single atom: light blue is Gallium and orange is Indium[32].

well may have been damaged by sample preparation. As compared to the indium distribution in a random alloy, no significant deviations were found in the three QWs, leading the authors to conclude that there was no evidence of indium clustering in their sample. However, other authors still believes in possible clustering in InGaN QWs which may depend on the growth conditions[33], so the controversy is still going on.

On the other hand, a different process has been proposed by Hangleiter *et al.*[34], for high emission efficiency of InGaN-based QW light emitting diodes, which relies on screening by defects. In this instance, during the growth of the QWs, hexagonal V-shaped pits which form on top of threading dislocations exhibit {10-11} growth facets with a smaller growth rate than along the [0001] direction, leading to smaller thicknesses for the sidewall QWs (as shown in Figure 4.5). Such QWs exhibit higher bandgaps and form a potential barrier around the corresponding dislocation. The authors proposed that such configuration keeps carriers from recombining non- radiatively at the defect core. The so-called V- shaped defects are one of the most common defects which are frequently observed in (0001) grown InGaN thick layers and InGaN/GaN MQWs[35,36,37,38].

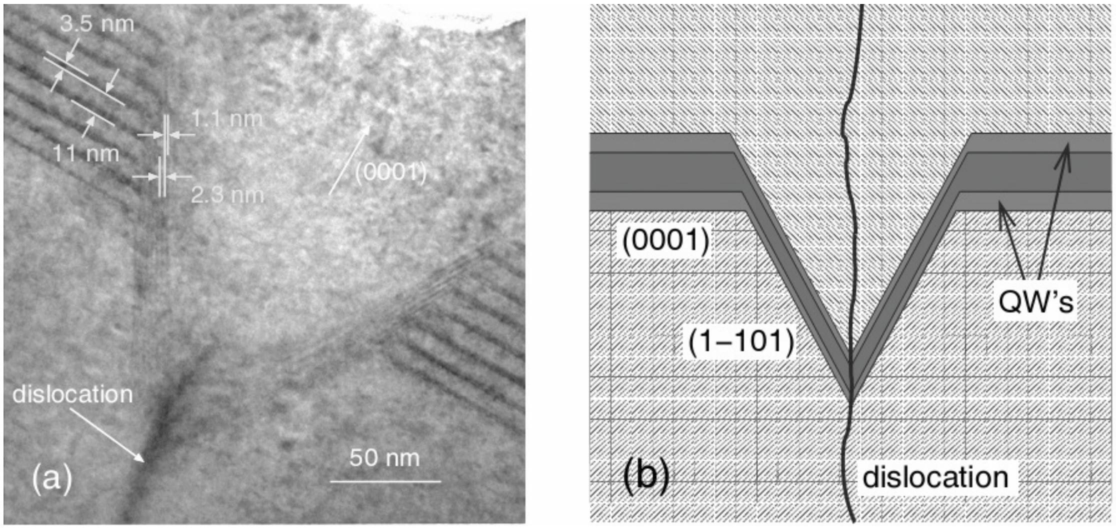

Figure 4. 5 TEM image a) of an InGaN/GaN MQW structure and b) a schematic illustration of the QW structure in the vicinity of a TD induced V-pit[34].

In this chapter, we report on our investigation of the structure of InGaN QWs within an effort to correlate it with the optical properties. To this aim, we have carried out Transmission Electron Microscopy by minimizing the electron dose on carefully prepared InGaN QWs grown by Metal Organic Vapour Phase Epitaxy (MOVPE) and/ (or) Molecular Beam Epitaxy (MBE). The objective is to determine the effect of V-pits on QW widths as well as the Indium distribution inside the wells versus the growth conditions. PL studies were carried out to connect the peak emission intensity and energy with QW thickness, In composition possible fluctuations.

4.2 The samples

This chapter discusses the results obtained on three different sets of InGaN/GaN QW structures grown in three laboratories. The first set of samples was grown by Metal Organic Vapour Phase Epitaxy (MOVPE), or Molecular Beam Epitaxy (MBE) and by use of the two techniques on the same wafer, at EPFL, Lausanne, Switzerland. The second and third set of samples was grown by MOVPE technique at CRHEA Valbonne.

EPFL samples (Set-I): The first two samples (L210 and L212) were grown by MBE technique, they were made of one QW, in this case, the varying parameter has been the nominal thickness of the QW; the next two samples (A1809 and A1807) were grown by MOVPE and were either made of one QW, or two QWs of equivalent nominal thickness. The fifth sample was made of one QW grown by MOVPE, on top of an additional QW was deposited by MBE. All the samples were grown on commercial Lumilog templates (c-plane sapphire with MOVPE GaN of 4 µm thickness).

CRHEA samples (Set-II): This is a set of three samples 1386, 1389 and 1425, which were grown by MOVPE. The first two samples were 5 periods of InGaN QWs and the last is made of 30 QWs with the barriers doped with Si. All the active layers were grown in temperature range: 800 - 810 °C. The samples we investigated in this chapter are listed in Table 4.1.

Table 4. 1. Sample nominal specification

Source	**Growth technique**	**Specimen**	**No. of QWs**	**QW thickness (nm)**	**In%**	**Emission color**
EPFL (Set -I)	MBE	L210	1	2.5	25	Green
		L212	1	2	25	Blue
	MOVPE	A1809	1	1.5	25	Blue
		A1807	2	3	25	Green
	MBE & MOVPE	L248H	1	2	25	Blue
			1	3	25	Green
CRHEA (Set-II)	MOVPE	1386	5	2	25	Green
		1389	5	2	21	Blue
		1425	30	2	20.8	Violet

4.3 Microstructure studies of InGaN QWs for V-pits and its association with PL studies

4.3.1 Microstructure

One of the key issues is the presence of hexagonal shaped deep-pits on the surface of the samples. We analyze the behavior of the Threading Dislocation(TD) attached to V-pits, as it has been claimed the presence of v-pits is detrimental on the device characteristics.

EPFL sample (Set-I)

MBE QWs : The MBE QW sample is first subjected to TEM for investigation of TDs and their termination in the topmost layer. Figure 4. 6, shows a weak beam cross-sectional TEM micrograph taken around the $[10\bar{1}0]$ zone axis with diffraction vectors g such as g = (0002) were screw and mixed type of TDs are visible and the other along $g = (11\bar{2}0)$, for the edge and mixed type TDs are in contrast (not shown here). The TDs are noticed as bright lines propagating in a direction normal to the GaN surfaces are seen in Figure 4. 6, in which some of the TDs are started inside the GaN buffer layer and some originated from the substrate (which is not shown in figure). From the ***g.b*** criteria as described in Chapter 2, we identified these TDs as edge, screw and mixed types. Among them, the mixed type of dislocations is dominant in number comparatively to edge type of TDs with an even smaller number of screw type TDs. All the TDs which are shown with solid white arrows exhibit a mixed type of character. These TDs propagate from GaN to the surface, a larger view is shown for the TD surrounded by the rectangle (Figure 4. 6) and is discussed in the next paragraph (Figure 4. 7).

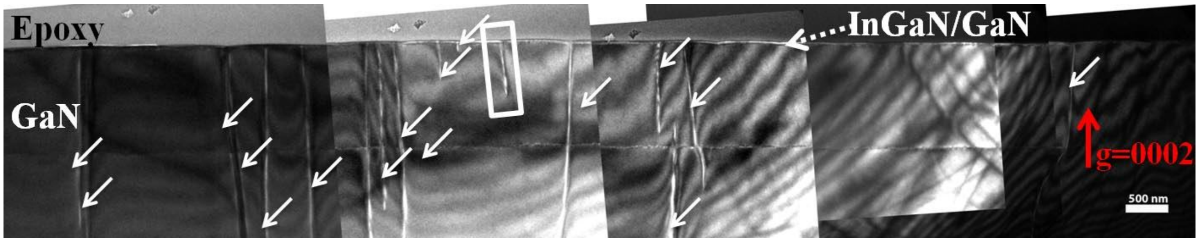

Figure 4. 6 Typical low magnification XTEM micrograph of MBE SQW (sample L210).

In this instance, the TD passes to the top of the GaN surface via InGaN QW, without being affected by the active layer. From Figure 4. 7, it is clear that there is no V-pit at the top of the dislocations in these MBE QWs.

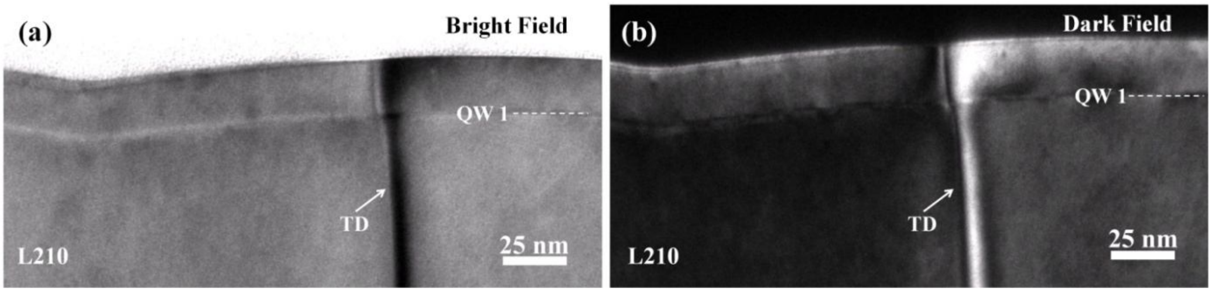

Figure 4. 7. A magnified view at the TD area which is surrounded by a rectangle shown in figure 4.6(sample L210). (a)Bright Field image and (b) Dark Field image taken under 2 beam condition same area and with g=0002.

MOVPE QWs: Previous reports have shown that, when V-shape defects in III-N materials are related to threading dislocations, they initiate at the threading dislocations, always extending along the growth direction in the InGaN heterostructure[39]. These TDs can be of edge, screw and mixed type of character, which has been reported earlier in this heteroepitaxial system. It has also been shown that the V-defects start at the onset of the first quantum well, second or third QWs[35, 40]. To obtain an insight about the V-pits association with TDs and also with QWs in MOVPE layers, we have observed the samples with a variation of well widths and In content inside the QWs. Figure 4.8 (a) and (b), shows a bright field image with single and double InGaN/GaN QWs containing V-pits , which originate in the GaN buffer layer, in case of SQW, and in case of DQW , the V-pits originate inside the GaN barrier. The two images, in Figure 4. 8, were recorded in two

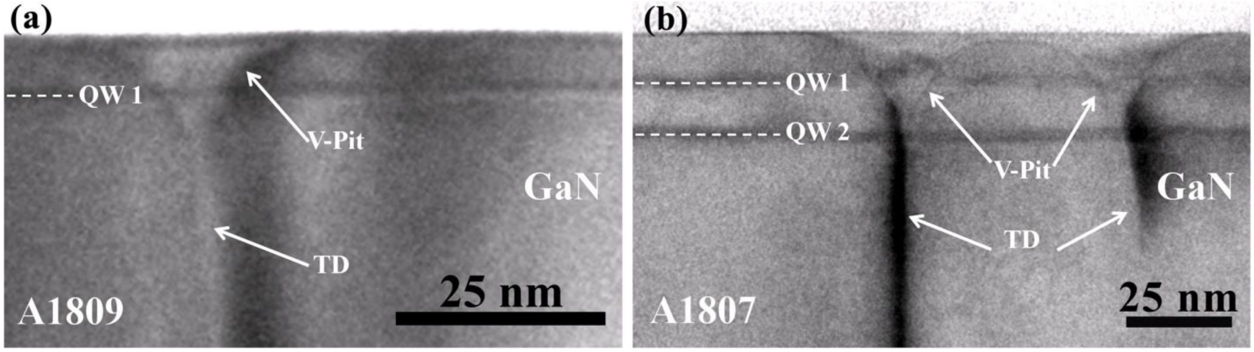

Figure 4. 8. Bright-field TEM image taken with *g*=0002 diffraction condition showing that V-defects are associated with mixed-component TDs; (a) MOVPE single QW (sample A1809), (b) A MOVPE double QW (A1807).

beam conditions with g=0002 near a <10-10> zone axis. By applying the diffraction contrast g.b, invisibility criteria, we concluded that the TD arriving from the GaN buffer layer and GaN barrier are mixed type of dislocations. At the vicinity of TDs, the QW remains flat and regular, showing no change on the QW geometry due to V-pit unlike the case reported in Hangleiter et al[34].

CRHEA samples (Set-II)

MOVPE QWs: In this case, we have observed MQWs which comprised of 5 and 30 InGaN periods. In these MQW structures, irrespective of its emission wavelength and number of InGaN periods, we noticed V-shape defect structures which are always connected to TDs as shown in Figure 4. 9 and Figure 4. 10 respectively. Figure 4. 9 shows dark field images taken with g=0002 beam condition for the two samples, one (1386 shown in the left-hand side of the image) emitting in blue-green and the other (1389, shown in the right hand side of the image) emitting in blue. In both cases, the V-pits are formed at the tip of the mixed type TDs. In case of 5 QWs, the V-pit is started at the 3rd QW from the top shown in Figure 4. 9 and in case of 30 QWs, in 2nd QW. A similar result has been reported by Sánchez et al[40]. We note that MOVPE QWs form V-pits irrespective of the well widths, growth conditions as they came from different laboratories. In all the cases, the TD stops at the apex of this V-defect. In all the MOVPE single or multiple QWs samples, the QWs thickness is not modified by the V-pit formation unlike the case mentioned by Hangleiter et al[34].

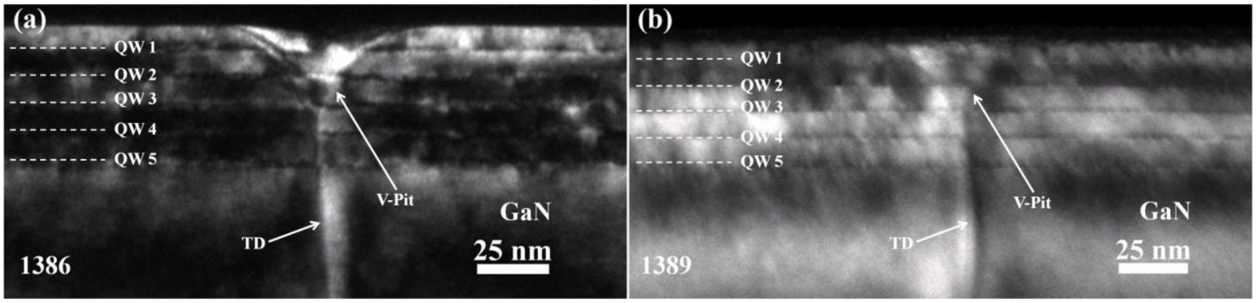

Figure 4. 9. Cross-sectional dark-field TEM images taken under two-beam diffraction conditions with g=0002: (a) sample 1386 emitting in green, and (b) sample 1389 emitting in blue. Both of these samples constituted of 5 QWs.

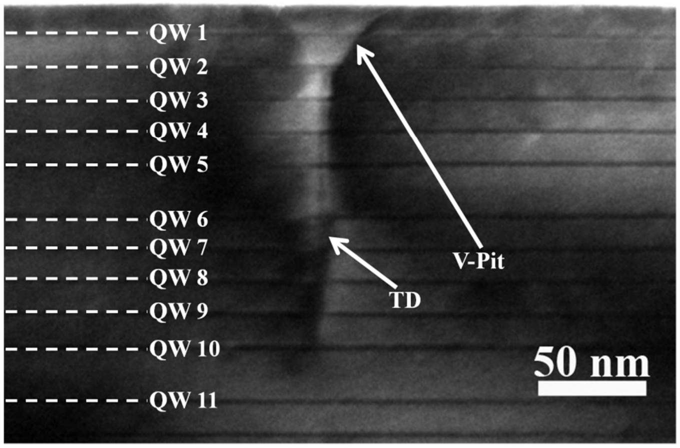

Figure 4. 10 Cross-sectional dark-field TEM images of sample 1425 taken under two-beam diffraction conditions with g=0002.

4.3.2 Optical properties of InGaN/GaN QWs

To see the influence of V-pits on the luminescence intensity, we carried out PL. A CW He-Cd laser was used as an excitation source at 325 nm. Figure 4. 11 shows, PL spectra of all InGaN QWs

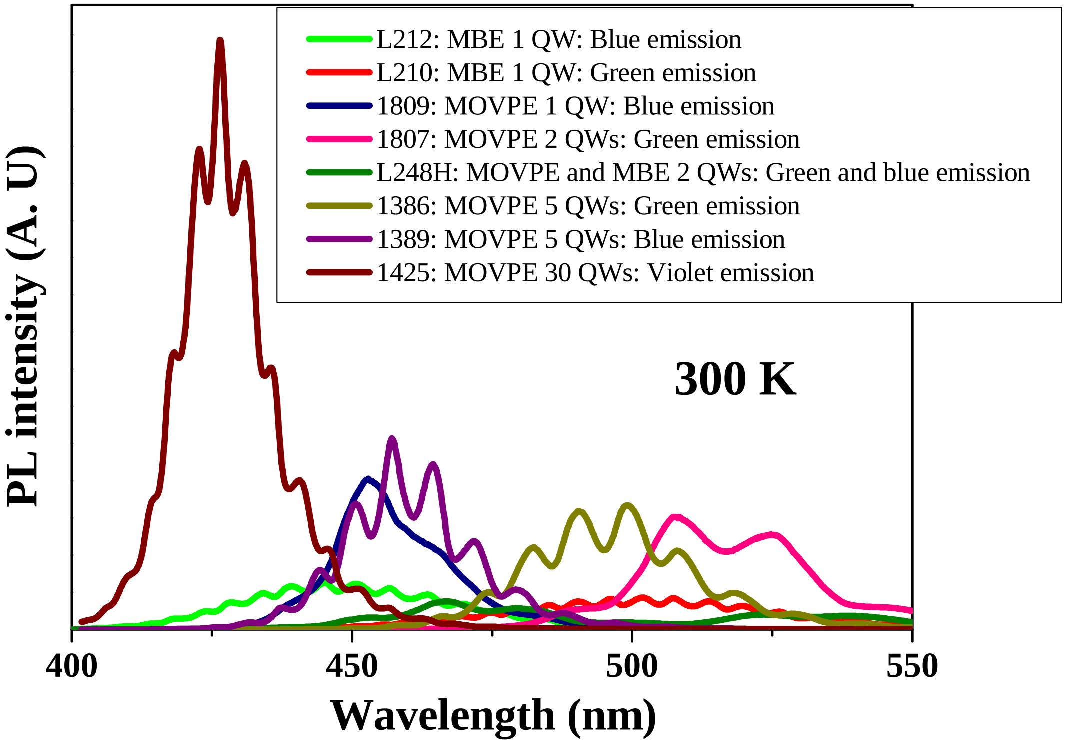

Figure 4. 11. Room temperature PL spectra for different In content layers of MBE and MOVPE grown layers.

samples taken at ambient temperature. At first glance, from the PL spectra one can notice a higher PL intensity for MOVPE QWs as compared with MBE grown QW. With increasing the number of QWs from 1 to 30, the optical emission intensity is strongly enhanced. Additionally, we can observe, in case of MBE QW, the PL spectrum is quite broad while in MOVPE QWs.

At this point, it may be stated that, the luminescence in our samples, may not be enhanced by the self screening of the defects as it has been reported in reference 34. In other words, the presence (in case of MOVPE) or absence (in case of MBE) of V-pits does not appear to have a direct correlation with the observed PL emission.

Photoluminescence studies at low temperatures: Figure 4. 12 displays low temperature PL spectra of single QW grown of MBE or MOVPE techniques. The PL measurement shows a peak centered around 492– 493 nm at 12 K for MBE QW, and as can be noticed in Figure 4.12, it is broad with a measured full width half maximum (FWHM) of ~300 meV, this result may be directly related to the QW irregular morphology as has been discussed earlier[41]. The corresponding PL spectrum is shown in Figure 4. 12. In this instance, we obtain an emission which is shifted more towards the blue ~ 450 nm and the corresponding FWHM is 54 meV, which is almost five times smaller than the previous MBE QW. This indicates that the optical quality of the QWs for MBE are severely

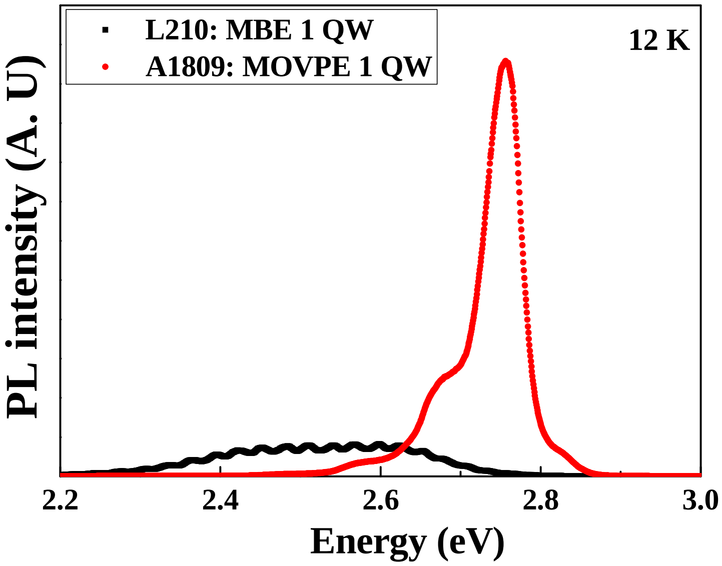

Figure 4. 12. PL spectra recorded at 12K for MBE Single QW (Sample L210) and MOVPE single QW (A1809).

degraded when compared to MOVPE QWs, which is more clear with the PL intensity in Figure 4. 11. Note that the first LO phonon replica appearing on the low energy side of the PL spectra[42].

In order to have a better insight into their optical properties, we have performed the temperature dependence of the PL peak energy. Figure 4. 13 displays PL spectra of a MOVPE double QW structure. It shows a double peak emission. Firstly one can notice in these PL spectra that the higher energy peak emission is reduced quickly by increasing temperature than that compared to the lower energy peak. These results indicate that the dominant emission is from the QWs[43]. This quenching of PL intensity can be attributed to alloy and interface fluctuations[44].

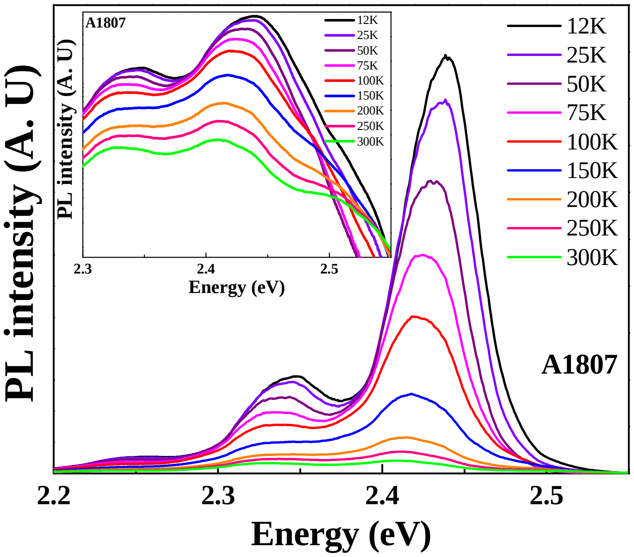

Figure 4. 13. Photoluminescence spectra, at various temperatures, of an InGaN/GaN QW structure with nominal In content of 25%. (Sample A1807). Inset figure: Semi log plot of PL versus energy.

The InGaN QW peak energy exhibits an S shaped behavior, in the temperature range of 12K – 300 K as shown in the inset of Figure 4. 13. It is believed that in InGaN alloys, the PL peak energy positions of InGaN, exhibits a S shaped behavior, which results from the carrier localizations in potential minimums and hence connected to In composition fluctuations[45]. Similar results were reported by Chichibu et al[46] in 20% In content InGaN MQWs, who concluded on the possibility of excitons localized at the potential minima originating from In composition fluctuation.

4.4 Microstructure analysis with CTEM, HRTEM and STEM

As it has been mentioned in the introduction, the other most quoted key possible origins for the high efficiency of InGaN/GaN QWs would be the presence of In rich clusters, well width fluctuations etc. In our case, we have pursued the microstructure investigations by High Resolution TEM (HRTEM) and STEM. The HRTEM extracted data was analysed using digital phase as well as peak finding procedures in order to extract the local strain and In compositions[47].

4.4.1 Microstructure and chemical composition studies with HRTEM

4.4.1EPFL sample (Set-I)

MBE QWs: For MBE grown QWs, we notice that the well width is systematically fluctuating, as can be seen in Figure 4. 14, the width goes from 0.5 nm to more than 2 nm, in this exhibited area. In lateral extension, the changes can take place at quite small scale, see arrows and the well morphology is changing from a quantum dot like, to more extended features. This well morphology can be connected to the low PL intensity in MBE QW, the corresponding PL was shown in Figure 4. 12 (a) and this may explain the large FWHM of 300 meV.

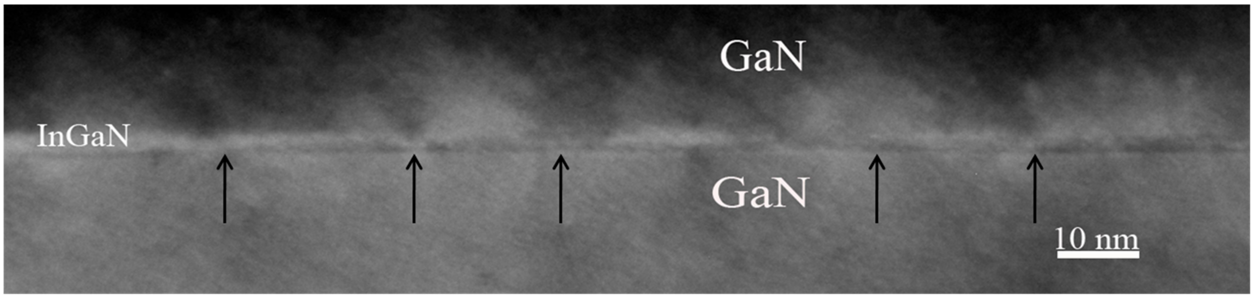

Figure 4. 14 Typical XTEM micrograph of MBE QW (sample L210)

A HRTEM micrograph as recorded within optimal conditions[24] is exhibited in Figure 4. 15, as can be noticed, from the colour coded strain map which had been superimposed, this area corresponds to a more or less quantum dot like feature. The well width is larger towards the middle of the image, where it extends up to close 2.0 nm and there is a decrease towards the borders of the image. From the maximum measured strain, we extract a local indium maximum composition of 29%.

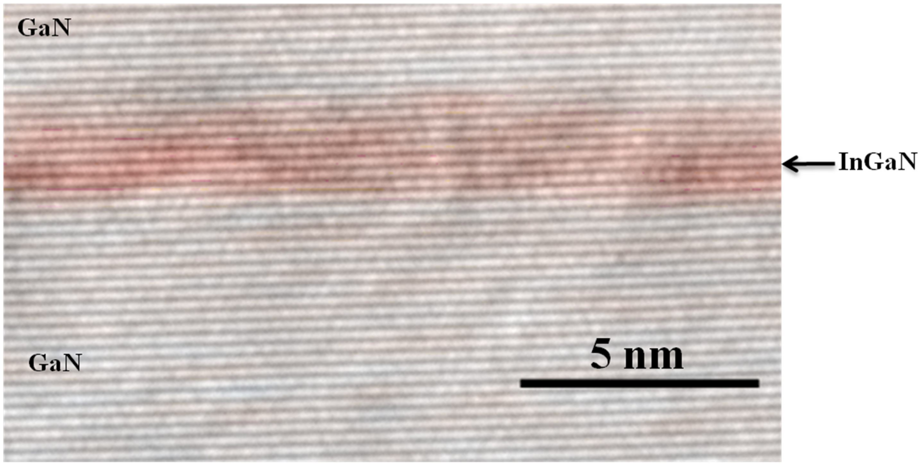

Figure 4. 15 Strain map superimposed on corresponding HRTEM image. (sample L210)

MOVPE QWs:

Single QW: In contrast to the MBE QWs, the MOVPE ones exhibit a homogeneous well morphology as can be noticed in Figure 4. 16 for sample A1809: the well thickness is uniform throughout and in this sample; it is measured as 1.4 nm. The corresponding PL spectrum shown in Figure 4. 12, evidences high efficiency, which could be correlated to this homogeneous well width morphology as determined at this scale. The corresponding HRTEM image is exhibited in Figure 4.

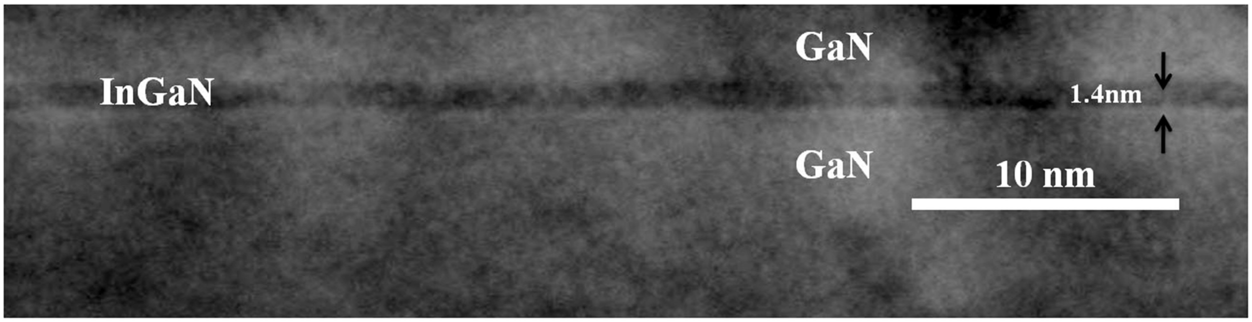

Figure 4. 16 Typical XTEM micrograph of MOVPE QW (sample A1809)

17, from the measured strain; we extract a local indium maximum composition of 27%, as can be noticed, at this smaller scale, there could some fluctuations in the local indium composition.

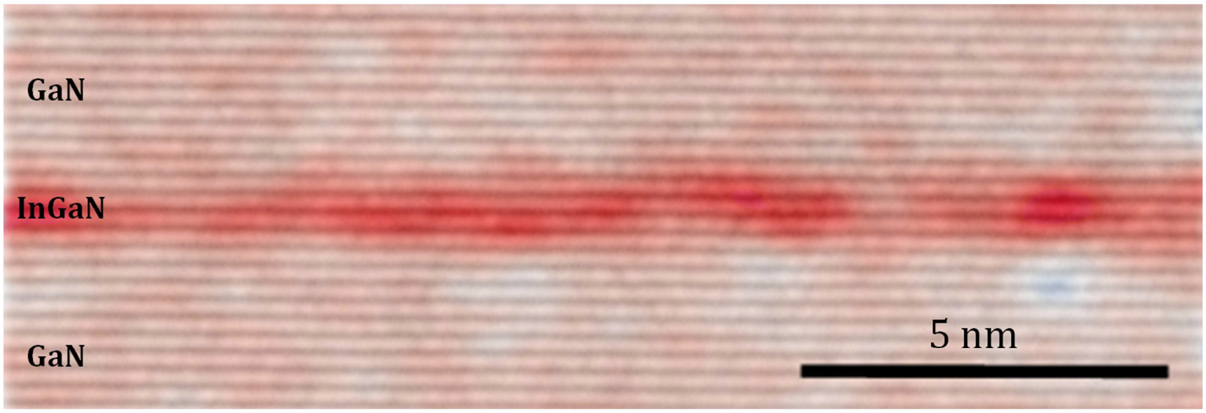

Figure 4. 17 Strain map superimposed on corresponding HRTEM image. (Sample A1809).

Double Qws: In case of double QWs grown by MOVPE, the results of one QW are confirmed and the well width is always homogeneous as exhibited in Figure 4. 18 for sample A1807. The measured thickness for two QWs is 2.6 and 2.9 nm, respectively.

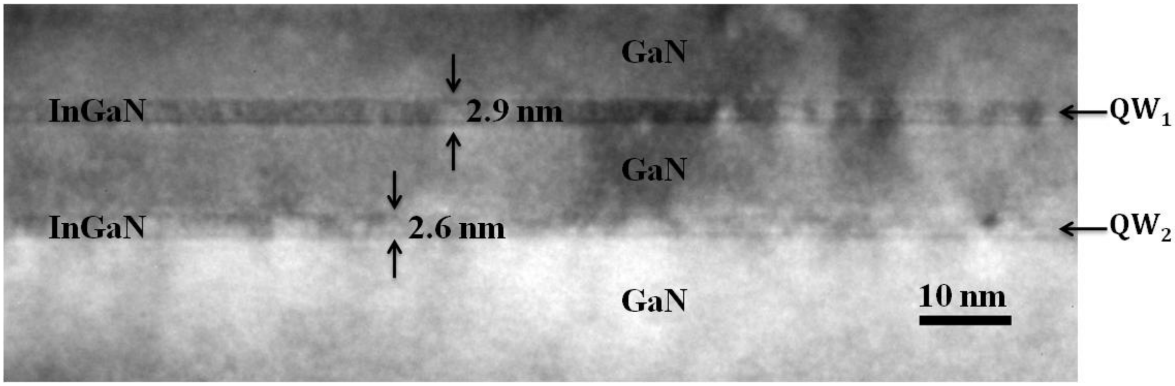

Figure 4. 18 Typical XTEM microgrpah of MOVPE QWs (sample A1807).

The corresponding PL spectrum recorded from 12K and room temperatures are shown in Figure 4. 13. In this instance we obtained a green emission at 510 nm. Considering the above two cases of MOVPE QWs (sample 1809 and 1807) of PL spectrum, we observed an increase in PL energy with the decrease in QW thickness consistently with the confinement effect[48].

Combined MBE and MOVPE QWs: An interesting case is shown in sample L248H where an MBE QW was grown on top of MOVPE one. In this case, as expected from the above observation the MOVPE well is easily noticed with its homogeneous thickness (see Figure 4. 19), whereas, the MBE one on top exhibits thickness fluctuations.

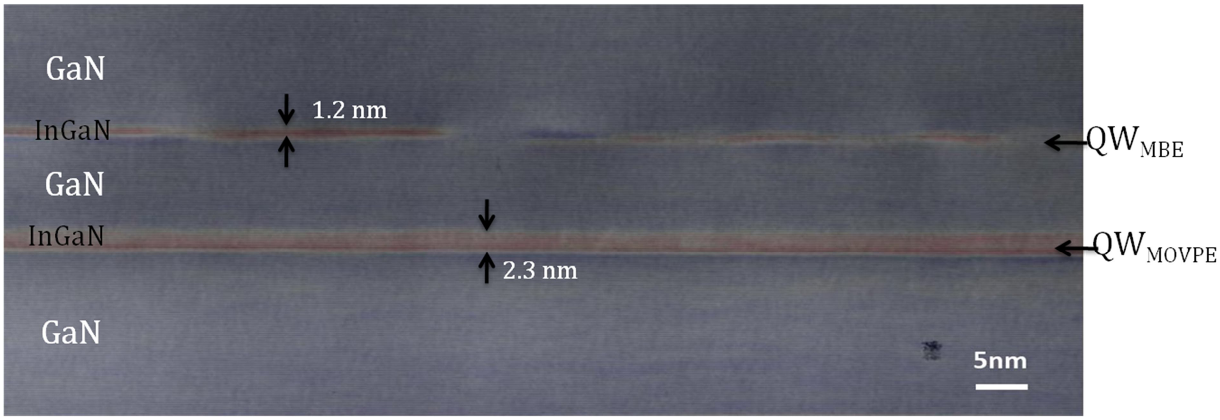

Figure 4. 19 Typical XTEM micrograph of MBE AND MOVPE QWs (sample L248H)

This image is completely consistent with the PL emission as exhibited in Figure 4. 11, the green narrow FWHM emission of the MOPVE QW is corresponding to the 2.3 nm uniform thickness, whereas, the MBE peak is large and towards the blue, also in agreement with the fluctuations and the smaller average thickness.

4.4.2 HAADF Investigations

High-angle annular dark field (STEM-HAADF) was next used to have a more accurate measurement of the QW thicknesses. In the following we discuss the results obtained for two samples (L248H and 1425). As shown in Figure 4. 20, the white contrast allows to determine precisely the location of the QWs. In Figure 4. 20 (a), the MOVPE QW exhibits a homogeneous thickness (2.08 nm), and the MBE well is not only narrower, but its thickness fluctuation is also visible, in agreement with the conventional TEM observations. In sample 1425, from the 30 QWs, we show only five QWs, and as can be seen, they exhibit a very homogeneous thickness of (1.99 nm). The High Resolution STEM image of one of these 5 QWs of sample 1425 is shown in Figure 4. 20 (c). Although the two MOVPE samples L 248 and 1425, exhibit homogeneous thickness, a closer look with HRSTEM image in Figure 4. 20, reveals the interfaces of 1425 samples are abrupt than

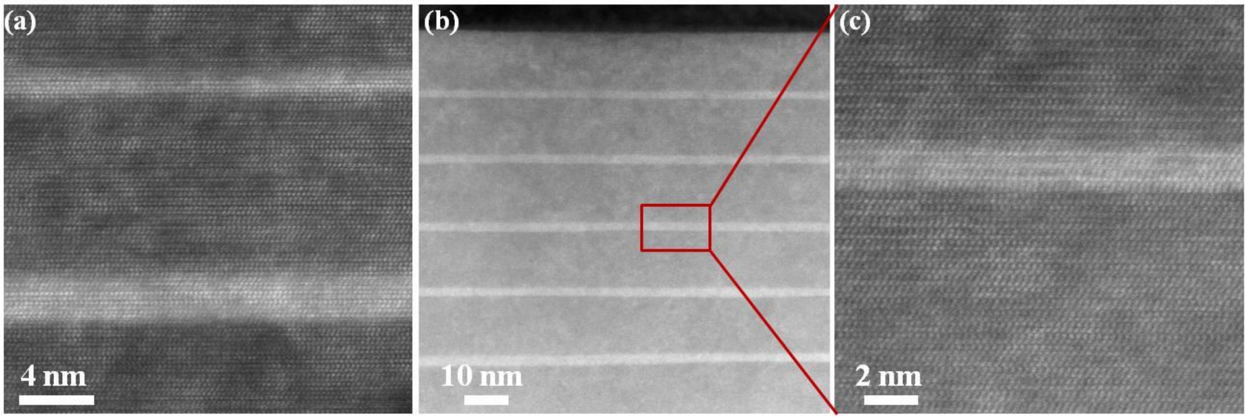

Figure 4. 20: STEM images (a) A High resolution STEM image of sample L248H, (b) A STEM image of a part of InGaN/GaN periods in sample 1425 and (c) A High resolution STEM image of one of the QWs in 1425.

that of MOVPE in sample L248, which indicates the fact that Si doping of GaN barriers results enhanced abrupt interfaces. These cross-sectional STEM images reveal QWs with highly perfect interfaces as shown in Figure 4. 20 a, b and c respectively. The uniform contrast inside the QW regions gives an indication of no phase separation.

In order to determine the indium composition, we chose L248H to describe here in the observed areas; one can use directly the image contrast. To this end profiles are taken and the background is subtracted with reference to the GaN (see detail in the appendix II). The thickness evolution of the sample in the area of interest is extracted from the fit of the background and the In composition is then obtained by a comparison of the resulting final profile to the theoretical ones that have been obtained through simulations. The obtained values are summarized as follows: 248H (QW1: In= 12.5%, QW2: 19%); 1386 (23.3); 1425 (14.1%).

4.4.3 Comparison of extracted In composition with literature

In order to properly compare the optical emission, QW width and the extracted In composition of the InGaN/ GaN QWs by taking into account the quantum confined stark effect and quantum well effect, we have reported here the data from the literature and as well as our own results on the same graph. The small open circles, small open triangles represent the experimental data from references 49 and 50 in Figure 4. 21.

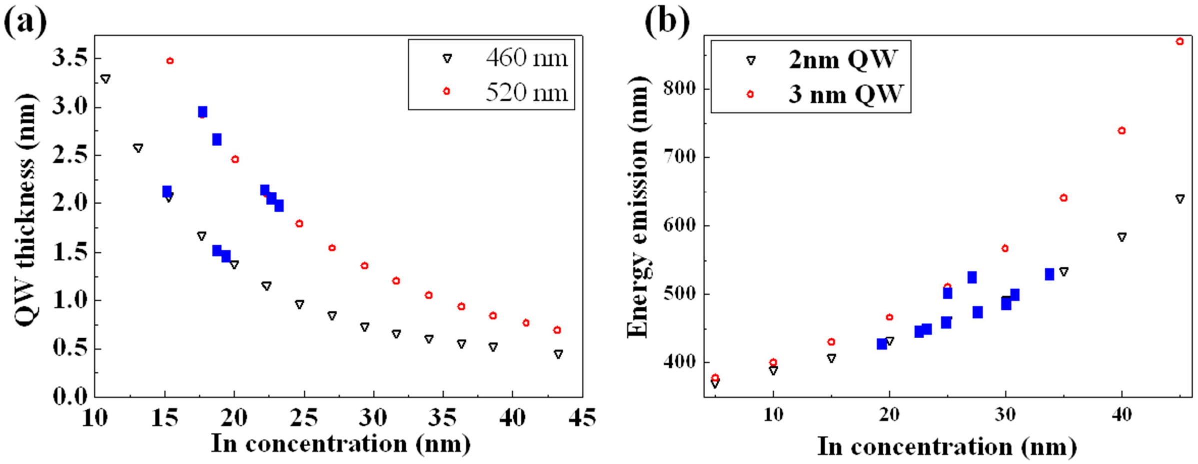

Figure 4. 21. Comparison of our extracted In composition from literature(our data: blue triangles) : (a) QW thickness vs In concentration[49], (b) Energy emission vs In concentration[50].

From reference 49, we have the plot of QW thickness versus In concentration for a blue and a green LED respectively. In this case, we know the emission of our QWs from PL and we know the exact thickness from TEM measurements, so we have over lied our results on top of these values, which are seen in solid triangles. In this work, almost all samples are emitting either in blue or in green except 1425, which is emitting in violet. In extracting indium composition, we have assumed the blue emitting InGaN layers corresponding to 460 nm and the green to 520 nm. From reference 50, we have the plot of emission wavelength versus In concentration corresponding to 2 nm and 3 nm InGaN QWs which is shown with open symbols in the Figure 4. 21 (b). We have from our PL and TEM, the emission energies and the real QW thickness. Though, we have thickness of QWs from about 1 nm to 3 nm, as mentioned in Table 4.2, but we have approximated the thickness close to either 2 nm or 3 nm to extract the In concentration corresponding to PL emission. The solid squares in Figure 4. 21 (b), corresponds to this work. We notice, in some cases, small discrepancies of as obtained In compositions with that of our samples and of nominal In contents. This could be accounted primarily due to the approximations; we employed to extract In compositions from references 49 and 50. The extracted values are listed in Table 4.2.

Table 4. 2 Summary of the InGaN/GaN QWs observed data on the investigated samples: Well thickness, In composition % and emission colour.

Specimen name	**Growth Technique**	**No. of QWs**	**InGaN QW thickness (nm)**		**PL peak position (nm)**	**In composition (%)**			
			nominal	**TEM**		**nominal**	**TEM**	**From Ref[49]**	**From Ref[50]**
L210	MBE	1	2.5	1.98	502	25	29	23.2	31
L212		1	2	1.5	447	25	19	18.74	22.6
A1809	MOVPE	1	1.5	1.4	453	25	27	19.79	23.2
A1807		2	3	2.9 and 2.6	508 and 525	25	32	17.83 and 19.2	24.54 and 26
L248H	MBE & MOVPE	1	2	1 and 2.08	473 and 532	25	26 & 3 0	24.2	26.9
		1	3				19 & 12.5	22.4	34.7
1386	MOVPE	5	2	1.95	495	25	18 - 21	23.3	30.81
1389		5	2	2.3	460	21	-	14.1	25
1425		30	2	1.99	426	20.8	-	*	19.2

4.5 Conclusions

We have systematically investigated the properties InGaN/GaN QWs by means of TEM, STEM and photoluminescence measurements. The investigated InGaN QWs layers are of thickness in the range of 1-3 nm with single pair of QW to 30 pairs of QWs, grown either by MBE and / or MOVPE techniques. As for the role of V-pits, they have been noticed to decorate the threading dislocations in the case of MOVPE growth, but we did not see any influence of these V pits on QWs. The QWs did not exhibit narrow sidewall quantum wells, therefore, the emission process in our samples does not follow the mechanism of dislocation screening by the potential wells as reported by Hangleiter et al. It is to be noted that, the V pit were not observed in MBE QWs, however, in quantum wells of similar thickness and nominal In content, we observed that the PL intensity for MOVPE QW is higher than that of MBE QW. To understand further, we carried out micro structural studies on these MBE and MOVPE QWs. We noticed that the MBE QWs have width fluctuations from one end to the other in contrast to MOVPE QWs, which have a well width homogeneity. This interfacial abruptness of the MOVPE QWs became enhanced by doping of Si in the GaN barriers which is consistent with the earlier reports by Keller et al[51]. Probably, the presence of high emission in MOVPE can be accounted for the homogeneous morphology of InGaN QW. We therefore have a consistent story that in InGaN/ GaN QW system, the well homogeneity gives higher PL luminescence which is illustrated in PL diagram in 4.4. We further conducted Quantitative HRTEM measurements to determine the local indium compositions from strain measurements. We found that the local In compositions could be higher than the nominal indium content and noticed local changes, this is probably an indication that there are local indium fluctuations in our InGaN/GaN QWs layers. As pointed out also, this is consistent with the temperature behavior in PL measurements. Using the chemical sensitive HAADF technique, it was possible to have accurate measurements of the QWs thicknesses within one monolayer accuracy and using this along with the peak position in our PL spectra, we were able to extract the average or effective indium composition using data from the literature. This procedure allowed us to obtain a consistent set of results between the various techniques used in this work without doing the complete calculation taking into account the strain and spontaneous polarization effects. We have also attempted to extract the local indium composition from the HAADF image contrast, in this instance, the obtained values are systematically smaller that that above. These are preliminary results and the discrepancy is still under investigation but could probably be due to a lack of known reference and/or bad correction of thin film relaxation effects.

4.6 References

---

[1] The Blue Laser Diode, edited by S. Nakamura and G. Fasol, Springer, Berlin (1997).

[2] J. Wu, W. Walukiewicz, K. M. Yu, J. W. Ager III, E. E. Haller, Hai Lu and W. J. Schaff, “Unusual properties of the fundamental band gap of InN”, Appl. Phys. Lett. **80**, 3967 (2002).

[3] I. Akasaki and H. Amano, “Crystal Growth and Conductivity Control of Group III Nitride Semiconductors and Their Application to Short Wavelength Light Emitters”, Jap. J. Appl. Phys. **36,** 5393 (1997).

[4] O.Jani, I. Ferguson, C. Honsberg and S. Kurtz, “Design and characterization of GaN/InGaN solar cells,” Appl. Phys. Lett. **91**, 132117 (2007).

[5] S.Nakamura,M. Senoh, N. Iwasa and S.-I. Nagahama, “High-power InGaN single-quantum-well-structure blue and violet light-emitting diodes”, Appl. Phys. Lett. **67**, 1868 (1995).

---

[6] T. Mukai, M. Yamada and S. Nakamura, "Characteristics of InGaN-Based UV/Blue/Green/Amber/Red Light-Emitting Diodes", Jpn. J. Appl. Phys., Part 1 **38**, 3976 (1999).

[7] C. Wetzel, T. Salagaj, T. Detchprohm, P. Li and J. S. Nelson, "GaInN⁄GaN growth optimization for high-power green light-emitting diodes", Appl. Phys. Lett. **85**, 866 (2004).

[8] V. Fiorentini, F. Bernardini and O. Ambacher, "Evidence for nonlinear macroscopic polarization in III–V nitride alloy heterostructures", Appl. Phys. Lett. **80**, 1204 (2002).

[9] A. Hangleiter, F. Hitzel, S. Lahmann and U. Rossow, "Composition dependence of polarization fields in GaInN/GaN quantum wells", Appl. Phys. Lett. **83**, 1169 (2003).

[10] F. A. Ponce, D. P. Bour, W. Götz, N. M. Johnson H. I. He lava, I. Grzegory, J. Jun, and S. Porowski, "Homoepitaxy of GaN on polished bulk single crystals by metalorganic chemical vapor deposition", Appl. Phys. Lett. **68**, 917 (1996).

[11] V. Potin, P. Ruterana, G. Nouet, R.C. Pond and H. Morkoç, "Mosaic growth of GaN on .0001. sapphire: A high-resolution electron microscopy and crystallographic study of threading dislocations from low-angle to high-angle grain boundaries", Phys. Rev. B **61**, 5587 (2000).

[12] S. Nakamura, M. Senoh, N. Iwasa and S. –I. Nagahama, "High power InGaN single quantum well structure blue and violet light emitting Diodes", Appl. Phys. Lett. **67**, 1868 (1995).

[13] S. Nakamura, M. Senoh, N. Iwasa, S. –I. Nagahama, T. Yamada and T. Mukai, "Superbright Green InGaN Single-Quantum-Well-Structure Light-Emitting Diodes", Jpn. J. Appl. Phys. **34**, L1332 (1995).

[14] J.K. Son, S.N. Lee, T. Sakong, H.S. Paek, O. Nam, Y. Park, J.S. Hwang, J.Y. Kim, Y.H. Cho, "Enhanced optical properties of InGaN MQWs with InGaN underlying layers", Journal of Crystal Growth **287**, 558 (2006).

[15] H. Zhao, G. Liu, and N. Tansu, "Analysis of InGaN-delta-InN quantum wells for light-emitting diodes", Appl. Phys. Lett. **97**, 131114 (2010).

[16] H. Zhao, G. Liu, X. –H. Li, G. S. Huang, D. Jonathan . S. Poplawsky, . T. Penn, V. Dierolf and N. Tansu, "Growths of staggered InGaN quantum wells light-emitting diodes emitting at 520–525 nm employing graded growth-temperature profile", Appl. Phys. Lett. **95**, 061104 (2009).

[17] Y. Narukawa, Y. Kawakami, M. Funato, S. Fujita, S. Fujita and S. Nakamura, "Role of self-formed InGaN quantum dots for exciton localization in the purple laser diode emitting at 420 nm", Appl. Phys. Lett. **70**, 981(1997)

[18] P. Ruterana, S. Kret, A. Vivet, G. Maciejewski and P. Dluzewski, "Composition fluctuation in InGaN quantum wells made from molecular beam or metalorganic vapor phase epitaxial layers", J. Appl. Phys. **91**, 8979 (2002).

[19] A. Vivet,S. Kret and P. Ruterana , "Investigation of the InGaN Quantum Wells Compositional Inhomogeneity" , Phys. Stat. Sol (c) **0**, 307 (2002).

---

[20] C. Kisielowski, Z. Liliental-Weber and S. Nakamura, “Atomic Scale Indium Distribution in a $GaN/In_{0.43}Ga_{0.57}N/Al_{0.1}Ga_{0.9}N$ Quantum Well Structure”, Jpn. J. Appl. Phys. **36**, 6932 (1997).

[21] S. Kret, G. Maciejewski, P. Dlujewski, P. Ruterana, N. Grandjean and B. Damilano, “Contribution to quantitative measurement of the In composition in GaN/InGaN multilayers”, Mat. Chem. and Phys. **81**, 273 (2003).

[22] C. Kisielowski, T.P. Bartel, P. Specht, F.-R. Chen and T.V. Shubina, “From extended defects and interfaces to point defects in three dimensions—The case of $In_xGa_{1-x}N$”, Physica B **401** 639 (2007).

[23] T.M. Smeeton, M.J. Kappers, J.S. Barnard, M.E. Vickers and C.J. Humphreys, “Electron-beam-induced strain within InGaN quantum wells: False indium “cluster” detection in the transmission electron microscope”, Appl. Phys. Lett. **83**, 5419 (2003).

[24] A. Rosenauer, D. Gerthsen, and V. Potin, “Strain state analysis of InGaN/GaN – sources of error and optimized imaging conditions”, Phys. Stat. Sol (a) **203**, 176 (2006).

[25] J. P. O’Neill, I. M. Ross, A. G. Cullis, T. Wang and P. J.Parbrook, “Electron-beam-induced segregation in InGaN/GaN multiple-quantum wells”, Appl. Phys. Lett. **83**, 1965 (2003).

[26] T. Li, E. Hahn, D. Gerthsen, A. Rosenauer, A. Strittmatter, L. Reissmann and D. Bimberg, “Indium redistribution in an InGaN quantum well induced by electron-beam irradiation in a transmission electron microscope”, Appl. Phys. Lett. **86**, 241911 (2005).

[27] R. Singh, D. Doppalapudi, T. D. Moustakas and L. T. Romano, “Phase separation in InGaN thick films and formation of InGaN/GaN double heterostructures in the entire alloy composition”, Appl. Phys. Lett. **70**, 1089 (1997).

[28] T. P. Bartel, P. Specht, J. C. Ho and C. Kisielowski, “Phase separation in $In_xGa_{1-x}N$”, Philosophical magazine, **87**, 1983 (2007).

[29] I. Ho and G. B. Stringfellow, “Solid phase immiscibility in GaInN”, Appl. Phys. Lett. **69**, 2701 (1996).

[30] T. Matsuoka, “Calculation of unstable mixing region in wurtzite $In_{1-x-y}Ga_xAl_yN$”. Appl. Phys. Lett. **71**, 105 (1997).

[31] S. F. Chichibu, A. Uedono, T. Onuma, B. Haskell, A. Chakraborty, T. Koyama, P. T. Fini, S. Keller, S. P. Denbaars, J.S. Speck, U. K. Mishra, S. Nakamura, S. Yamaguchi, S. Kamiyama, H. Amano, I. Akasaki, J.Han, and T. Sota, “Origin of localized excitons in In-containing three-dimensional bulk (Al,In,Ga)N alloy films probed by time-resolved photoluminescence and monoenergetic positron annihilation techniques”, Phil. Magazine **87**, No. 13, 2019 (2007).

[32] C. J. Humphyers, “Does In form In-rich clusters in InGaN quantum wells?”, Phil. Magazine **87**, 1971 (2007).

[33] T.P. Bartel and C. Kisielowski, “A quantitative procedure to probe for compositional inhomogeneities in $In_xGa_{1-x}N$ alloys”, Ultramicroscopy **108**, 1420 (2008).

---

[34] A. Hangleiter, C. Netzel, D. Fuhrmann, F. Hitzel, L. Hoffmann, H. Bremers, U. Rossow, G. Ade and Hinze, “Anti-localization suppresses non-radiative recombination in GaInN/GaN quantum well”, Phil. Magazine **87**, 2041 (2007).

[35] X.H. Wu, C.R. Elsass, A. Abare, M. Mack, S. Keller, P.M. Petroff, S.P. DenBaars, J.S. Speck, S.J. Rosner, “Structural origin of V-defects and correlation with localized excitonic centers in InGaN/GaN multiple quantum wells”, Appl. Phys. Lett. **72**, 692 (1998).

[36] Y. Chen, T. Takeuchi, H. Amano, I. Akasaki, N. Yamada, Y. Kaneko, S.Y. Wang, “Pit formation in GaInN quantum wells”, Appl. Phys. Lett. **72**, 710 (1998).

[37] N. Sharma, P. Thomas, D. Tricker, C. Humphreys, “Chemical mapping and formation of V-defects in InGaN multiple quantum wells”, Appl. Phys. Lett. **77**,1274 (2000).

[38] H.K. Cho, J.Y. Lee, C.S. Kim, G.M. Yang, N. Sharma, C. Humphreys, “Microstructural characterization of InGaN/GaN multiple quantum wells with high indium composition”, J. Cryst. Growth **231**, 466 (2001).

[39] M. Shiojiri, C. C. Chuo, J. T. Hsu, J. R. Yang and H. Saijo, “Structure and formation mechanism of V defects in multiple InGaN/GaN quantum well layers”, J. Appl. Phys. **99**, 073505 (2006).

[40] A.M. Sánchez, M. Gass, A.J. Papworth, P.J. Goodhew, P. Singh, P. Ruterana, H.K. Cho, R.J. Choi and H.J. Lee, “V-defects and dislocations in InGaN/GaN heterostructures”, Thin Solid Films **479**, 316 (2005).

[41] L. Nistor and H. Bender, “Direct evidence of spontaneous quantum dot formation in a thick InGaN epilayer”, Appl. Phys. Lett. **77**, 507 (2000).

[42] N. Grandjean, E. Feltin, R. Butte and J.-F. Carlin, “Growth mode induced carrier localization in InGaN/GaN quantum wells”, Phil. Magazine **87**, 2067 (2007).

[43] P. Chen, S. J. Chua and Z. L. Miao, “Photoluminescence of InGaN/ GaN multiple quantum wells originating from complete phase separation”, J. Appl. Phys. **93**, 2507 (2003).

[44] S. W. Feng, Y. –C. Cheng, Y. –Y. Chung, C. C. Yang, Y. –S. Lin and C. Hsu, K. –J. Ma, J. -I. Chyi, “Impact of localized states on the recombination dynamics in InGaN/GaN quantum well structures”, J. Appl. Phys. **92**, 4441(2002).

[45] Y-H. Cho, G. H. Gainer, A. J. Fischer, J. J. Song, S. Keller, U. K. Mishra, and S. P. DenBaars “S-shaped” temperature-dependent emission shift and carrier dynamics in InGaN/GaN multiple quantum wells”, Appl. Phys. Lett. **73**, 1370 (1998).

[46] S. Chichibu, T. Azuhata, T. Sota and S. Nakamura, “Luminescences from localized states in InGaN epilayers”, Appl. Phys. Lett. **70**, 2822 (1997).

[47] S. Kret, P. Ruterana, A. Rosenauer and D. Gerthsen, “Extracting Quantitative Information from High Resolution Electron Microscopy”, Phys. Stat. Sol(b) **227**, 247 (2001).

[48] I. Aasaki and H. Amano, “Crystal growth and conductivity control of group III Nitride semiconductors and their application to short wavelength light emitters”, Jpn. J. Appl. Phys. **36**, 5393 (1997).

---

[49] D. Fuhrmann, C. Netzel, U. Rossow, A. Hangleiter, G. Ade and P. Hinze, “Optimization scheme for the quantum efficiency of GaInN-based green-light-emitting diodes”, Appl. Phys. Lett. **88**, 071105 (2006).

[50] H. Zhao, G. Liu and N. Tansu, “Analysis of InGaN-delta-InN quantum wells for light-emitting diodes”, Appl. Phys.Lett. **97**, 131114 (2010).

[51] S. Keller, S. Chichibu, M. Minsky, E. Hu, U.K. Mishra and S. DenBaars, “Effect of the Growth rate and the barrier doping on the morphology and the properties of InGaN/GaN quantum wells”, J. Crystal Growth **195**, 258 (1998).

Chapter 5

Conclusions and Perspectives

This work had two main objectives which are critical for improving the performances of group III nitride semiconductor devices:

(a) Investigation of the transport properties of InN by extensive electrical characterization of this member of the nitride semiconductor, whose band gap was recently re-evaluated. This brought about new potential important applications, from efficient photovoltaics to devices capable to be operated in terahertz wavelengths.

(b) Determination of the structural and optical properties of InGaN/GaN QWs, which are the active parts of multicolour LEDs for solid state lighting applications.

5.1 InN layers

5.1.1 Conclusions

It is well known that the presence of surface electron accumulation in InN layers is still an important limitation to device applications. However recent reports[1], stated the accessibility of this bulk electrical conductivity, but there exists a discrepancy between the estimated doping levels and real ones. In our work, we have explored this issue using low frequency noise measurements on PAMBE InN layers. We obtained the following results:

- It was shown that the best optimum conditions for fabrication technology would be when the electrical isolation is done prior to metallization step and then followed by thermal annealing, with annealing times less than 20 min.

- We observed, in all of the InN layers, the contact resistances are extremely small 10^2-10^3 times smaller than the sheet resistances.

- The estimated mobilities of InN layers are closely related to the surface roughness. These layers follow the same trend as in Silicon MOS devices, where the electrical conduction takes place at the surface, pointing to the electrical conduction at the surface in these InN layers.

- The as obtained normalized noise levels are close to other conventional group III devices such as GaAs, InAs which are presently used in high frequency devices. These results indicate that the present studied InN layers are promising to use in electronic devices.

- In our electrical resistivity versus temperature study, we determined a transition from semiconducting behaviour to metal like conduction above 130 K, irrespective of In or N rich growth conditions. Moreover, the 1/f noise trend versus temperature indicates that the surface conduction is dominant above 100 K temperatures.

- At temperatures less than or equal to 100 K, a Lorentzian noise is present apart from 1/ f noise and white noise, this allowed us to determine the activation energy of a trap level about ~ 50 meV below the conduction band. These results show that, below 100 K, there is an additional contribution of electrical conduction apart from the surface conduction, in other words, we accessed bulk conductivity in our samples, which cannot be achieved with conventional C-V techniques in InN.

5.1.2 Open questions and future work

- Though, we have been successful in accessing the bulk electrical conductivity, it is still necessary to separate quantitatively this surface and bulk electrical conduction.

- Using simple models, we demonstrated that mobility fluctuations are coming out from bulk, this is still need to be checked experimentally with Hall measurements.

- It will be of interest to investigate, if the low frequency noise can be used to probe electrical conduction in p type doped InN layers, which is hard to access with conventional techniques.

5.2 InGaN/GaN QWs

5.2.1 Conclusions

For the emission in InGaN layers, we have systematically studied the structural properties and their correlation with photoluminescence of InGaN/GaN QWs. We have investigated the InGaN QWs with different characteristics such as well widths, number of QWs, nominal In composition, and the undoped and Si doped GaN barriers. The investigated QWs, consist of well thickness of 1 nm to 3 nm, with nominal indium compositions of 20 to 25%, emission wavelengths were from violet, blue and green.

- It was pointed out that the GaN barriers doped with Silicon, result in abrupt interfaces, with 1 monolayer.

- V pits have formed in MOVPE QWs, irrespective of the well thickness, however, they have no impact on the QWs.

- PL studies confirmed higher emission in MOVPE QWs in comparison to MBE QWs. This could be due to the homogeneous well morphology in MOVPE QWs, whereas MBE QWs exhibited well width fluctuations.

- We also have performed quantitative high resolution TEM, for strain mapping and observed local indium fluctuations.

- Further, studies with HAADF-STEM, results in accurately determining the InGaN well thickness. Using these thicknesses and the PL peak positions, we have obtained the indium compositions, taking into account the effect of QCSE and quantum confinement effects from the literature, and this is in the range of the In content obtained from strain measurements if we assume that we have local In composition fluctuations.

5.2.2 Open questions and future work

- As reported by Hangleiter *et al*[2], the V shaped defects are accounted for the high emission, so in order to confirm this study in our layers; it would be interesting to study the internal quantum efficiencies of MOVPE layers.

- Our STEM quantitative measurements resulted in underestimating the In compositions, this requires further studies to assess this technique which normally should be the most accurate.

5.3 References

---

[1] X. Wang, S.-B. Che, Y. Ishitani and A. Yoshikawa, “Systematic study on p-type doping control of InN with different Mg concentrations in both In and N polarities” Appl. Phys. Lett. **91**, 242111 (2007).

[2] A. Hangleiter, C. Netzel, D. Fuhrmann, F. Hitzel, L. Hoffmann, H. Bremers, U. Rossow, G. Ade and Hinze, “Anti-localization suppresses non-radiative recombination in GaInN/GaN quantum wells”, Philosophical Magazine, **87**, 2041 (2007).

Annex I

This annex provides a short description of the predicted evolution of 1/f noise level in InN layers according to mobility fluctuations. First the techniques used to estimate the mobility is described and then the model of noise is given.

1 Estimation of mobility

From resistance measurements performed at different temperatures, one can estimate the evolution of the mobility assuming that

$$R_M(T) = \frac{L}{\sigma(T)A} \tag{I.1}$$

where R_M is the resistance, T is the temperature, L is the length, A is the cross section of the device and σ is the conductivity.

Assuming that only electrons participate in the conduction, one can write:

$$\sigma(T) = n(T).\mu(T).q \tag{I.2}$$

where $\mu(T)$ is the mobility of carriers at temperature T , $n(T)$ is the carrier concentration at T and q is the charge of the electron.

Using equations (I.1) and (I.2), the ratio of resistances at 300 K and T K, is given:

$$\frac{R_M(300)}{R_M(T)} = \frac{n(T).\mu(T)}{n(300).\mu(300\,)} \tag{I.3}$$

In the following calculation, the numerical values have been taken for carrier concentration and mobity as , $n(T) = 10^{18}$ At/cm^3 (This value was taken from reference 1, in which the carrier concentration were extracted on these InN layers by using Raman measurements). And the mobility, $\mu(T) = 625$ cm^2/V.s, was extracted using equation equation (I.2).

Two hypotheses have been considered:

(1) InN is considered as an intrinsic semiconductor, in this case, the carrier concentration is given by $n(T) = Constant.T^{\frac{3}{2}}.\exp(-\frac{Eg}{k_BT})$ where E_g is the bandgap, k_B is the Boltzmann constant.

(2) InN is considered as a doped semiconductor and the carrier concentration is independent of the temperature in the range of the investigated temperatures (all doping atoms are ionized) *i.e* $n(T) = n(300)$.

Finally $\mu(T)$ can be rewritten as below by using equation (I.3),

$$\mu(T) = \frac{R_M(300)}{R_M(T)} . \frac{n(300).\mu(300)}{n(T)} \tag{I.4}$$

2 Noise Model

The same kind of work has been done for the noise model in the case of mobility fluctuations. This section consists in very preliminary studies and should be largely discussed and improved.

As conductivity is given by, $\sigma = n.\mu.q$, fluctuations in current can be due to fluctuations in either mobility (Δμ model) or number (ΔN model) fluctuations. For more details refer to section 1.5.6 of chapter 1.

From our experiments we have, $$S_v = \frac{K_v}{f} . v^2 \tag{I.5}$$

Δμ model gives, $$\frac{S_v}{v^2} = \frac{S_\mu}{\mu^2} \tag{I.6}$$

ΔN model gives, $$\frac{S_v}{v^2} = \frac{S_N}{N^2} \tag{I.7}$$

2.1 Δμ model

A basic description of this model can be found in reference 2. We have

$$\frac{S_\mu}{\mu^2} = \frac{\alpha}{fN} \tag{I.8}$$

where is the N is the total number of free carriers in the sample and α is related to mobility of the charge carriers.

According to Matthieussen law, one can write that the mobility in a semiconductor is due to lattice scattering (mobility μ_{latt}) and dopant scattering (mobility μ_{dop}), so that the effective mobility μ is given by

$$\mu = \left[\frac{1}{\mu_{latt}} + \frac{1}{\mu_{dop}}\right]^{-1} \tag{I.9}$$

In this present theory, it is assumed that only lattice scattering causes 1/f noise (see reference 3), so that by assuming $\mu_{dop} = 0$ and from equation (I.8), one can derive

$$\alpha = \alpha_{latt} \frac{\mu^2}{\mu_{latt}{}^2} \qquad \text{(I.10)}$$

Using these relationships, it follows that

$$\frac{S_v}{v^2} \infty \frac{\mu^2}{n} \qquad \text{(I.11)}$$

In modeling with temperature evolution, it is further assumed that μ_{latt} and α_{latt} do not depend on the temperature. Then by using equations (I.5) and (I.11), we obtain

$$\frac{K_v(T)}{K_v(300)} = \frac{\mu^2(T)}{n(T)} \cdot \frac{n(300)}{\mu^2(300)} \qquad \text{(I.12)}$$

2.2 ΔN model

Number fluctuations model[4] predicts that,

$$\frac{S_N}{N^2} \infty \mathrm{T} \qquad \text{(I. 13)}$$

Using equations (I.5) and (I. 13), ΔN model can be rewritten as

$$\frac{K_v(T)}{K_v(300)} = \frac{T}{300} \qquad \text{(I.14)}$$

The equations (I.12) and (I.14) were plotted with experimental results in Figure 3.22 of chapter 3.

References

[1] A. Vilalta-Clemente, A Ph.D thesis on “Structure of InN and InAlN alloys”, University of Caen, (2012).

[2] F. N. Hooge, “1/f noise sources”, IEEE trans. on Elect. Dev. **4**1, 1926(1994).

[3] F. N. Hooge, “Lattice scattering causes 1/f noise”, Phys. Lett. A **66**, 315 (1978).

[4] F. N. Hooge, “Experimental studies on 1/f noise”, Rep. Prog. **44**, 479 (1981).

Annex II

This annex gives a brief description of In compositions quantitative measurements in HRSTEM images. For instance, we will describe here in case of one sample, how we have extracted the In composition. This section of work is mainly contributed by Bertrand Lacroix, Post doctorate in CIMAP, Caen. More results have been discussed in chapter 4.

Method for evaluating composition from intensity profiles

Figure 1, shows a low magnification STEM HAADF image of the sample (L248H) viewed in cross section along [11-20]. This shows a HAADF scan in which two InGaN/GaN layers QWs and part of thick GaN are visible. The InGaN/GaN interfaces as shown in Figure 1 (a) are relatively abrupt.

The first step of the analysis consists in extracting the intensity profile (shown in Figure 1 (b) from the raw image (I_{raw}).

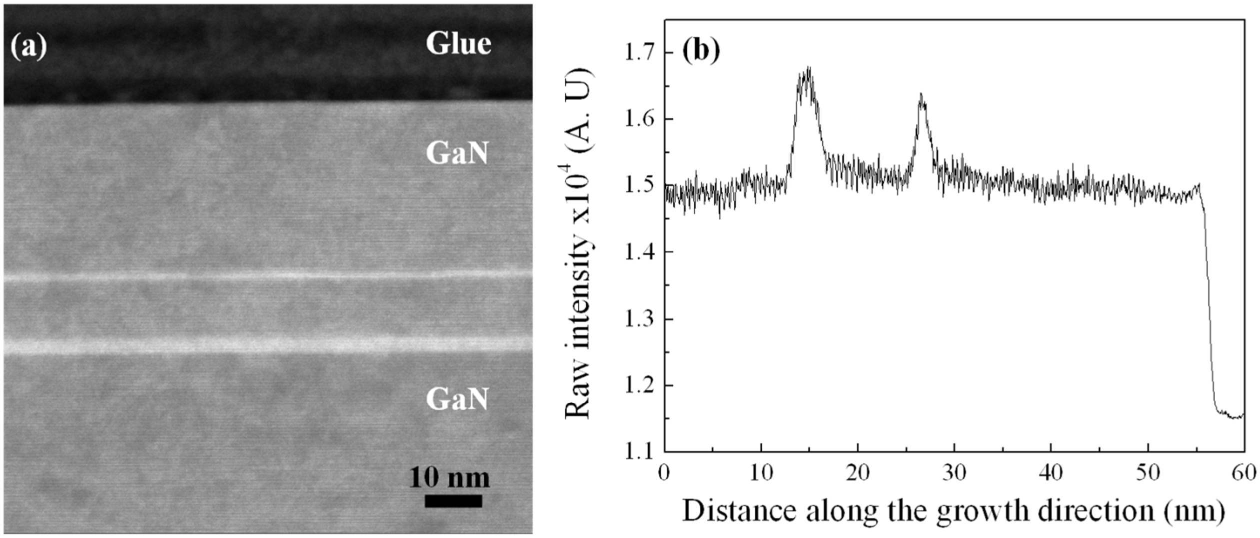

Figure 1. STEM HAADF image of (a) Two InGaN/GaN layers and part of thick GaN buffer layer at the bottom in Sample L248H, (b) Extraction of the intensity profile from the corresponding STEM HAADF image.(White contrast regions correspond to InGaN QW regions: thinner one corresponds to MBE and thicker one corresponds to MOVPE)

Intensity normalization is required to obtain quantitative informations (sample thickness, composition) from the HAADF signal. It is given by $I_{norm} = (I_{raw}-I_{vac})/ (I_{det}- I_{vac})$, where I_{det} and I_{vac}

represent the average intensities of the incident electron probe in the detector region (I_{det}) and in the vacuum region (I_{vac}). These values are determined from a detector scan (shown in Figure 2).

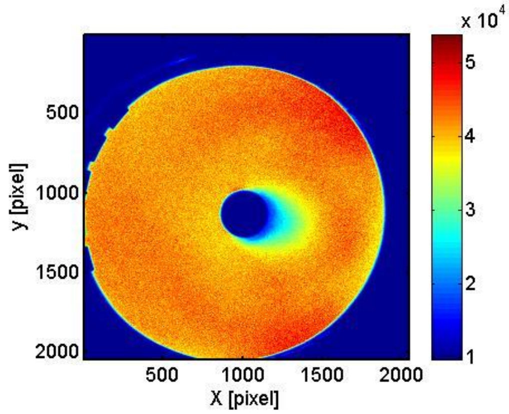

Figure 2 Registered intensity of the incident electron probe as a function of the position on the detector.

Evaluation of the sample thickness is performed by fitting a polynomial to the GaN regions used as references in the profile (Figure 3a) and by comparing the experimental intensities to simulations. The estimated thickness for this sample is approximately 50 nm (Figure 3b).

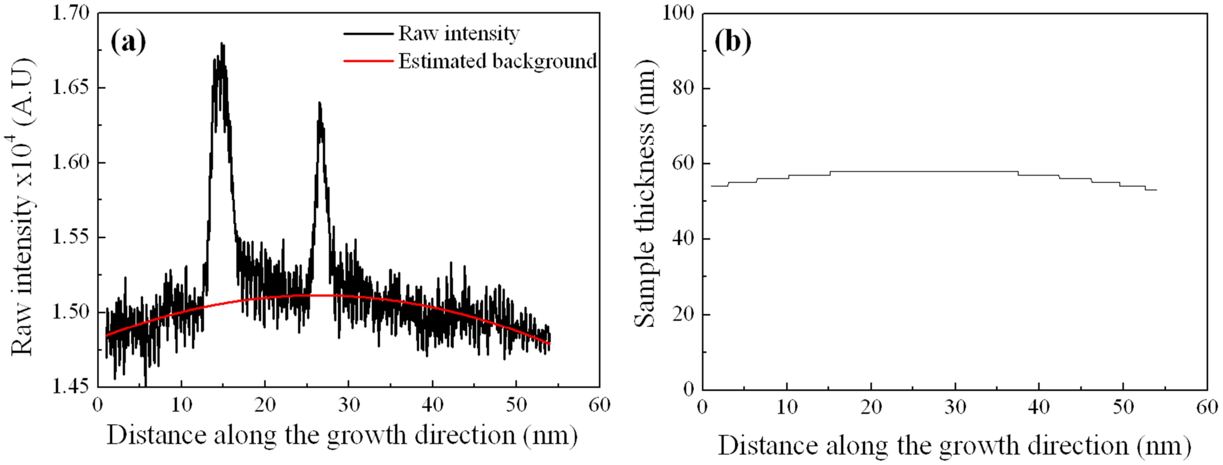

Figure 3. Evaluation of background intensity by fitting the reference region in the profile and the corresponding thickness profile

Then, the intensity ratio profile between the reference regions (GaN) and the QW regions (InGaN) is determined, and the indium concentration profile is evaluated (Figure 4) from the comparison of the intensity variations to simulations.

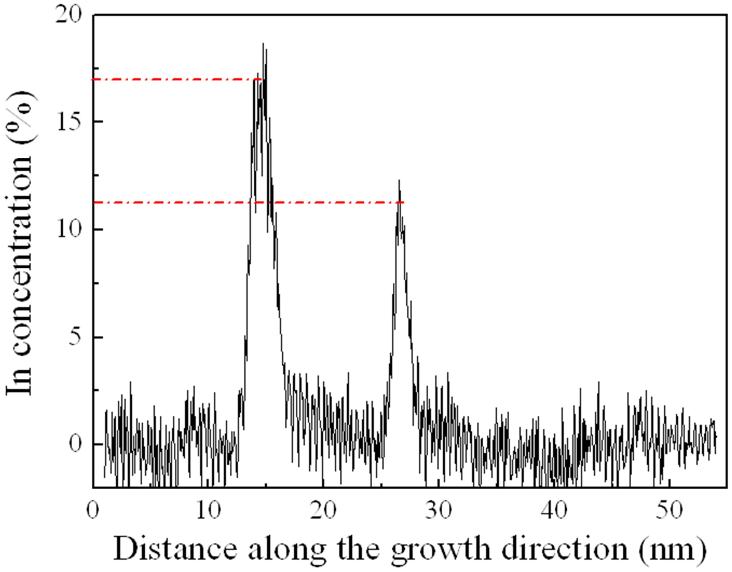

Figure 4. Indium concentration profile, red dotted lines gives the level of indium content.

Method for evaluating composition in high resolution STEM-HAADF images

The experimental procedure for composition mapping from HRSTEM images is similar to the previous one. It is fully explained in reference 1.The Figure 5 shows a high resolution HAADF STEM image of InGaN/GaN QWs. The intensity analysis is performed in each atomic column. A

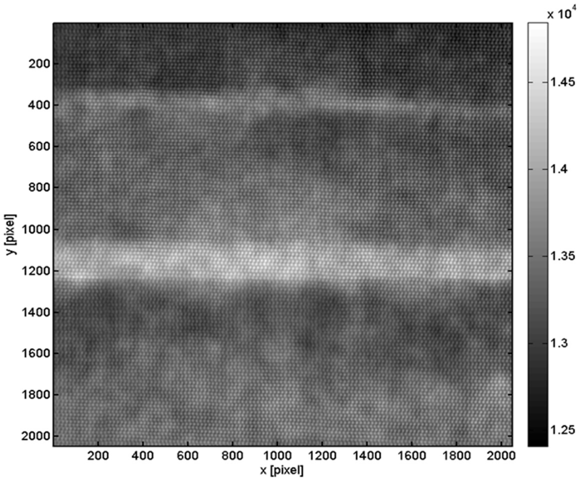

Figure 5. Filtered HRSTEM image

Wiener filter is applied on the raw image to facilitate the detection of the atomic columns (Figure 5). The positions of the pixels having the highest intensities are used to estimate the positions of the atomic column, and a local mean intensity is computed for each column. After having specified reference regions for background determination (GaN barriers), the intensity is normalized in each column with respect to the intensity of the incident electron beam determined from the detector scan. The corresponding indium concentration map is given by the Figure 6.

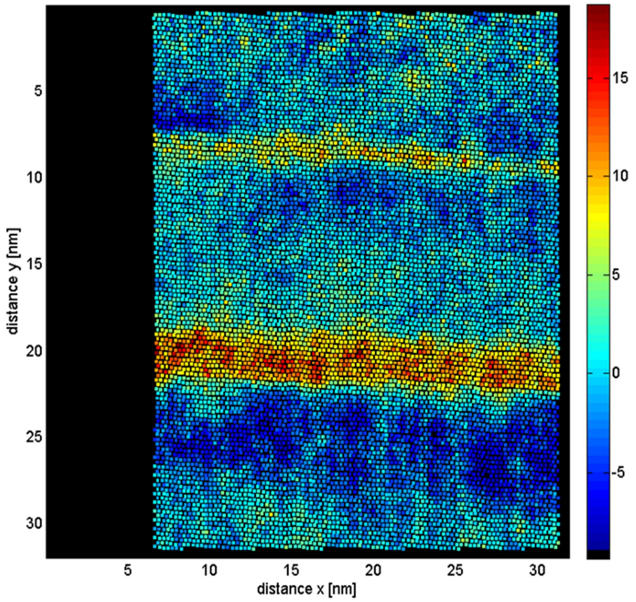

Figure 6. In concentration map.

The InGaN/GaN MOVPE QW interface is more abrupt than that of MBE QW. The thicknesses of the InGaN QWs and the GaN barriers are measured to be around 1.5 nm, 3 nm and 10 nm respectively. The contrast within the GaN barrier is relatively uniform, suggesting that no phase separation has taken place.The measured InGaN layer widths and barrier layer values agrees well with previous measurements with Conventional TEM. Form the two dimensional composition map, it is clearly seen that inside the QW, the indium composition fluctuates (Figure 6).

References

[1] A. Rosenauer, T. Mehrtens, K. Müller , K. Gries, M. Schowalter, P. VenkataSatyam, S. Bley, C. Tessarek, D. Hommel, K. Sebald, M. Seyfried, J. Gutowski, A. Avramescu, K. Engl and S. Lutgen, “Composition mapping in InGaN by scanning transmission electron microscopy”, Ultramicroscopy **111,** 1316 (2011).

Propriétés structurales, optiques et électroniques des couches d'InN et hétérostructures riches en indium pour applications optoélectroniques

Résumé :

Les semi-conducteurs nitrures (AlN, GaN, InN) focalisent une activité de recherche intense en raison de nombreuses applications comme les diodes électroluminescentes, les composants de puissance ou hyperfréquence. Dans cette recherche, nous avons abordé le travail sous deux angles: a) la conduction électrique dans les couches d'InN produites par croissance épitaxiale aux jets moléculaires assistée par plasma (PAMBE) et une recherche sur l'origine de la forte émission bleue dans les puits de quantiques d'InGaN/GaN.

L'accumulation d'électron en surface dans les couches d'InN constitue une limitation importante pour la fabrication de composants. Au cours de ce travail, nous avons exploré l'utilisation des mesures de bruit de basse fréquence sur les couches d'InN et pu accéder à leur conductivité électrique en volume.

L'étude des puits quantiques d'InGaN/GaN, obtenue par croissance épitaxiale aux jets moléculaires (MBE) ou épitaxie en phase vapeurs aux organométalliques (MOVPE) , a été effectuée par analyses de la microstructure par microscopie électronique en transmission (MET, HRTEM et STEM) en corrélation avec les propriétés optiques d'un grand nombre d'échantillons provenant de conditions de croissance différentes. Ce travail nous a permis d'acquérir une vision plus critique du rôle des conditions de fabrication et des paramètres comme la morphologie, les fluctuations de composition et la présence des défauts en V sur les explications actuellement avancées pour la forte efficacité d'émission dans les puits quantiques d' InGaN/GaN.

Mots-clés : InN, InGaN, PAMBE, MOVPE, MET, STEM, HRSTEM, bruit basse fréquence, conduction électrique en volume, puits quantique, fluctuations de composition

Structural, optical and electronic properties of InN films and In rich heterostructures for optoelectronic applications

Abstract :

The nitride semiconductors (AlN, GaN, InN) are subject to a large research effort-due to their numerous applications, such as light emitting diodes, high power and high frequency components. The aim of this work has been twofold: to investigate the electrical conduction in InN layers and the origin of the high emission efficiency in InGaN/GaN Quantum Wells (QWs).

The surface electron accumulation in InN layers is still an important limitation to device applications. We have explored this point using low frequency noise measurements on Plasma Assisted Molecular Beam Epitaxy (PAMBE) InN layers and we demonstrated that the bulk electrical conductivity of InN can be accessed.

The investigation of quantum wells produced by Molecular Beam Epitaxy (MBE) or Metalorganic Vapour Phase Epitaxy (MOVPE), has been carried out through microstructural analyses by Transmission Electron Microscopy techniques(TEM, HRTEM, STEM) in correlation with optical properties on a large number of samples grown in different growth conditions. This experimental work has allowed us to obtain a critical view on the role of the growth conditions and such parameters as the well morphology, composition fluctuations, as well as the V shaped defects on the current explanations of high emission efficiency in InGaN/GaN QWs.

Keywords: InN, InGaN, GaN, PAMBE, MBE, MOVPE, TEM, HRTEM, STEM, low frequency noise, bulk electrical conduction, quantum wells, In compositional fluctuations